

ABSTRACT OF DISSERTATION

Emmanuel Momjian

The Graduate School

University of Kentucky

2003

SENSITIVE VERY LONG BASELINE INTERFEROMETRY STUDIES OF
INTERACTING/MERGING GALAXIES

ABSTRACT OF DISSERTATION

A dissertation submitted in partial fulfillment of the
requirements for the degree of Doctor of Philosophy
in the College of Arts and Sciences at the University of Kentucky

By

Emmanuel Momjian

Lexington, Kentucky

Director: Dr. Thomas H. Troland, Professor of Physics and Astronomy

Lexington, Kentucky

2003

Copyright © Emmanuel Momjian 2003

ABSTRACT OF DISSERTATION

SENSITIVE VERY LONG BASELINE INTERFEROMETRY STUDIES OF INTERACTING/MERGING GALAXIES

It has become clear in recent years that the study of interacting/merging galaxies plays an important role in understanding important astrophysical phenomena. This thesis presents an observational study of interacting/merging galaxies at radio frequencies. The observations have been carried out at extremely high resolution using very long baseline interferometry. The observations described here include: (1) A study of the high velocity H I absorption associated with the peculiar galaxy NGC 1275; (2) A study of the radio continuum and H I absorption of the ULIRG IRAS 17208–0014; (3) A study of the radio continuum and H I absorption of the LIRG NGC 7674.

Some of the most prominent results of these observations include:

- Detection of several narrow H I absorption features in the high velocity system associated with NGC 1275. These H I absorption lines were observed toward the strong radio nucleus 3C 84. The results indicate the existence of several H I clouds with velocity differences and widths similar to those seen in Galactic neutral hydrogen absorption and similar to some of the H I absorption seen in the Large Magellanic Cloud.

- The discovery of an extreme nuclear starburst region in the advanced merger system IRAS 17208–0014. Our results suggest a star formation rate of $84 M_{\odot} \text{ yr}^{-1}$, and a supernova rate of 4 yr^{-1} . H I absorption is detected in multiple components with optical depths ranging between 0.3 and 2.5, and velocity widths between 58 and 232 km s^{-1} .
- The detection of complex jet structures in the inner 1 kpc region of the galaxy NGC 7674. At full resolution, several compact sources are observed with brightness temperatures on the order of 10^7 K . While it is possible that one of these compact structures could host an AGN, they could also be shock-like features formed by the interaction of the jet with compact interstellar clouds in the nuclear region of this galaxy. At least eight H I absorption lines are detected toward some of the continuum emission regions in NGC 7674. If the widest H I feature in our observations is rotationally broadened by a central supermassive black hole, the implied dynamical mass is about $10^7 M_{\odot}$.

KEYWORDS: Galaxies: Interactions, Galaxies: Seyfert, Galaxies: Starburst, Observations: Radio Continuum and 21 cm Hydrogen Line, Techniques: Radio Interferometry

Emmanuel Momjian

August 28, 2003

SENSITIVE VERY LONG BASELINE INTERFEROMETRY STUDIES OF
INTERACTING/MERGING GALAXIES

By

Emmanuel Momjian

Thomas H. Troland
Director of Dissertation

Thomas H. Troland
Director of Graduate Studies

August 28, 2003

RULES FOR THE USE OF DISSERTATIONS

Unpublished theses submitted for the Doctor's degree and deposited in the University of Kentucky Library are as a rule open for inspection, but are to be used only with due regard to the rights of the authors. Bibliographical references may be noted, but quotations or summaries of parts may be published only with the permission of the author, and with the usual scholarly acknowledgements.

Extensive copying or publication of the thesis in whole or in part requires also the consent of the Dean of the Graduate School of the University of Kentucky.

DISSERTATION

Emmanuel Momjian

The Graduate School

University of Kentucky

2003

SENSITIVE VERY LONG BASELINE INTERFEROMETRY STUDIES OF
INTERACTING/MERGING GALAXIES

DISSERTATION

A dissertation submitted in partial fulfillment of the
requirements for the degree of Doctor of Philosophy
in the College of Arts and Sciences at The University of Kentucky

By

Emmanuel Momjian

Lexington, Kentucky

Director: Dr. Thomas H. Troland, Professor of Physics and Astronomy

Lexington, Kentucky

2003

Copyright © Emmanuel Momjian 2003

I dedicate this dissertation to the love of my life, my wife Mari.
Without her love and support throughout these years,
this work would not have been possible.

ACKNOWLEDGMENTS

During the years leading to the completion of a thesis, the help of countless people makes the difference. My thesis was not an exception, and I would like to acknowledge my debt of gratitude to at least some of them. First, and foremost I thank my wife, Mari, for her love, support, and encouragement through all the times. I will also be forever grateful to the person who introduced me to radio astronomy, my academic adviser Tom Troland. Without Tom's invaluable advise, help, support, and guidance, which started from the first days I joined the University of Kentucky, I would never have made it this far. I also extend foremost thanks to my NRAO adviser, Jon Romney, who taught me the details of doing VLBI and using AIPS. With extraordinary patience, he read, checked, and corrected all my VLBA schedules, proposals and papers. Jon has been very generous with his time and resources. His support and guidance have been critical to this thesis. Another NRAO scientist who made a significant impact on my outlook and scientific achievement, is Chris Carilli. Chris introduced me to the exiting universe of IR galaxies. His help and encouragement were essential in the success of this project. My heartfelt thanks also go to two colleagues, Crystal Brogan and Anuj Sarma, who both taught me many tricks in the business, and tirelessly helped me in various things related to the work presented in this thesis and beyond. I would also like to thank Kumar Golap for being always available to teach me AIPS++. My thanks also go to the pre-docs and the postdocs of NRAO for the very useful conversations and discussions we had. I have enjoyed the hospitality of the National Radio Astronomy Observatory during the three years I've spent in Socorro, and I am grateful to most of the staff members of the observatory. Their doors were always open to answer my questions. Support for this work was provided by the Predoctoral Research Program and the Graduate Summer Student Research Assistantship of the National Radio Astronomy Observatory, and the NSF grant AST 99-88341.

Table of Contents

Acknowledgements	iii
List of Tables	vi
List of Figures	vii
List of Files	ix
1 Introduction	1
1.1 INTERACTING/MERGING GALAXIES	1
1.2 VERY LONG BASELINE INTERFEROMETRY	3
1.2.1 The Very Long Baseline Array (VLBA)	4
1.3 OVERVIEW OF THESIS PROJECTS	6
1.3.1 Chapter 2	6
1.3.2 Chapter 3	7
1.3.3 Chapter 4	7
2 Global VLBI Observations of the High Velocity H I Absorption Toward NGC 1275¹	18
2.1 INTRODUCTION	18
2.2 OBSERVATIONS	19
2.3 RESULTS	21
2.3.1 The Continuum	21
2.3.2 The H I Absorption	22
2.4 DISCUSSION	24
2.5 CONCLUSIONS	25
3 Sensitive VLBI Continuum and H I Absorption Observations of the Ultra-Luminous Infrared Galaxy IRAS 17208–0014²	34
3.1 INTRODUCTION	34
3.2 OBSERVATIONS AND DATA REDUCTION	36

¹Results presented in Chapter 2 have been published in the February 2002 edition of The Astrophysical Journal (vol. 566; p 195-201) by E. Momjian, J. D. Romney, & T. H. Troland.

²Results presented in Chapter 3 have been published in the April 2003 edition of The Astrophysical Journal (vol 587; p. 160-170) by E. Momjian, J. D. Romney, C. L. Carilli, T. H. Troland, & G. B. Taylor.

3.3	RESULTS AND ANALYSIS	37
3.3.1	The Radio Continuum	37
3.3.2	The H I Absorption	39
3.4	DISCUSSION	41
3.4.1	The Radio Continuum	41
3.4.2	The H I Absorption	46
3.5	CONCLUSIONS	47
4	Sensitive VLBI Continuum and H I Absorption Observations of NGC 7674: First Scientific Observations with the Combined Array VLBA, VLA & Arecibo³	58
4.1	INTRODUCTION	58
4.2	OBSERVATIONS AND DATA REDUCTION	60
4.3	RESULTS AND ANALYSIS	62
4.3.1	The Radio Continuum	62
4.3.2	The H I Absorption	64
4.4	DISCUSSION	68
4.4.1	The Radio Continuum	68
4.4.2	The H I Absorption	71
4.4.3	The age of the AGN in NGC 7674	74
4.5	CONCLUSIONS	74
5	Summary and Future Work	94
5.1	SUMMARY	94
5.1.1	Global VLBI Observations of the high Velocity H I Absorption To- ward NGC 1275	94
5.1.2	Sensitive VLBI Continuum and H I Absorption Observations of the Ultra-Luminous IR Galaxy IRAS 17208–0014	95
5.1.3	Sensitive VLBI Continuum and H I Absorption Observations of the Seyfert-2 NGC 7674	95
5.2	FUTURE WORK	97
	References	99
	Vita	105

³Results presented in Chapter 4 have been accepted for publication in The Astrophysical Journal (E. Momjian, J. D. Romney, C. L. Carilli & T. H. Troland).

List of Tables

1.1	Locations of the VLBA Antennas	8
1.2	VLBA Baseline Lengths in km	9
2.1	Parameters of the Global VLBI Observations of NGC 1275	27
2.2	Parameters of the High Velocity H I Clouds in NGC 1275	28
3.1	Parameters of the VLBI Observations of IRAS 17208–0014	49
3.2	Compact Sources in IRAS 17208–0014	50
3.3	Parameters of the H I Clouds in IRAS 17208–0014	51
4.1	Parameters of the VLBI Observations of NGC 7674	76
4.2	Gaussian Fits to the Central Component in NGC 7674	77
4.3	Gaussian Fits to the Western Component in NGC 7674	78
4.4	Parameters of the Continuum Components in Figure 4.4	79
4.5	Physical Properties of the Continuum Structures	80
4.6	Gaussian Fit Parameters of the H I Absorption Features at High Resolution	81
4.7	Gaussian Fit Parameters of the H I Absorption Features at Low Resolution	82

List of Figures

1.1	A graph illustrating the generation of synchrotron radiation	10
1.2	A graph illustrating the H I 21 cm hyperfine transition	11
1.3	The Very Large Array (VLA) radio telescope	12
1.4	The Very Long Baseline Array (VLBA) radio telescope	13
1.5	The 305-m Arecibo radio telescope	14
1.6	Optical images of the Perseus cluster and NGC 1275 (Perseus A)	15
1.7	Infrared image of IRAS 17208–0014 with the HST NICMOS camera	16
1.8	Optical images of Hickson 96 (H96) compact galaxy group and NGC 7674 (H96a)	17
2.1	Continuum image of 3C 84 at 1383 MHz	29
2.2	H I optical-depth spectra obtained in various regions against the background continuum source 3C 84 at 1383 MHz	30
2.3	Gray-scale and contour H I optical depth channel images toward 3C 84 in the velocity range 8127.0–8106.2 km s ^{−1}	31
2.4	Gray-scale and contour H I optical depth channel images toward 3C 84 in the velocity range 8135.7–8128.8 km s ^{−1}	32
2.5	Gray-scale and contour N_{HI}/T_s images	33
3.1	Low resolution continuum image of the central region in IRAS 17208–0014 at 1362 MHz	52
3.2	High resolution continuum image of the central region in IRAS 17208–0014 at 1362 MHz	53
3.3	Hanning smoothed H I optical depth spectra obtained at various locations against the background continuum source IRAS 17208–0014 at 1362 MHz	54
3.4	Gray-scale and contour H I optical depth channel images toward IRAS 17208–0014 in the velocity range 13,170.3–12,539.0 km s ^{−1}	55
3.5	Position-velocity plots of the H I 21 cm absorption along two cuts in position angle 52°	56
3.6	H I velocity field and H I position-velocity plot (P.A. 120°)	57
4.1	Continuum images of the nuclear region in NGC 7674 at 20 and 11 × 5 mas resolution	83
4.2	Gray scale continuum image of the central (<i>left</i>) and western (<i>right</i>) components in NGC 7674 at 11 × 5 mas resolution	84

4.3	Continuum image of the nuclear region in NGC 7674 at 1380 MHz and 92×76 mas resolution	85
4.4	H I absorption spectra obtained at various locations against the central (<i>top</i>) and the western (<i>bottom</i>) components of NGC 7674 at 1380 MHz	86
4.5	High resolution gray-scale and contour H I optical depth channel images toward the central component in NGC 7674 in the velocity range 8626.7–8529.0 km s ⁻¹	87
4.6	Velocity field and position-velocity plot (P.A. 14°) of the strongest H I absorption in NGC 7674 at high spatial resolution	88
4.7	High angular resolution N_{HI}/T_s images in the velocity range 8626.7–8529.0 km s ⁻¹	89
4.8	H I absorption spectra averaged against the continuum components of NGC 7674 at 1380 MHz and low spatial resolution	90
4.9	Low resolution gray-scale and contour H I optical depth channel images toward the central, eastern, and northeastern components in NGC 7674 in the velocity range 8626.7–8522.0 km s ⁻¹	91
4.10	Low angular resolution N_{HI}/T_s images in the velocity range 8626.7 – 8522.0 km s ⁻¹	92
4.11	Velocity field of the H I absorption at low spatial resolution, and the integrated H I 21 cm absorption profile against the whole region where H I absorption is detected at low spatial resolution	93

List of Files

EMthesis.pdf (PDF file, 7.25 MB)

Chapter 1

Introduction

It has become clear in recent years that galaxies are not isolated “island universes”, and that gravitational interactions between galaxies are far more common than previously believed. All galaxies appear to be grouped into clusters, small groups, or pairs. It is likely that they have formed, and continue to evolve, in interaction with their environment and neighboring galaxies. Multiwavelength studies show that galaxy interactions may have even more fundamental significance in astrophysics. The interactions and mergers of galaxies are able to trigger violent bursts of star formation as well as provide material to feed central massive black holes in galactic nuclei. Thus, the study of interacting/merging systems plays an important role in understanding astrophysical phenomena. For example, it provides information on the environment in which a significant fraction of the stars in the universe likely formed. Also, it provides an evolutionary connection between mergers and the formation of active galactic nuclei (AGN).

1.1 INTERACTING/MERGING GALAXIES

For many years, optical observations were the sole means of identifying interacting galaxies. Such identifications were based on the existence of tails and/or bridges, or other disturbed or peculiar morphologies. One of the best known optical catalogs that lists interacting/merging galaxies was that of Halton C. Arp in his “Atlas of Peculiar Galaxies” using the 200-inch Palomar telescope (Arp 1996). Another major work was “The Atlas

and Catalog of Interacting Galaxies” by Verontsov-Velyaminov (1959, 1977). However, such studies only selected the strongest and most obvious interactions.

The *Infrared Astronomical Satellite* (IRAS) mission revolutionized the study of interacting/merging galaxies. The IRAS survey, which was conducted in 1983 and covered 96% of the sky, revealed tens of thousands of galaxies which were too faint to have been included in previous optical catalogs. This survey discovered a significant number of galaxies emitting the bulk of their energy at infrared wavelengths (Houck et al. 1984, 1985; Soifer et al. 1984, 1986; Rieke & Lebofsky 1986). The trigger for the intense infrared emission from these galaxies appears to be the strong interaction/merger of molecular gas-rich spirals. At the highest luminosities ($L_{\text{IR}} > 10^{12} L_{\odot}$), nearly all objects are advanced mergers powered by a mixture of circumnuclear starburst and/or Active Galactic Nuclei (AGN). Both these energy sources are fueled by an enormous concentration of molecular gas that has been funneled into the merger nucleus (Sanders & Mirabel 1996; Genzel et al. 1998; Lutz et al. 1999). At luminosities above $10^{11} L_{\odot}$, these infrared galaxies comprise the dominant population of extragalactic objects in the local universe ($z \leq 0.3$; Mirabel & Sanders 1996). Based on their infrared luminosities, these galaxies have been further subdivided into Luminous IR Galaxies or LIRGs ($L_{\text{IR}} > 10^{11} L_{\odot}$), Ultra-Luminous IR Galaxies or ULIRGs ($L_{\text{IR}} > 10^{12} L_{\odot}$), and Hyper-Luminous IR Galaxies or HyLIRGs ($L_{\text{IR}} > 10^{13} L_{\odot}$).

The study of interacting/merging systems is essential to the understanding of two important phenomena in modern astronomy:

- Interactions and mergers seem to be the effective triggers for starburst activity in gas rich galaxies. Hence, they could provide information on the environment in which a significant fraction of the stars in the universe have formed.
- Interactions and mergers may represent an important stage in the chemical and morphological evolution of galaxies. Hence, they could provide a better understanding on the formation of ellipticals, quasi-stellar objects (QSOs), and powerful radio galaxies.

Interacting/merging galaxies in the local universe offer a valuable opportunity to address the above mentioned questions. Radio frequency observations represent one of the most effective means to study the structure and the kinematics of these systems. Such

observations are not affected by the dusty environments associated with these galaxies. Moreover, the Very Long Baseline Interferometry (VLBI) technique provides extremely high angular resolution for observing these sources.

In this thesis, three such interacting/merging systems are studied in detail using the VLBI technique. Observations of these galaxies were made at 1.4 GHz, both in the continuum and in 21 cm atomic hydrogen (HI) absorption. The radio continuum emission is due to synchrotron radiation, which is emitted by relativistic electrons spiraling around magnetic field lines (Figure 1.1). On the other hand, the 21 cm absorption line arises from a hyperfine transition in the ground state of atomic hydrogen. This state is split into two closely spaced sublevels through interaction between the magnetic moments of the proton and the electron. In the higher energy states the two magnetic moments are parallel, and the emission of a photon is associated with the change from the parallel orientation to antiparallel (Figure 1.2). The absorption is the opposite case. The energy separation between the two hyperfine sublevels of the ground state of the hydrogen atom corresponds to a frequency of $\nu = 1.4$ GHz.

1.2 VERY LONG BASELINE INTERFEROMETRY

The angular resolution of a telescope is equal to the observed wavelength divided by the diameter of the telescope. At radio wavelengths, which are the longest in the electromagnetic spectrum, very large diameter telescopes are required to obtain high spatial resolution. For example, the resolution of the human eye is about 0.5 arcmin. To achieve a similar resolution at 1.4 GHz (21 cm), a radio telescope with a diameter of about 1.7 km is needed.

In the 1950s, radio astronomers discovered that several antennas could be placed at various distances, and linked together to observe the same celestial object simultaneously. When the cosmic signals received at each one of the telescopes were brought to a correlator and added, the resulting angular resolution was then equivalent to that of a single dish with a diameter equal to the separation between the most distant antennas. This technique has been called radio interferometry, and the most famous example of a radio interferometer

is the Very Large Array (VLA) in New Mexico (Figure 1.3). The next logical step was to increase the separation between the antennas to even larger distances. However, the physical connection between the elements of the interferometer was no longer possible due to the practical difficulty of laying cables over such large distances. Thus, the science of Very Long Baseline Interferometry (VLBI) was born. In this technique, the radio signals at each telescope are recorded on magnetic tapes with very accurate time stamps. Later, these tapes are brought to a central facility for correlation.

1.2.1 The Very Long Baseline Array (VLBA)

The only full-time dedicated VLBI array in the world, and the main instrument used for the research presented in this thesis, is the Very Long Baseline Array (VLBA) operated by the National Radio Astronomy Observatory (NRAO). The array consists of ten identical antennas distributed over the United States from St. Croix (US Virgin Islands) in the east to Hawaii in the west (Napier et al. 1994; Napier 1995). Figure 1.4 shows the approximate geographic locations of the VLBA stations. Their two letter codes, location and coordinates are listed in Table 1.1. Each of the antennas has a diameter of 25 m, and provides an angular resolution as high as 0.1 milliarcsecond (mas) at 86 GHz. Table 1.2 lists the lengths of the 45 VLBA baselines. The antennas of the VLBA operate at nine frequencies ranging between 330 MHz and 86 GHz, and are controlled by the Array Operations Center (AOC) in Socorro, New Mexico. The VLBA correlator (Benson 1995, Romney 1999) is located at the AOC, and is designed to process all observations involving the ten VLBA antennas in addition to as many as ten other foreign stations.

The maximum angular resolution of the VLBA (θ_{HPBW}) in units of mas can be calculated using the following expression:

$$\theta_{\text{HPBW}} \text{ (mas)} \simeq 2063 \times \frac{\lambda}{B_{\text{max}}}, \quad (1.1)$$

where λ is the observed wavelength in cm, and B_{max} is the maximum baseline length in km. At 1.4 GHz (21 cm), for example, the maximum resolution of the VLBA is 5 mas.

Another quantity of interest for an interferometer is its sensitivity. The sensitivity can

be expressed as the r.m.s. noise limit that determines the weakest detectable feature. The sensitivity achieved with the VLBA for a dual circular polarization observation can be calculated using the following formula:

$$\Delta I \text{ (Jy beam}^{-1}\text{)} \simeq \frac{SEFD}{\sqrt{N \times (N - 1) \times \Delta\nu \times t_{int}}}, \quad (1.2)$$

where N is the number of observing antennas, $\Delta\nu$ is the total bandwidth per polarization for continuum data and the channel width for spectral line data in Hz, and t_{int} is the total observing time in units of seconds. The term $SEFD$ (system equivalent flux density) takes into account the efficiency and the collecting area of the antenna, as well as the system noise. The flux density of the weakest detectable source, for example, in a 10 hr observation with the VLBA at 1.4 GHz, using dual circular polarization and a typical bandwidth of 16 MHz per polarization, is $\sim 40 \mu\text{Jy beam}^{-1}$.

The concept of “brightness temperature”, commonly used in radio astronomy, can also be used to measure the sensitivity of a radio telescope. The brightness temperature (T_b) is defined as the Rayleigh-Jeans temperature of an equivalent black body which will give the same power per unit area per unit frequency interval per unit solid angle as the celestial radio source. For a source of flux density S , and solid angle Ω , the brightness temperature in units of Kelvin (K) is:

$$T_b \text{ (K)} = \frac{\lambda^2}{2k_B} \frac{S}{\Omega}. \quad (1.3)$$

Assuming a circular Gaussian beam with θ_{HPBW} of 10 mas, a flux density of $40 \mu\text{Jy beam}^{-1}$ (calculated in the example above), will correspond to a brightness temperature of 2.5×10^5 K.

The very small beam size of the VLBA allows us to observe and study compact sources, but the required high brightness temperature ($> 10^5$ K) limits the observable celestial objects to non-thermal radiation emitting sources. Some of the sources that have both these characteristics are AGNs, radio jets, radio supernovae, supernova remnants, and masers. However, the VLBA also allows us to observe the 21 cm neutral hydrogen line in absorption against high-brightness background continuum sources. This makes it possible to study the structure, the kinematics, and the distribution of neutral gas around AGNs

or starburst regions. Also, at frequencies of a few hundred MHz, free-free absorption can be studied if there is ionized gas in our line of sight to the synchrotron emitting region.

To further enhance the sensitivity and/or the resolution of the VLBA, stations such as the VLA, the 305-m Arecibo radio telescope (Figure 1.5), or stations from the European VLBI Network (EVN), can be used simultaneously with the VLBA. For example, the observations described in Chapter 1 were carried out with the VLBA, the phased VLA (Y27) and four EVN stations.

1.3 OVERVIEW OF THESIS PROJECTS

1.3.1 Chapter 2

The giant elliptical galaxy NGC 1275 is the dominant member of the Perseus cluster of galaxies (Figure 1.6). The systemic velocity of NGC 1275 is $\sim 5200 \text{ km s}^{-1}$. This galaxy has an active nucleus whose presence is revealed by one of the most powerful radio sources in the sky, 3C 84. Another velocity system with $\sim 8200 \text{ km s}^{-1}$ is also associated with NGC 1275. This high velocity system is located in front of NGC 1275, and is seen in 21 cm H I absorption toward 3C 84. The superposition of the foreground galaxy with the bright core of NGC 1275 provides an unusual opportunity to probe the properties and physical conditions of extragalactic neutral hydrogen clouds in what seems to be a highly disturbed late-type spiral galaxy colliding with a giant elliptical galaxy.

In this chapter we report on a detailed study of the high velocity H I absorption toward 3C 84. The observations were made at high spatial and spectral resolutions using a global VLBI array. We discuss the physical characteristics of the multiple H I absorption features that we observe in the high velocity object that appears to be falling toward the center of the Perseus cluster at 3000 km s^{-1} , and may be strongly interacting or even merging with NGC 1275.

1.3.2 Chapter 3

The Ultra-Luminous IR Galaxy (ULIRG) IRAS 17208–0014 is an advanced merging system. Optical images show two tidal tails attributed to a merger. The IR images reveal a very disturbed morphology and an extended but single nucleus suggesting a complete merger (Figure 1.7). This galaxy is thought to have formed by the merger of two spirals, and represents an observational proof that collision of galaxies can lead to a mass distribution similar to elliptical galaxies.

In this chapter, we report both continuum and H I absorption results on IRAS 17208–0014 with the VLBA and the phased VLA. The continuum results reveal an extreme nuclear starburst in this galaxy with no indication of a radio-loud AGN. Our H I absorption results show multiple features and a clear rotational behavior, suggesting a rotating H I disk or torus feeding the nuclear starburst in this galaxy.

1.3.3 Chapter 4

The galaxy NGC 7674 is the dominant member of the Hickson 96 compact galaxy group (Figure 1.8). This Luminous IR Galaxy (LIRG) is optically classified as a Seyfert type-2, and it is interacting with the nearby galaxies in the group. The VLA observations of Unger et al. (1988) at 15 GHz revealed a triple radio source in the nuclear region of this galaxy. However, their EVN observations at 20 mas resolution detected only two of the three components.

In this chapter we report a detailed study of the continuum emission from, and the H I absorption toward, the LIRG NGC 7674 at 1.38 GHz. The observations were carried out using the VLBA, the phased VLA, and the 305-m Arecibo radio telescope. Both the continuum and the H I absorption were imaged at various spatial resolutions. The results reveal several new continuum structures that seem to be related to the central AGN responsible for the Seyfert activity. We also discuss the physical characteristics of the H I absorption features that we observe at high (10 mas) and low (100 mas) angular resolutions.

Table 1.1: Locations of the VLBA Antennas

Code	Location	N Latitude ($^{\circ}$ ' ")	W Longitude ($^{\circ}$ ' ")	Elevation (m)
SC	Saint Croix, VI	17 45 30.57	64 35 02.61	16
HN	Hancock, NH	42:56:00.96	71:59:11.69	309
NL	North Liberty, IA	41:46:17.03	91:34:26.35	241
FD	Fort Davis, TX	30:38:05.63	103:56:39.13	1615
LA	Los Alamos, NM	35:46:30.33	106:14:42.01	1967
PT	Pie Town, NM	34:18:03.61	108:07:07.24	2371
KP	Kitt Peak, AZ	31:57:22.39	111:36:42.26	1916
OV	Owens Valley, CA	37:13:54.19	118:16:33.98	1207
BR	Brewster, WA	48:07:52.80	119:40:55.34	255
MK	Mauna Kea, HI	19:48:15.85	155:27:28.95	3720

Table 1.2: VLBA Baseline Lengths in km

	Sc	Hn	Nl	Fd	La	Pt	Kp	Ov	Br	Mk
Sc	—	2853	3645	4143	4458	4579	4839	5460	5767	8611
Hn	2853	—	1611	3105	3006	3226	3623	3885	3657	7502
Nl	3645	1611	—	1654	1432	1663	2075	2328	2300	6156
Fd	4143	3105	1654	—	608	564	744	1508	2345	5134
La	4458	3006	1432	608	—	236	652	1088	1757	4970
Pt	4579	3226	1663	564	236	—	417	973	1806	4795
Kp	4839	3623	2075	744	652	417	—	845	1913	4466
Ov	5460	3885	2328	1508	1088	973	845	—	1214	4015
Br	5767	3657	2300	2345	1757	1806	1913	1214	—	4398
Mk	8611	7502	6156	5134	4970	4795	4466	4015	4398	—

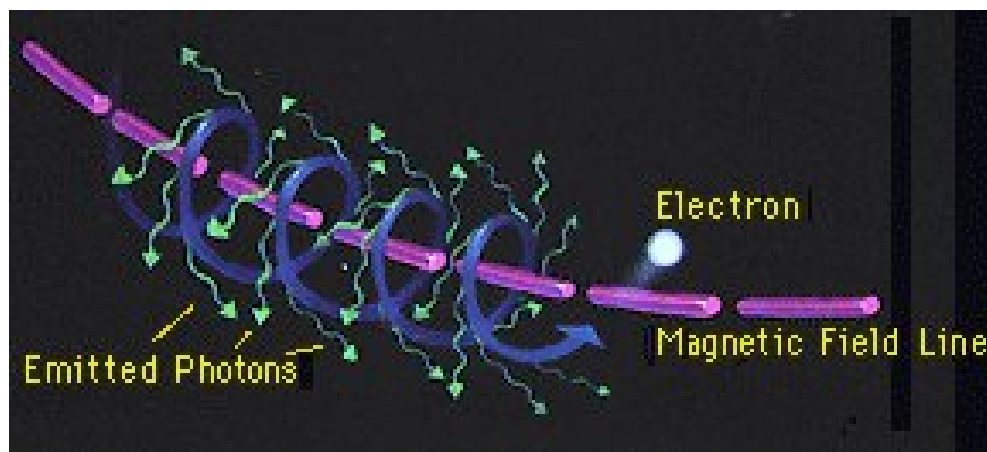


Figure 1.1: A graph illustrating the generation of synchrotron radiation. Image from http://imagine.gsfc.nasa.gov/docs/science/how_l2/xray_generation.html.

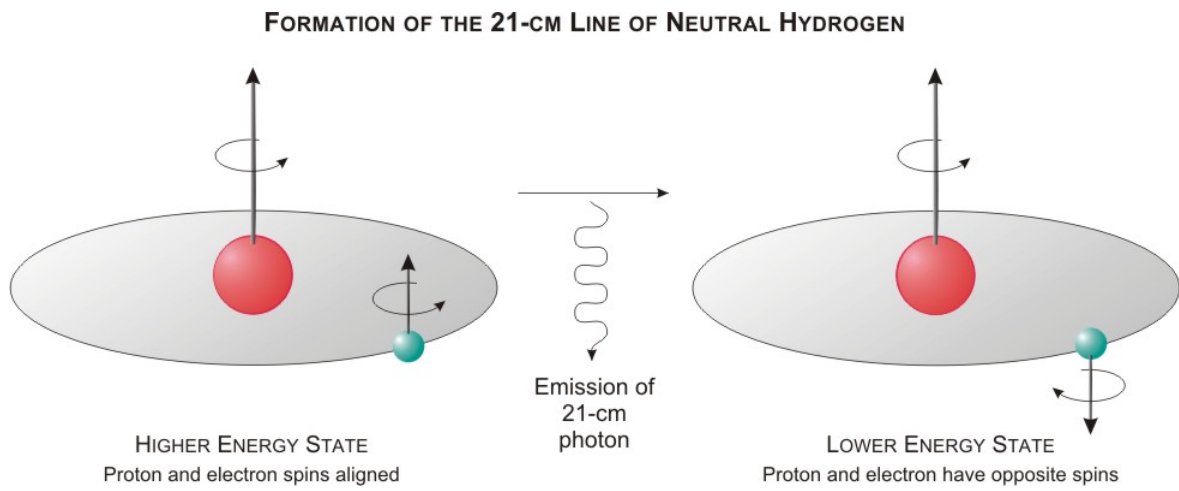


Figure 1.2: A graph illustrating the H I 21 cm hyperfine transition. Image courtesy of NRAO/AUI



Figure 1.3: The Very Large Array (VLA) radio telescope in Socorro, New Mexico, is a connected-element radio interferometer that consists of 27 antennas each with 25 m diameter. The images show the VLA at its most compact configuration (D Array), which has a maximum antenna separation of 1 km. The extended configuration of the VLA, known as A array, has a maximum antenna separation of 36 km, corresponding to an angular resolution of 50 mas at 43 GHz. Image courtesy of NRAO/AUI.

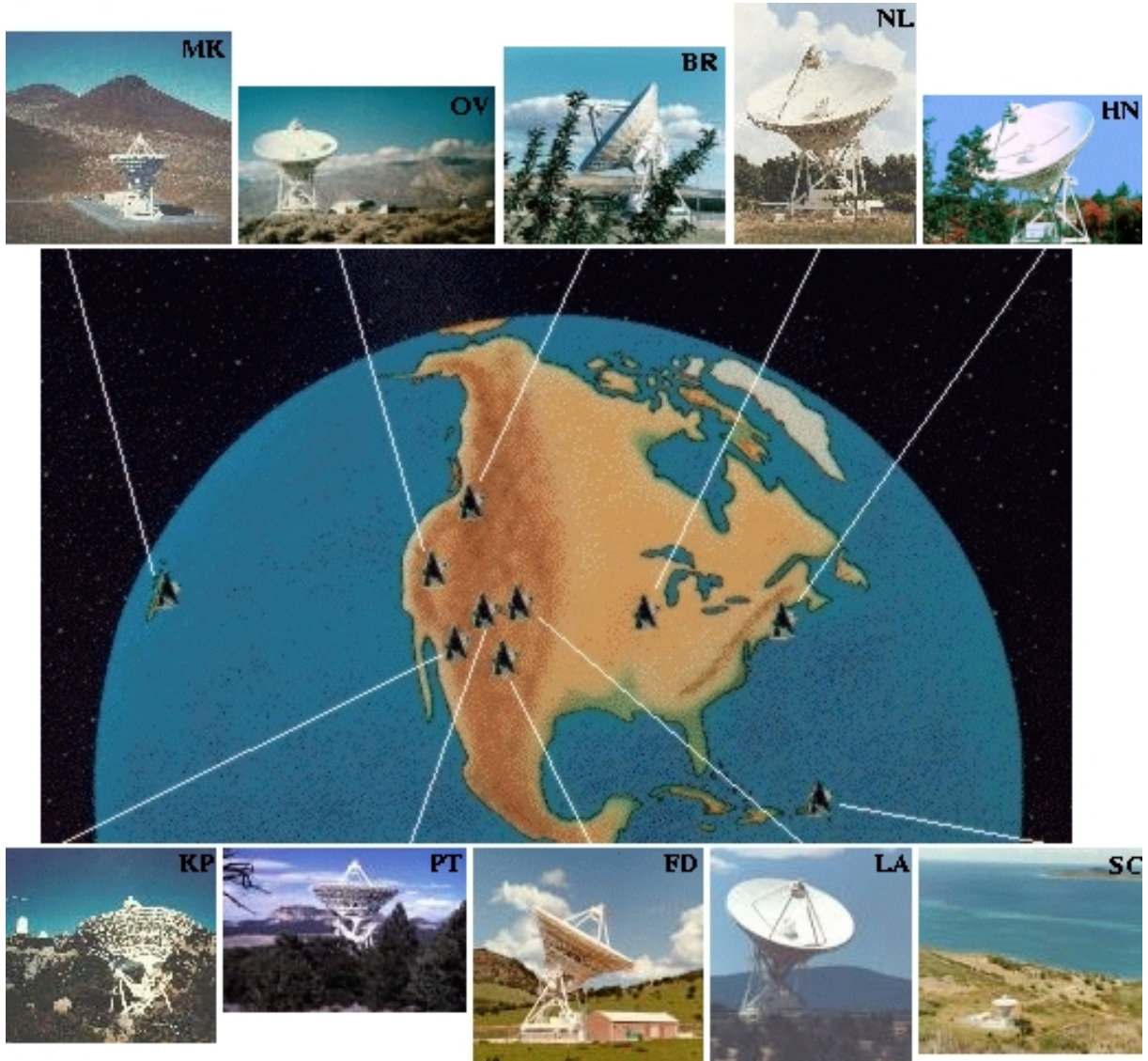


Figure 1.4: The Very Long Baseline Array (VLBA) radio telescope, is a full-time dedicated VLBI array that consists of 10 identical antennas, each 25 m in diameter. The elements of the array are spread out across North America from Hawaii to the US Virgin Islands. The antennas function together as one instrument resulting in an angular resolution as high as 0.1 milliarcsecond at 86 GHz. The two letter codes of the VLBA stations are given on the top-right side of each antenna image and are listed in Table 1.1. Image courtesy of NRAO/AUI.



Figure 1.5: The 305-m Arecibo radio telescope, the largest single-dish radio telescope in the world, is located in Puerto Rico. Image courtesy of the NAIC - Arecibo Observatory, a facility of the NSF.

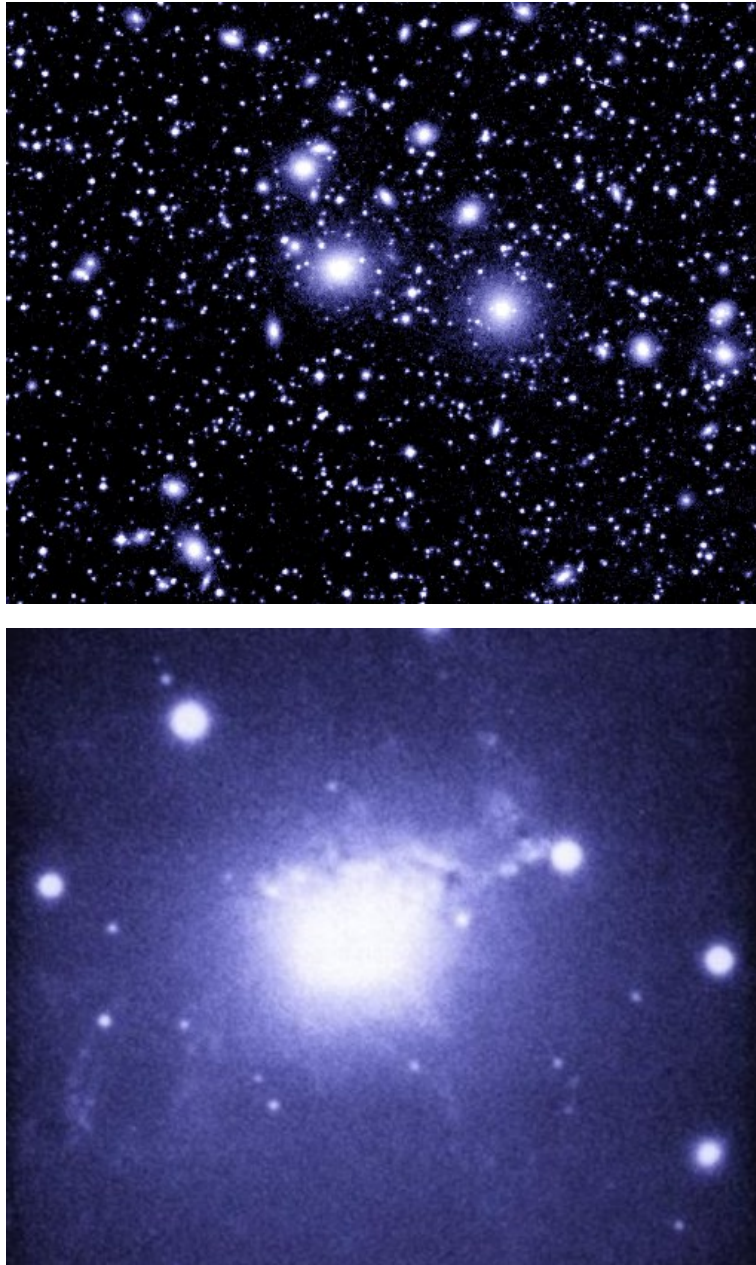


Figure 1.6: Optical images of the Perseus cluster and NGC 1275 (Perseus A). *Top*: Optical Image of the center of the Perseus Cluster obtained with the 0.9 meter telescope at KPNO (Cheng et al. 1997). *bottom*: Optical image of NGC 1275 (Perseus A) obtained with the 200 inch Palomar telescope (Sandage & Bedke 1994).

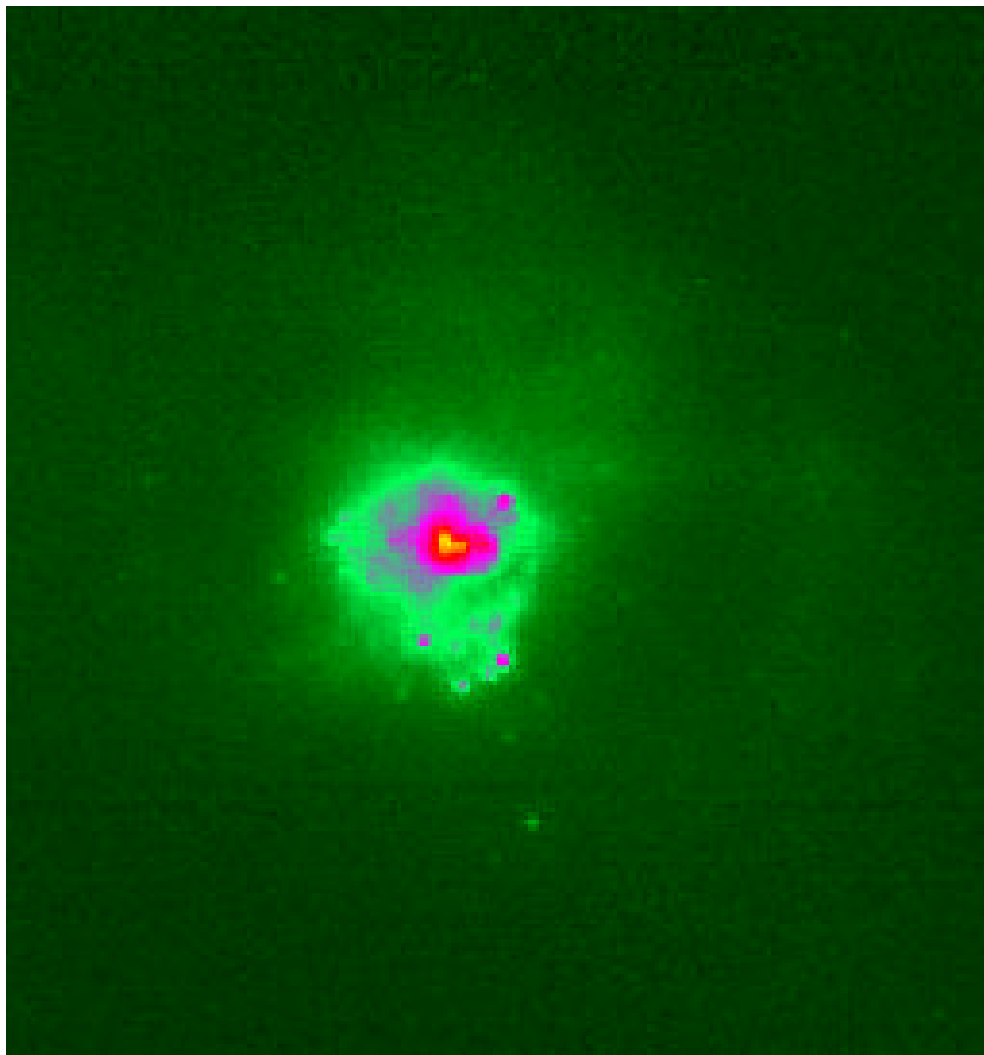


Figure 1.7: Infrared image of IRAS 17208–0014 with the HST NICMOS camera at $1.6\ \mu\text{m}$ (Scoville et al. 2000).

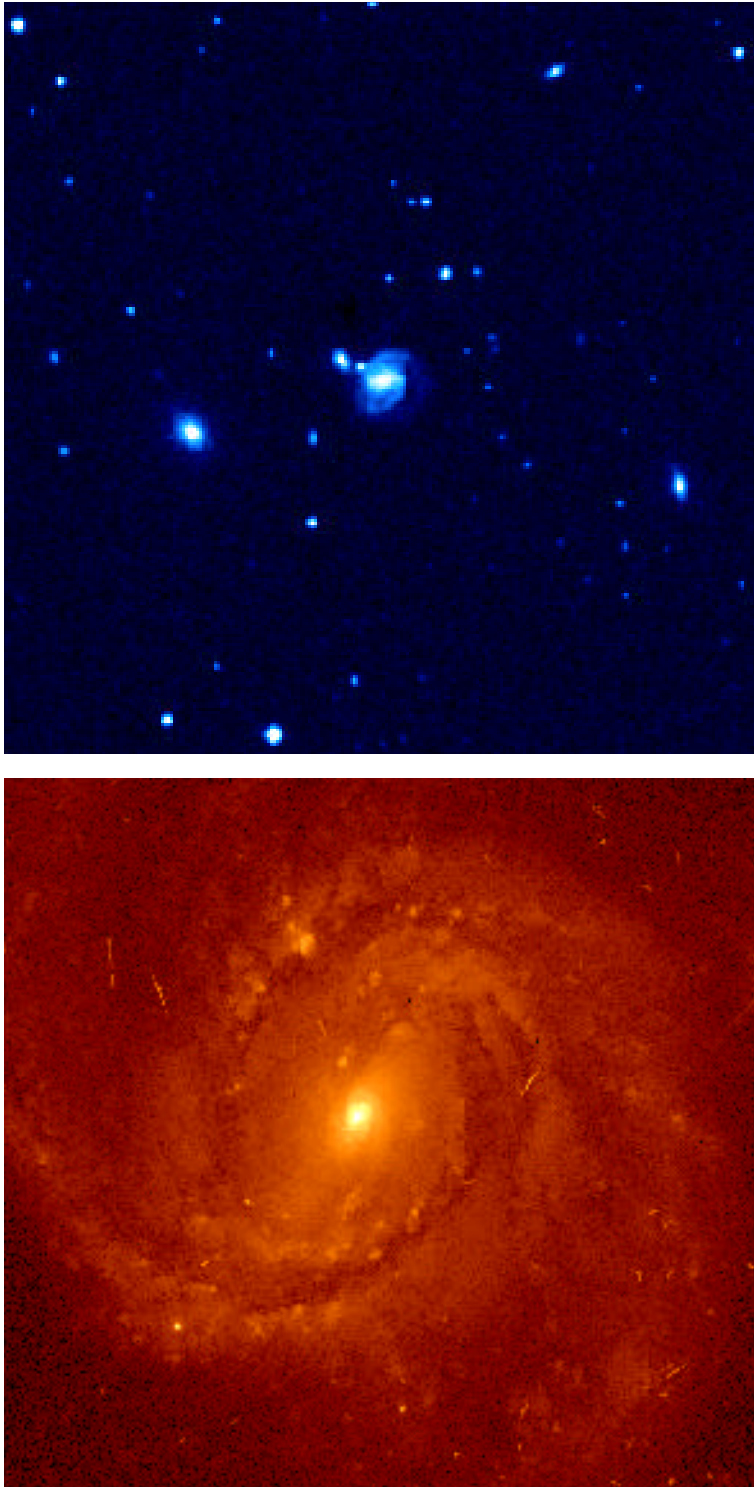


Figure 1.8: Optical images of Hickson 96 (H96) compact galaxy group and NGC 7674 (H96a). *Top*: Optical image of the Hickson 96 compact galaxy group (The Digitized Sky Survey). *bottom*: Optical image of NGC 7674 (H96a) obtained with the HST (Malkan, Gorjian, & Tam 1998).

Chapter 2

Global VLBI Observations of the High Velocity H I Absorption Toward NGC 1275¹

2.1 INTRODUCTION

NGC 1275 is a giant cD elliptical galaxy located near the center of the Perseus cluster, with a systemic velocity of $\sim 5200 \text{ km s}^{-1}$. The galaxy has an active nucleus whose presence is revealed by the powerful compact radio source 3C 84. Lying in front of NGC 1275 is another velocity system at $\sim 8200 \text{ km s}^{-1}$. This system is visible in H α emission (Caulet et al. 1992) as well as in 21 cm H I absorption (De Young, Roberts, & Saslaw 1973). The nature of the foreground system is unclear. It may be a late-type Sc or Sd galaxy whose H II regions account for the H α emission. However, no nucleus or other systematic morphological structure is apparent (Unger et al. 1990). Also, it is not known if the foreground system is in a chance alignment with NGC 1275 (Rubin et al. 1977, 1978) or if it is strongly interacting with the elliptical galaxy (Unger et al. 1990).

The H I absorption near 8116 km s^{-1} consists of several relatively narrow components ($1.5\text{--}5 \text{ km s}^{-1}$), similar in nature to Galactic H I absorption lines. (All velocities in this paper are heliocentric, using the optical convention for redshift.) The presence of such lines offers the opportunity to study spatial structure of the absorbing H I in the high-velocity system. However, radio continuum observations reported by Sijbring (1993) indicate that

¹Results presented in Chapter 2 have been published in the February 2002 edition of *The Astrophysical Journal* (vol. 566; p 195-201) by E. Momjian, J. D. Romney, & T. H. Troland.

76% of the 1395 MHz continuum flux arises in a milliarcsecond-scale core. Therefore, very long baseline interferometry (VLBI) techniques are essential. The first VLBI observations on this feature were performed by Romney (1978), who reported one strong absorption peak at 8114 km s^{-1} located between two wide absorption shoulders, with some indication of weaker absorption features. Only the strong peak was subject to detailed study, due to the limitations of the three element VLBI array and the equipment then available.

The completion of the Very Long Baseline Array (VLBA) in the early 1990s provided a new opportunity to study this H I absorption system. An early observation of this feature with the 10 stations of the VLBA was performed in 1995 as part of a wider project which also included the Galactic and the low-velocity H I absorption toward 3C 84 (J. E. Conway, J. D. Romney, M. Rupen, & A. J. Beasley, unpublished). Analysis of the high-velocity H I absorption feature by E. M. and J. D. R. produced interesting preliminary results. The poor quality of the original data, and the limited observing time, led us to propose new observations to study this absorption feature with a more sensitive VLBI array.

In this paper, we report a detailed study of the high-velocity H I absorption feature with a global VLBI array. Our results show the existence of several neutral hydrogen clouds in the intervening object, which is falling toward NGC 1275 at $\sim 3000 \text{ km s}^{-1}$. We adopt a distance of 104 Mpc for the Perseus cluster, assuming $H_0 = 50 \text{ km s}^{-1} \text{ Mpc}^{-1}$. At this distance, 1 mas corresponds to 0.49 pc.

2.2 OBSERVATIONS

The observations were carried out at 1383 MHz on 2000 February 19 using the VLBA², the VLA as a phased array, and four stations of the European VLBI Network, namely Effelsberg, Jodrell Bank (Lovell), Medicina, and the Westerbork phased array. Two different baseband channel widths were observed, wide (8 MHz) and narrow (0.5 MHz), both with right- and left-hand circular polarizations. Both bands were centered at the frequency of the neutral hydrogen 21 cm line at a heliocentric velocity of $V = 8114 \text{ km s}^{-1}$, and

²The National Radio Astronomy Observatory is a facility of the National Science Foundation operated under cooperative agreement by Associated Universities, Inc.

recorded using 2-bit sampling. The total observing time was 25 hr, with the first 11 hr being observed only by the EVN stations. The wide and the narrow-band data were correlated in separate passes at the VLBA correlator in Socorro, New Mexico with 4 second correlator integration time, to produce 16 and 256 spectral channels, respectively. Table 2.1 summarizes the parameters of these observations.

Along with 3C 84, the radio sources J0303+4716 and J0313+4120 were observed at the same frequencies for calibration purposes. Due to the lower flux densities of these two nearby calibrators compared to 3C 84, which is one of the strongest sources in the radio sky, calibration measurements were also obtained by shifting the narrow-band frequency of 3C 84 occasionally to an offset frequency 500 kHz (one bandwidth) higher, away from the H I absorption line. Both wide and narrow-band data were reduced and processed using the AIPS (Astronomical Image Processing System) package of NRAO.

Initial examination of the data showed the existence of interference in a wide frequency range at the EVN station Medicina at all times. All data from this station had to be abandoned. After many iterations, we found that amplitude self-calibration was essential in achieving high dynamic range images, and thus we also had to abandon the observations while the remaining three EVN stations were observing alone.

Wide-band channels were included in the observations to provide a high dynamic range continuum image for the background source 3C 84. After applying *a priori* flagging, and manually excising integrations affected by interference, we performed amplitude calibration using the measurements of the antenna gain and the system temperature (T_{sys}) of each station. Bandpass calibration was performed, and the spectral channels were averaged, self-calibrated, and imaged. The resulting continuum image has a dynamic range of 17,000.

The 256 spectral channels of the narrow-band data set were used to study the high-velocity H I absorption feature at high spectral resolution, with a channel separation of 0.43 km s^{-1} (1.95 kHz). This data set was reduced twice. Each reduction implemented a different amplitude calibration method for the purposes of comparison, and to obtain the best possible results from our observations. In the first reduction, as for the wide band, the amplitude calibration was based on the measured antenna gains and T_{sys} values. In the second reduction, the “template” spectrum method was utilized, obtaining ampli-

tude solutions by fitting a long-term averaged total-power spectrum of a specific antenna to short-term (20 min) intervals on the other stations and applying the solutions to the cross-power spectra. This method was originally developed for the calibration of VLBI spectral line observations using poorly calibrated antennas. The offset-frequency 3C 84 observations were used to correct the bandpass variations of the cross-power spectra in both data reduction methods. The source J0303+4716 was used for bandpass calibration of the total-power template spectrum.

The results reported in this chapter are based on the narrow-band data reduction that utilized the measured antenna gains and T_{sys} values for amplitude calibration. Consistent results were obtained for the template spectrum method, but it also introduced spectrally-dependent image artifacts which could not be corrected by the self-calibration process. The template method may provide superior results, however, when applied on stronger absorption or emission-line features.

The phase and amplitude corrections from the self-calibration of the wide band were applied on the narrow-band data sets. HI data cubes were constructed by subtracting the continuum in the UV-plane using the AIPS task “UVLSF”. Optical depth cubes were calculated from the continuum image and the inner 140 channels of each line cube as

$$\tau(\nu) = -\ln[1 - I_{\text{line}}(\nu)/I_{\text{continuum}}]. \quad (2.1)$$

2.3 RESULTS

2.3.1 The Continuum

Figure 2.1 is our continuum image of 3C 84 at 1383 MHz. The image was reconstructed with a grid weighting intermediate between natural and uniform (ROBUST = 0 in AIPS task “IMAGR”).

The source consists of a compact core and a jet extending to the south. An image of 3C 84 convolved to a larger beam size revealed the northern counterjet, which was

first discovered at 8.4 GHz (Walker, Romney, & Benson 1994) and 22 GHz (Vermeulen, Readhead, & Backer 1994), simultaneously. This northern feature was not detected at 1.7 GHz in a high dynamic range image by Biretta, Bartel, & Deng (1991); however, Silver, Taylor, & Vermeulen (1998) detected it at 1414 MHz. The extent and the flux density of the northern counterjet in our observations are consistent with the results of Silver, Taylor, & Vermeulen (1998).

The total flux density of 3C 84 in our observations is ~ 18 Jy, almost 4 Jy less than the total flux density reported by Taylor & Vermeulen (1996) at 1347 MHz and Silver, Taylor, & Vermeulen (1998) at 1414 MHz. Both these VLBA observations were carried out in 1995. A similar proportional decline in the flux density of this source is reported in the single dish monitoring observations between 1995 and 2000 at higher frequencies (H. D. Aller, M. F. Aller, G. E. Latimer, & P. A. Hughes, in preparation). The decline of the flux density of 3C 84 at the frequencies monitored has been continuous since 1982–1984.

2.3.2 The H I Absorption

Our study reveals the existence of several H I absorption peaks in the high-velocity system associated with NGC 1275. Figure 2.2 shows a continuum image of 3C 84 and Hanning smoothed spectra of H I optical depth at various locations against the continuum image. Six main absorption peaks can be distinguished in the spectra of Figure 2.2, with velocity widths of $1.5\text{--}5\text{ km s}^{-1}$ at half maximum. Weaker H I components are also evident in the velocity range $8128.77\text{--}8136.17\text{ km s}^{-1}$.

Figure 2.3 presents optical-depth images covering the velocity range $8127.0\text{--}8106.2\text{ km s}^{-1}$, in every other spectral channel. Because the signal-to-noise ratio in the optical-depth images is poor where the continuum is weak, these images are blanked in areas where the flux density in the background continuum image is below 1.2% of the peak value, i.e., less than 64 mJy beam^{-1} . These images explicitly show the variation of the H I distribution in the small section of the foreground galaxy which is seen against the bright compact background source. The shift in the neutral hydrogen opacity from west to east is apparent in the images that cover the velocity range $8119.2\text{--}8113.1\text{ km s}^{-1}$. This range represents

the velocity spanned by the strongest H I peak, which is centered at 8114 km s⁻¹.

Figure 2.4 shows optical-depth images similar to Figure 2.3, but with modified gray-scale and contour levels for the weakest H I components seen in the velocity range 8135.7–8128.8 km s⁻¹ of the spectra in Figure 2.2. These features are mainly seen against the weakest parts of the background continuum, with little optical depth toward the stronger regions.

Our study shows no evidence for absorption against the southern jet or the weaker northern counterjet of 3C 84, where the flux density is less than 40 and 7 mJy beam⁻¹, respectively.

Figures 2.5*a*–2.5*e* show images of N_{HI}/T_s for the velocity ranges 8128.3–8125.7, 8124.9–8120.1, 8119.2–8113.1, 8112.7–8110.1, and 8108.8–8104.9 km s⁻¹, respectively. These ranges of velocity correspond to the six strongest H I absorption features, which are marked with heavy solid lines in the spectra for regions I, II and VI of Figure 2.2, although they can also be seen in some of the other regions. The N_{HI}/T_s images are calculated by integrating over the optical-depth values in each velocity range, as

$$N_{\text{HI}}/T_s = 1.823 \times 10^{18} \int \tau(v) dv. \quad (2.2)$$

The velocity ranges in Figures 2.5*c* and 2.5*d* are limited so that the effect of the blending between the strongest peaks in regions I and II of Figure 2.2 is minimized. The velocity range of Figure 2.5*e* covers two H I absorption peaks that arise at different locations, one in the east and one in the south (regions II and VI in Figure 2.2).

Table 2.2 summarizes the physical characteristics of the six strongest H I absorption features observed against 3C 84. The velocities (col. [1]) refer to peaks of these features seen in the optical-depth spectra of Figure 2.2. The widths of these lines (col. [2]) are the approximate full widths at half maximum optical depth. N_{HI}/T_s of each peak (col. [5]) is obtained from the images in Figure 2.5. The volume densities (col. [7]) are deduced assuming spherically symmetric clouds with diameters equal to their observed transverse linear extents, and $T_s = 50$ K.

2.4 DISCUSSION

The strong background radio source covers an area of about 7 by 16 pc on the plane of the sky. This area represents a very small section of the high-velocity foreground galaxy, which has an extent of at least 25 kpc (Rubin et al. 1977, 1978; Unger et al. 1990; van den Bergh 1977). However, even in this very compact region, several H I absorption features have been identified.

The nature of the foreground galaxy remains unclear. Rubin et al. (1977, 1978) report an east-west velocity gradient of about 300 km s^{-1} in the foreground galaxy, suggesting an edge-on rotating spiral with $V_{\text{max}} = 150 \sin(i) \text{ km s}^{-1}$, which is not necessarily in collision with NGC 1275. However, the observations of Unger et al. (1990) show a velocity gradient in the north-south direction too, by about 100 km s^{-1} , and no evidence for spiral structure or a single well-defined nucleus. This means that the foreground galaxy is either an irregular galaxy, as was suggested by Oort (1976), or a late-type spiral galaxy, disturbed either by its passage through the intergalactic medium in the core of the cluster, or by its collision with NGC 1275 (Unger et al. 1990). The absence of continuum light from a nucleus or a disk (van den Bergh 1977) makes it difficult to determine the exact nature of this foreground galaxy.

Considering these possibilities for the structure of the intervening galaxy, we can conduct a comparison of the detected H I lines with the H I absorption in the Galaxy, as a well-studied spiral, and with H I absorption in the Large Magellanic Cloud (LMC), as the closest and best-known irregular galaxy.

For Galactic H I absorption lines detected against various background sources, we consider observations obtained with the Parkes single dish and Parkes two-element interferometer (Radhakrishnan et al. 1972; Goss et al. 1972), and with the VLA and the Arecibo-Los Caños interferometer (Garwood & Dickey 1989). The velocity widths of the Galactic H I absorption lines range over $1\text{--}17 \text{ km s}^{-1}$, the optical depths from $0.11\text{--}5.3$ and the derived column densities $(0.3\text{--}34) \times 10^{20} \text{ cm}^{-2}$. In all three papers, most velocity widths fall in a narrower range, $1\text{--}9 \text{ km s}^{-1}$.

In this comparison, we have excluded the VLBA observations of Galactic H I absorption

toward background radio sources (Faison et al. 1998; Faison & Goss 2001), where the linear extent of the H I clouds, between 3 and 100 AU, is much smaller than the extent of the H I structures in our observations.

The H I absorption lines in the LMC were observed with the Australia Telescope Compact Array (ATCA) (Dickey et al. 1994; Marx-Zimmer et al. 2000). Most of the H I absorption lines have velocity widths less than 1 km s^{-1} , and very few exceed 1.2 km s^{-1} . The optical-depth values range between 0.12 and 2.05.

In both galaxies, the Milky Way and the LMC, multi-component H I absorption features are detected against individual background sources. The optical depths measured in our extragalactic H I lines fall in the lower end of the optical depth ranges for both the Galaxy and LMC. While the velocity widths of the Galactic H I absorption features are close to the values seen in our observations, which range between 1.5 and 5 km s^{-1} , the features in the LMC tend to have narrower H I components, with most having widths less than 1 km s^{-1} .

2.5 CONCLUSIONS

We have reported the discovery of multiple H I clouds in the high-velocity ($\sim 8200 \text{ km s}^{-1}$) system associated with NGC 1275 = Perseus A, the dominant member of the Perseus cluster ($V_{\text{sys}} \sim 5200 \text{ km s}^{-1}$).

The background galaxy NGC 1275 is an early-type giant cD elliptical. Its compact core, known as 3C 84, has a total flux density of $\sim 18 \text{ Jy}$, and a linear extent of 16 pc on the plane of the sky at 1.38 GHz. Our observations show a decline of $\sim 4 \text{ Jy}$ in the total flux density of 3C 84 since 1995.

The nature of the foreground object remains uncertain. However, all studies suggest that it is a gas-rich galaxy. The detected H I lines appear to arise in “interstellar” type H I clouds within the foreground galaxy, and lie along our line of sight to the high-brightness source 3C 84.

The superposition of the foreground galaxy, which lacks a strong radio nucleus, with the bright core of NGC 1275, provides an unusual opportunity to probe the properties and

physical conditions of extragalactic neutral hydrogen clouds in a late-type galaxy. The results show close similarities between these extragalactic H I clouds, and clouds in both the Galaxy and LMC, detected against various background radio sources.

Table 2.1: Parameters of the Global VLBI Observations of NGC 1275

Parameter	Value
Frequency	1383 MHz
Observing Date	2000 February 19
Total observing time	25 hr
R.A. (J2000)	03 ^h 19 ^m 48 ^s .160
Dec. (J2000)	+41°30′42″.105
Continuum data bandwidth	8 MHz
Continuum image rms	330 μ Jy beam ⁻¹
Line data bandwidth	0.5 MHz
Line data velocity coverage	8058 to 8169 km s ⁻¹
Line velocity resolution	0.43 km s ⁻¹
Line image rms	1.5 mJy beam ⁻¹
Optical depth image cutoff	64 mJy beam ⁻¹
Angular to linear scale ^a	1 mas = 0.49 pc

NOTES: (a) Assumes distance of 104 Mpc, and $H_0 = 50$ km s⁻¹ Mpc⁻¹.

Table 2.2: Parameters of the High Velocity H I Clouds in NGC 1275

Velocity ^a	Δv_{FWHM} ^b	τ_{peak}	Linear Size	N_{HI}/T_s	N_{HI} ^c	n ^d
(km s ⁻¹)	(km s ⁻¹)		(pc)	(cm ⁻² K ⁻¹)	(cm ⁻²)	(cm ⁻³)
(1)	(2)	(3)	(4)	(5)	(6)	(7)
8126.2	1.5	0.14	15	1.3×10^{18}	6.5×10^{19}	1.4
8121.8	3.5	0.30	13	5.2×10^{18}	2.6×10^{20}	6.5
8114.0	5.0	0.45	10	7.6×10^{18}	3.8×10^{20}	11.2
8112.2	3.5	0.38	9	3.4×10^{18}	1.7×10^{20}	6.1
8108.3	1.5	0.10	5	0.7×10^{18}	3.5×10^{19}	2.3
8106.6	3.5	0.15	6	2.4×10^{18}	1.2×10^{20}	6.5

NOTES: (a) Heliocentric velocity of the H I absorption feature at τ_{peak} .

(b) Full width at half optical depth.

(c) Based on $T_s = 50$ K.

(d) Assumes spherically symmetric clouds and $T_s = 50$ K.

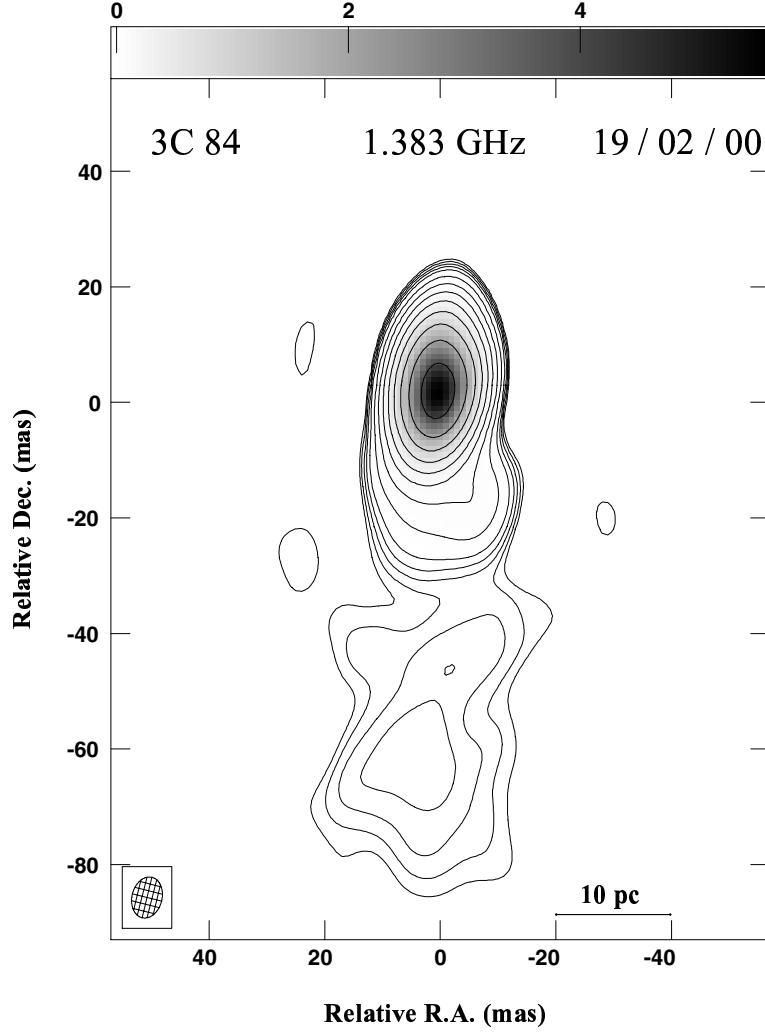


Figure 2.1: Continuum image of 3C 84 at 1383 MHz with its southern jet. The restoring beam has dimensions 7.2×5.2 mas in position angle -14° . The peak flux is $5.58 \text{ Jy beam}^{-1}$, and the contour levels are at 4, 5.7, 8, 11, 16, 32, 64, ..., 4096 mJy beam⁻¹. The gray scale range is indicated by the step wedge at the top of the image. The reference position (0,0) is $\alpha(\text{J2000}) = 03^{\text{h}}19^{\text{m}}48^{\text{s}}.160$, $\delta(\text{J2000}) = 41^\circ30'42''.105$.

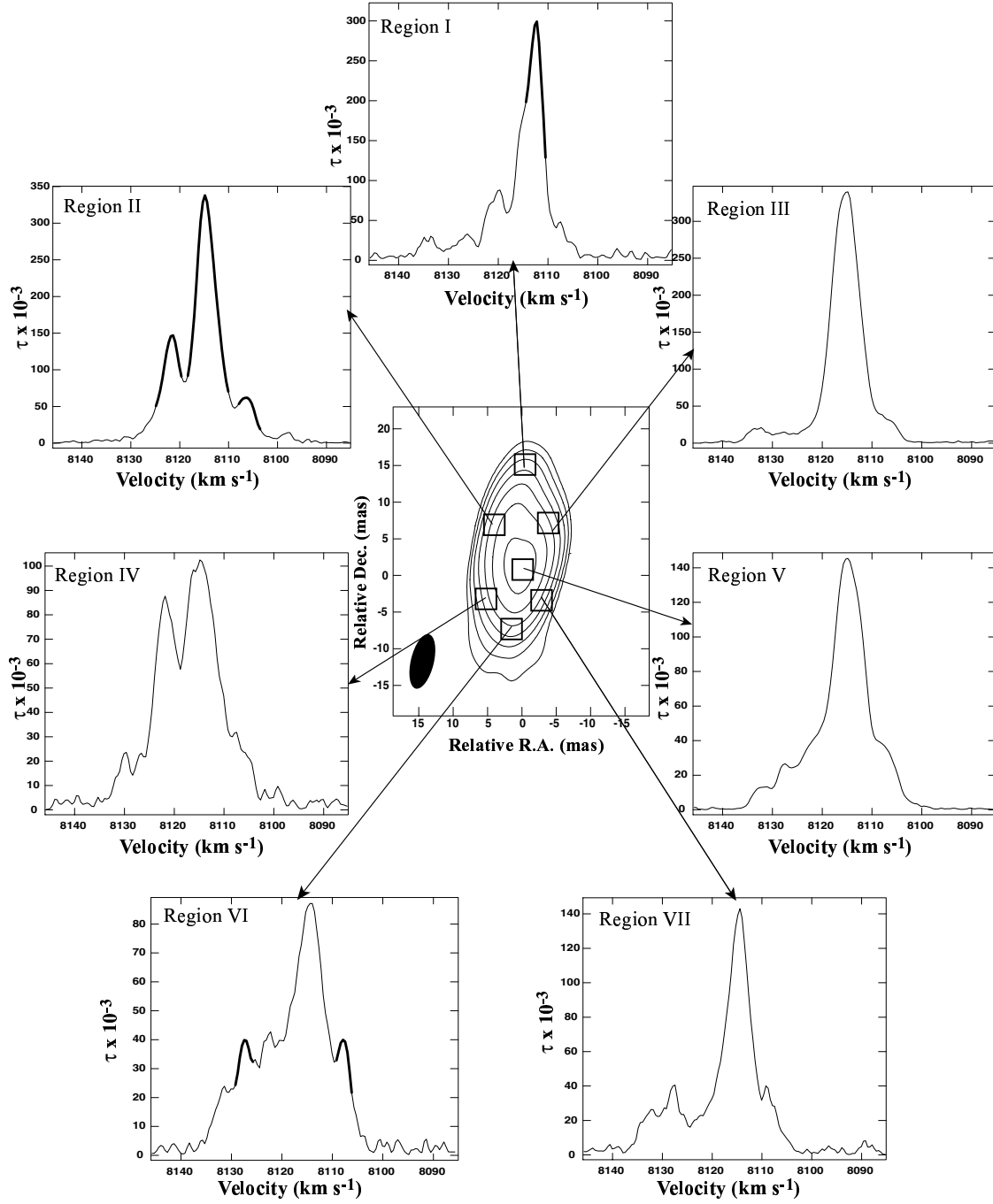


Figure 2.2: H I optical-depth spectra obtained in various regions against the background continuum source 3C 84 at 1383 MHz. The restoring beam is 7.66×3.25 mas in position angle -14.56° . The contour levels are at 64, 128, 256, ..., 4096 mJy beam $^{-1}$. Heavy lines denote the six major absorption components seen toward the background radio continuum, in the regions where they are most evident.

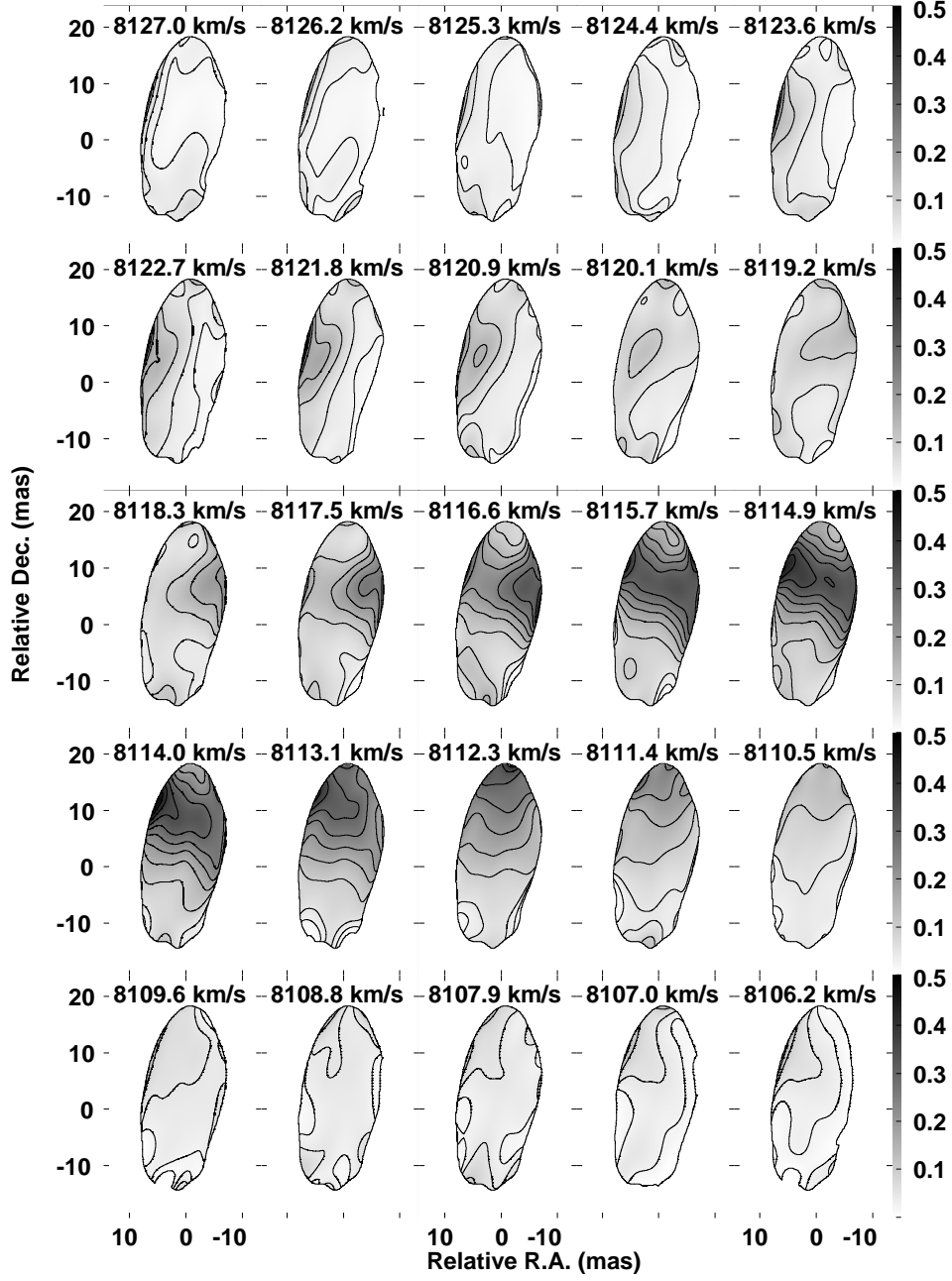


Figure 2.3: Gray-scale and contour HI optical depth channel images toward 3C 84 in the velocity range 8127.0–8106.2 km s⁻¹, with every other channel being displayed. The restoring beam in these images is 7.66×3.25 mas. The gray-scale range is indicated by the step wedge at the right side of the images; the contour levels are 0.025, 0.5, 0.1, 0.15, ..., 0.5.

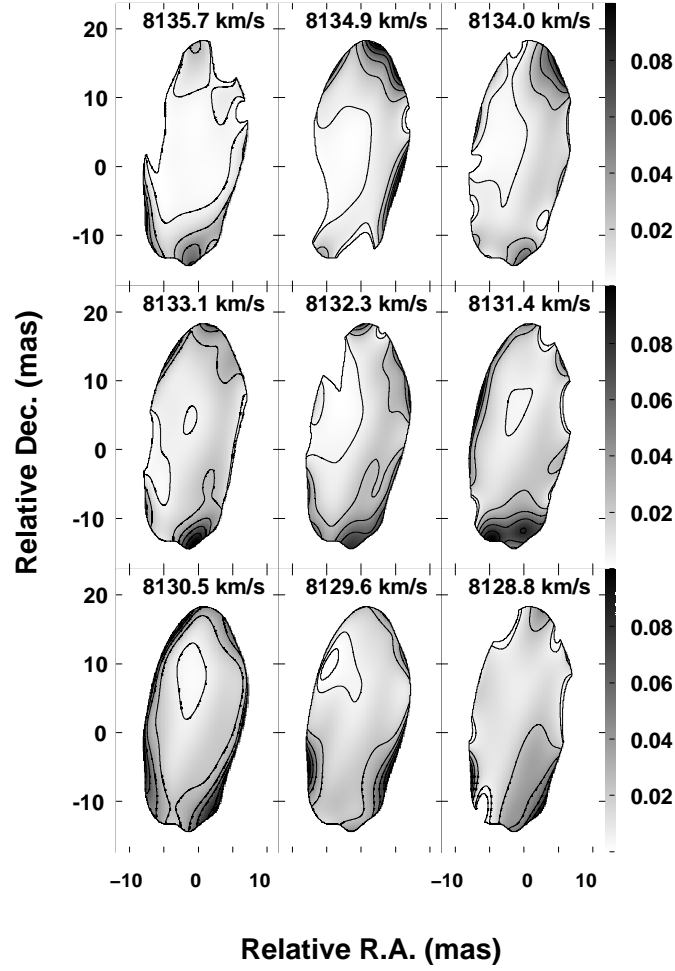


Figure 2.4: Gray-scale and contour H I optical depth channel images toward 3C 84 in the velocity range 8135.7–8128.8 km s⁻¹, with every other channel being displayed. The restoring beam is 7.66×3.25 mas. The gray-scale range is indicated by the step wedge at the right side of the images; the contour levels are 0.005, 0.025, 0.045, 0.065, and 0.085.

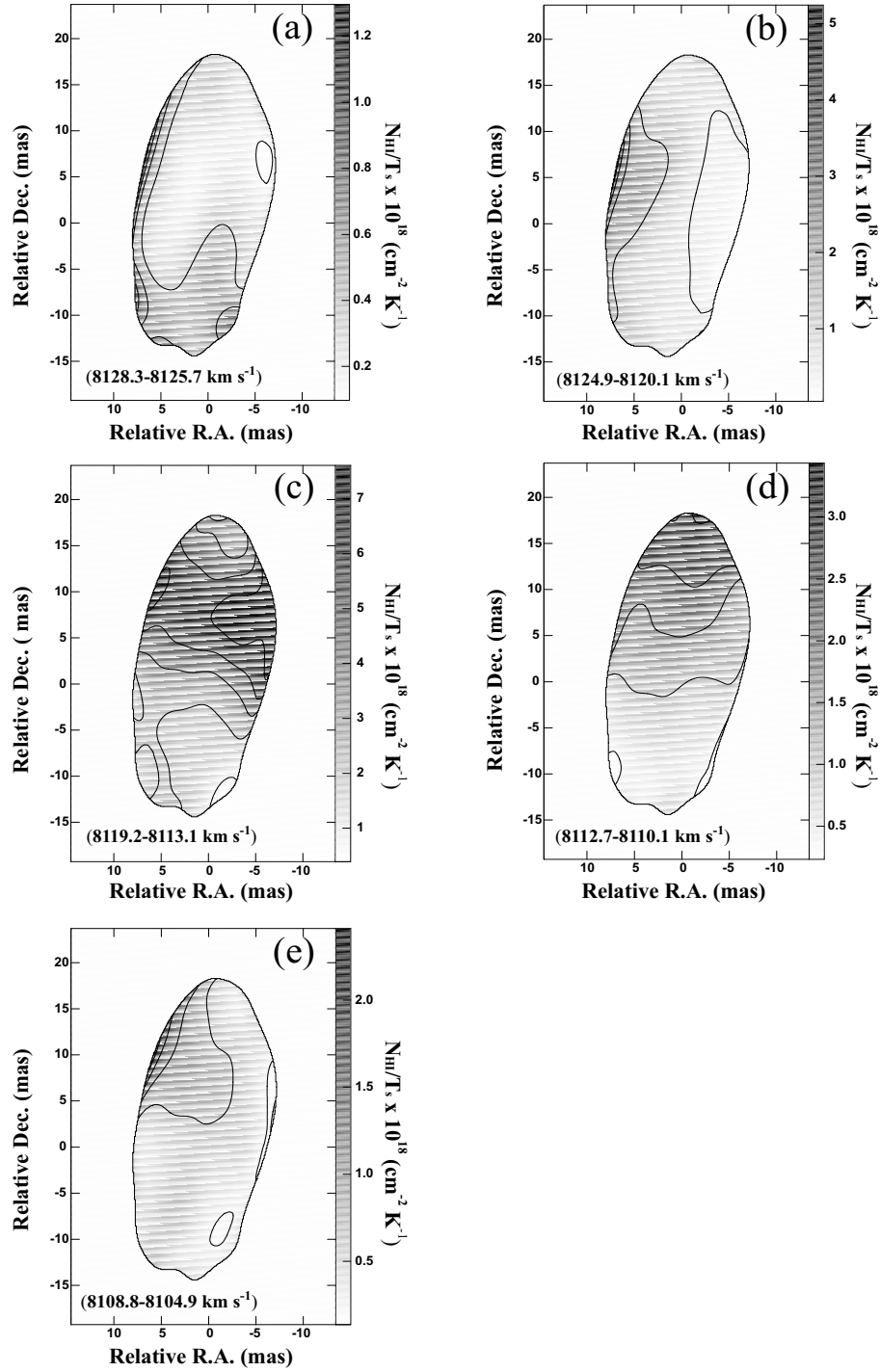


Figure 2.5: Gray-scale and contour N_{HI}/T_s images for the velocity ranges (a) 8128.3–8125.7 km s^{-1} , (b) 8124.9–8120.1 km s^{-1} , (c) 8119.2–8113.1 km s^{-1} , (d) 8112.7–8110.1 km s^{-1} , and (e) 8108.8–8104.9 km s^{-1} . The contour levels are 10, 30, 50, 70, and 90% of the peak value indicated by the step wedge at the right side of each map. The restoring beam in these images is $7.66 \times 3.25 \text{ mas}$.

Chapter 3

Sensitive VLBI Continuum and H I Absorption Observations of the Ultra-Luminous Infrared Galaxy IRAS 17208–0014¹

3.1 INTRODUCTION

At luminosities above $10^{11} L_{\odot}$, infrared galaxies become the most numerous objects in the local universe ($z \leq 0.3$; Sanders & Mirabel 1996). The trigger for the intense infrared emission appears to be the strong interaction or merger of molecular gas-rich spirals. Galaxies at the highest infrared luminosities [$L_{\text{IR}}(8 - 1000 \mu\text{m}) \geq 10^{12} L_{\odot}$], known as Ultra-Luminous and Hyper-Luminous Infrared Galaxies (ULIRGs & HyLIRGs), appear to be advanced merger systems and may represent an important stage in the formation of quasi-stellar objects (Sanders et al. 1988; Sanders & Mirabel 1996).

The bulk of the energy radiated by these sources is infrared emission from warm dust grains heated by a central power source or sources. The critical question concerning these galaxies is whether the dust is heated by a nuclear starburst, or an active galactic nucleus (AGN), or a combination of both. Mid-IR spectroscopic studies on a sample of ULIRGs by Genzel et al. (1998) suggest that 70%–80% of these galaxies are powered predominantly by recently formed massive stars, and 20%–30% by a central AGN. These authors conclude further that at least half of these ULIRGs are probably powered by both an AGN and a

¹Results presented in Chapter 3 have been published in the April 2003 edition of The Astrophysical Journal (vol 587; p. 160-170) by E. Momjian, J. D. Romney, C. L. Carilli, T. H. Troland, & G. B. Taylor.

starburst in a 1–2 kpc diameter circumnuclear disk or ring. The most direct evidence to date of sub-kpc nuclear starburst regions in ULIRGs is the discovery of luminous radio supernovae (RSNe) and supernova remnants (SNRs) in both Arp 220 (Smith et al. 1998b) and Mrk 273 (Carilli & Taylor 2000) using VLBI observations.

In this chapter, we present VLBI continuum and H I absorption observations of the ULIRG IRAS 17208–0014 at $z = 0.0426$. This galaxy has an infrared luminosity of $L_{\text{IR}} = 2.5 \times 10^{12} L_{\odot}$, as defined in Goldader et al. (1995).

Optical images of IRAS 17208–0014 at 6550 Å show two tidal tails from a merger (Melnick & Mirabel 1990; Murphy et al. 1996), and its optical spectrum resembles that of an H II region (Veilleux et al. 1995; Soifer et al. 2000). Its near-IR images show a very disturbed morphology and an extended but single nucleus, suggesting a complete merger (Zenner & Lenzen 1993; Murphy et al. 1996). Higher resolution near-IR images reveal numerous extremely luminous clusters in the inner 1 kpc, with no direct evidence of an AGN (Scoville et al. 2000). Infrared observations, in general, suggest that this galaxy represents the extreme of starburst dominated sources of this type (Soifer et al. 2000), and an observational proof that a collision of galaxies can lead to a mass distribution similar to elliptical galaxies (Zenner & Lenzen 1993).

The CO (1–0) emission observations of IRAS 17208–0014 by Downes & Solomon (1998) show a source of size $1''.8 \times 1''.6$ at full width half maximum (FWHM), and a strong velocity gradient with a change of 400 km s^{-1} over $1''.5$ in position angle 120° . The enclosed dynamical mass estimated from the CO observation is $8.5 \times 10^9 M_{\odot}$.

IRAS 17208–0014 also exhibits OH megamaser activity (Martin et al. 1989) at 1665, 1667, and 1720 MHz. The strongest emission is in the 1667 MHz line, with a luminosity of $L_{\text{OH}} = 10^3 L_{\odot}$. MERLIN 1662 MHz radio continuum observations at $0''.3$ resolution (Martin et al. 1989) revealed the existence of an unresolved component on the longest baselines, with a constant visibility amplitude of $\sim 35 \text{ mJy}$. However, the continuum emission from this galaxy was not detected in the 18 cm global VLBI observations by Diamond et al. (1999) to a limit of $3 \sigma = 210 \mu\text{Jy beam}^{-1}$.

Single dish observations by Martin et al. (1989) at Nançay showed the existence of a very wide H I absorption line in this galaxy, with full velocity widths of 650 and 695 km s^{-1}

at 50% and 20% of the maximum depth, which is -12 mJy.

In this chapter, we report a detailed study of the HI 21 cm absorption and the radio continuum emission from IRAS 17208–0014. The results reveal the HI gas dynamics and the distribution of compact continuum sources, possibly composed of luminous RSNe and/or SNRs, in the nuclear region of this galaxy on subkiloparsec scales. We adopt a distance of 171 Mpc to this galaxy, assuming $H_0 = 75$ km s $^{-1}$ Mpc $^{-1}$. At this distance 1 mas corresponds to 0.76 pc.

3.2 OBSERVATIONS AND DATA REDUCTION

The observations were carried out at 1362 MHz on 2001 June 4, using NRAO’s ² Very Long Baseline Array (VLBA), and the phased Very Large Array (VLA) as an element. The bandwidth of the observations was 16 MHz, in each of right and left-hand circular polarizations, sampled at two bits and centered at the frequency of the neutral hydrogen 21 cm line, at a heliocentric redshift of $z = 0.0426$, or $cz = 12,790$ km s $^{-1}$. The data were correlated at the VLBA correlator in Socorro, New Mexico with 512-point spectral resolution per baseband channel and 2.6 second correlator integration time. The total observing time was 11 hr. An initial correlation was performed at the position reported by Diamond et al. (1999) for IRAS 17208–0014 in their 18 cm VLBI OH megamaser observations, but no emission was detected. A second and final correlation was done at the position reported by Martin et al. (1989) in their 18 cm OH megamaser and continuum observations with the VLA and MERLIN. This position, where strong fringes were detected, is about 5''5 different from the position reported by Diamond et al. (1999).

Data reduction and analysis were performed using the Astronomical Image Processing System (AIPS) and the Astronomical Information Processing System (AIPS++). Table 3.1 summarizes the parameters of these observations.

Along with the target source IRAS 17208–0014, the compact source J1730+0024 was observed as a phase reference with a cycle time of 120 seconds, 80 seconds on the tar-

²The National Radio Astronomy Observatory is a facility of the National Science Foundation operated under cooperative agreement by Associated Universities, Inc.

get source and 40 seconds on the phase reference. The source J1743–0350 was used for amplitude and bandpass calibration.

After applying *a priori* flagging and manually excising integrations affected by interference, we performed amplitude calibration using the measurements of the antenna gain and the system temperature of each station, and bandpass calibration. Different spectral averages generated two data sets, a one-channel continuum and a 124-channel line data set. The phase calibrator J1730+0024 in the continuum data set, was self-calibrated and imaged in an iterative cycle. The self-calibration solutions of J1730+0024 were applied on both the continuum and the line data of the target source IRAS 17208–0014.

The continuum data of IRAS17208–0014 were then deconvolved and imaged with various spatial resolutions by tapering the visibility data to reveal its continuum structure. Continuum signals were mainly detected on the short to moderate length baselines to the phased VLA (Y27). The H I absorption line was only detected on the shortest baselines to Y27, primarily on the Y27–Pie Town baseline. The continuum emission was subtracted from the spectral-line visibility data. The spectral-line data were then analyzed at various spatial and spectral resolutions and imaged by applying a two dimensional Gaussian taper falling to 30% at 500 k λ . Pairs of channels were averaged together to improve the sensitivity. The resulting velocity resolution of the H I images was 58 km s^{–1}, and the spatial resolution was 0".55 \times 0".35. An optical-depth $\tau(\nu)$ cube was calculated from the H I absorption image cube and a continuum image with a similar resolution as

$$\tau(\nu) = -\ln[1 - I_{\text{line}}(\nu)/I_{\text{continuum}}]. \quad (3.1)$$

The optical depth cube was blanked in areas where the flux density of the background continuum image is below 9.4% of the peak value, i.e., less than 3 mJy beam^{–1}.

3.3 RESULTS AND ANALYSIS

3.3.1 The Radio Continuum

Figure 3.1 is our moderate resolution continuum image of the central region in IRAS 17208–0014 at 1362 MHz, with 80 \times 63 mas (60.8 \times 47.9 pc) resolution, obtained by using the

CLEAN algorithm as implemented in the AIPS task IMAGR, with a grid weighting intermediate between natural and uniform (ROBUST = 0). A two dimensional Gaussian taper falling to 30% at $2\text{ M}\lambda$ in both u and v directions was applied on the visibility data. The radio continuum emission region has an extent of $670 \times 390\text{ pc}$ on the plane of the sky, with a total flux density of 52 mJy. We also reduced the VLA data from these observations, which were performed in the CnB configuration and yielded a resolution of $9''.5 \times 4''.5$. The total flux density of the source at this resolution is 100 mJy, consistent with the value measured by Condon et al. (1996) at 1.425 GHz with the VLA B array.

An important question regarding these observations is whether the extended emission is likely diffuse, or composed of many point sources as might be expected for a nuclear starburst. Due to the incomplete u - v coverage in VLBI observations, especially for a source at 0° declination, the CLEAN algorithm tends to generate spurious point sources when deconvolving extended emission regions at high resolution. On the other hand, it is plausible that the extended emission is indeed composed of mostly faint point sources, in view of the likely starburst nature of IRAS 17208–0014. To resolve this ambiguity, we tested two other imaging algorithms, the Multi-Scale CLEAN and the Maximum Entropy Method (MEM), by generating two artificial data sets in AIPS++ with the same u - v sampling, weights, and sky positions as our target source. Such simulations give us confidence in the reliability of the results obtained from the real observations. The first data set was composed of multiple point sources and an extended source, and the second was composed of three extended sources. While the MEM gave very poor images for the set with compact sources and relatively poor results on the set with large sources, the Multi-Scale CLEAN successfully imaged both data sets without exhibiting any tendency to generate spurious point sources. Thus, we imaged the actual observations of our target source at high resolution (Figure 3.2) using the Multi-Scale Clean algorithm as implemented in the AIPS++ tool IMAGER, with a grid weighting ROBUST = 0.

Figure 3.2 has a resolution of $36 \times 33\text{ mas}$ ($27.4 \times 25.1\text{ pc}$) and represents the same region as in Figure 3.1. The visibility data were tapered with a Gaussian function falling to 30% at $6\text{ M}\lambda$ in the u direction and $4.5\text{ M}\lambda$ in the v direction. The continuum source is resolved and consists of a diffuse component extending over $670 \times 390\text{ pc}$, punctuated by a

number of compact sources.

There are about 25 compact sources in this high resolution image with flux densities larger than $5 \sigma = 350 \mu\text{Jy beam}^{-1}$, but Table 3.2 lists only the seven strongest compact sources, with flux densities higher than $9 \sigma = 630 \mu\text{Jy beam}^{-1}$. We selected this conservative limit because only these sources were consistently reproduced in the total intensity and in the individual RR and LL images, with comparable flux densities. The remaining sources lacked this consistency.

The compact source parameters in Table 3.2 were obtained by fitting Gaussian functions using the tool IMAGEFITTER in AIPS++. The positions (col. [2]) are relative to the peak surface brightness. Column (3) lists the surface brightnesses of these source, and column (4) their integrated fluxes. Columns (5) and (6) are the major and minor axes of the Gaussians at FWHM, and column (7) are their position angles.

Phase-referencing observations allow the determination of the absolute position of the target source and its components, if any, from the position of the calibrator (Walker 1999). The peak emission in IRAS 17208–0014, which is $1043 \mu\text{Jy beam}^{-1}$, is found to be at $\alpha(\text{J2000}) = 17^{\text{h}}23^{\text{m}}21^{\text{s}}.9554$, $\delta(\text{J2000}) = -00^{\circ}17'00''.938$. In applying the phase-referencing technique, the accuracy of the calibrator position is important. The position of J1730+0024 was obtained from the Jodrell Bank–VLA Astrometric Survey (JVAS) of phase calibrators, with a position uncertainty of ~ 14 mas (Browne et al. 1998). I verified the reported position of this calibrator, as well as its structure and its VLBI flux density, with a short VLBA observation preceding our main observations.

3.3.2 The H I Absorption

The H I absorption detected against the whole structure of the continuum has a full width at 20% maximum of 696 km s^{-1} and is composed of several components. Figure 3.3 shows Hanning-smoothed spectra of H I optical depth averaged over various regions against the low-resolution continuum image of IRAS 17208–0014. Figure 3.4 presents optical depth images covering the velocity range $13,170.3\text{--}12,539.0 \text{ km s}^{-1}$. These images explicitly show the variation of the H I opacity against the nuclear region of IRAS 17208–0014. In the lower

panel of Figure 3.5, Figure 3.5*a* is the H I position-velocity (PV) plot along the major axis of the radio source (position angle 52°), and Figure 3.5*b* is a PV diagram along another cut parallel to the major axis, as shown in the continuum image at the upper panel of Figure 3.5. I distinguish five main absorption peaks in both the PV and the optical-depth images. Their velocity widths range between 58 and 232 km s $^{-1}$ at half maximum, with optical depths between 0.3 and 2.5. Table 3.3 summarizes the physical characteristics of these five H I absorption features. The velocities (col. [1]) refer to peaks of these features as seen in the optical-depth spectra. The widths of these lines (col. [2]) are the approximate full widths at half peak optical depth. N_{HI}/T_s of each peak (col. [4]) is calculated as

$$N_{\text{HI}}/T_s \text{ (cm}^{-2} \text{ K}^{-1}\text{)} = 1.823 \times 10^{18} \int \tau(v) dv. \quad (3.2)$$

The column densities N_{HI} (col. [5]) are derived assuming $T_s = 100$ K. The visual extinction of each feature as a function of the H I spin temperature A_v/T_s (col. [6]) is computed assuming a Galactic dust-to-gas ratio (Staveley-Smith, & Davies 1987), and the visual extinctions A_v (col. [7]) are also derived for $T_s = 100$ K.

Our analysis shows that the strongest velocity gradient in the H I absorption is along a position angle of 120° , and not along the major axis of the radio source. The top panel of Figure 3.6 is the H I absorption velocity field, the contours are in steps of 50 km s $^{-1}$ and cover a velocity range between 12,600 and 13,000 km s $^{-1}$. The bottom panel of Figure 3.6 is a PV plot along a cut where the strongest velocity gradient is seen (position angle 120°). This gradient is 453 km s $^{-1}$ over 360 mas (274 pc), i.e. 1653 km s $^{-1}$ kpc $^{-1}$.

The spatial resolution of the low-resolution continuum image and the H I images (Figures 3.3, 3.4, 3.5, and 3.6) is $0''.55 \times 0''.35$ (418×266 pc). The rms noise level of the H I image cube is 0.5 mJy beam $^{-1}$. All these images were reconstructed with natural grid weighting (ROBUST = 5 in AIPS task IMAGR).

3.4 DISCUSSION

3.4.1 The Radio Continuum

At a moderate resolution (Figure 3.1), the nuclear region of IRAS 17208–0014 is composed of large scale structures a few hundred milliarcsecond in size, with an average brightness temperature of 3×10^5 K. Our high resolution continuum results (Figure 3.2) show that the nuclear region is composed of a diffuse emission, covering an overall area of $0''.88 \times 0''.51$ (670×340 pc), punctuated by multiple bright compact sources with flux densities greater than 5 times the rms noise level, or $350 \mu\text{Jy beam}^{-1}$. At the full resolution of our array, this region is over-resolved and does not reveal any single dominant source with very high brightness temperature. This morphology resembles those of the starburst nuclei in M 82 (Muxlow et al. 1994; Pedlar et al. 1999), NGC 253 (Ulvestad & Antonucci 1997), Arp 220 (Smith et al. 1998b), Mrk 273 (Carilli & Taylor 2000), and III Zw 35 (Pihlström et al. 2001). The average size of these compact sources is 70×48 mas (53×37 pc), and their brightness temperatures are between $(2.2\text{--}6.6) \times 10^5$ K, indicating the emission is non-thermal and not from H II regions. The non-thermal emission in nuclear starburst galaxies is usually attributed to synchrotron radiation from electrons accelerated in supernova remnant shocks (Condon 1992).

3.4.1.1 The starburst and the star formation rate

A remarkably tight and linear correlation between the total radio continuum emission and the far-IR luminosities (L_{FIR}) is well known in “normal” galaxies where the main energy source is not due to a supermassive black hole (Condon 1992). The most obvious interpretation of this correlation is the presence of massive stars that both provide relativistic particles via supernova events, and heat the interstellar dust which radiates in FIR wavelengths (Helou, Soifer, & Rowan-Robinson 1985; Wunderlich & Klein 1988; Condon 1992).

The ratio of infrared to radio luminosity is expressed by the quantity q as defined by Helou et al. (1985):

$$q = \log \left(\frac{\text{FIR}/(3.75 \times 10^{12})}{S_{1.4 \text{ GHz}}} \right), \quad (3.3)$$

where FIR is given by:

$$\text{FIR} = 1.26 \times 10^{-14} (2.58 S_{60 \mu\text{m}} + S_{100 \mu\text{m}}). \quad (3.4)$$

For IRAS 17208–0014, the total flux density at 1.4 GHz is 100 mJy (this work), and the IR flux densities at 60 and 100 μm are $S_{60 \mu\text{m}} = 34.67$ Jy and $S_{100 \mu\text{m}} = 37.65$ Jy, respectively (Sanders et al. 1995). The resulting q is 2.63, reasonably consistent with the mean value of 2.34 for infrared-selected galaxies, and dispersion of ± 0.33 for galaxies with $L_{60 \mu\text{m}} > 10^{11} L_{\odot}$, obtained by Yun, Reddy, & Condon (2001). Values of q less than 1.64 would indicate the presence of a radio-loud AGN (Yun, Reddy, & Condon 2001). Thus, based on the radio-FIR correlation, it would appear that IRAS 17208–0014 is dominated by a starburst.

An estimate of the massive star formation rate (SFR) and the supernova rate for a starburst galaxy can be obtained in two independent ways. The first is a theoretical approach which assumes an initial mass function (IMF) (Scoville & Soifer 1991), and the second is based on an empirical relationship between the observed non-thermal radio flux density and the supernova rate in the Galaxy (Condon & Yin 1990).

For the theoretical approach, we assume a modified Miller-Scalo IMF of the form $\psi(M) \propto M^{-5/2}$. This function is truncated at $M_l \leq 1 M_{\odot}$ and $M_u \geq 100 M_{\odot}$ (Scalo 1986; Condon 1992; Smith, Lonsdale, & Lonsdale 1998). The models presented by Scoville & Soifer (1991) give the following relationship between the luminosity of the starburst and the SFR:

$$L_* = 1.18 \times 10^{10} \left(\frac{M_l}{1 M_{\odot}} \right)^{\alpha} \left(\frac{M_u}{45 M_{\odot}} \right)^{0.37} \left(\frac{\text{SFR}}{1 M_{\odot} \text{ yr}^{-1}} \right) \left(\frac{t_B}{10^8 \text{ yr}^{-1}} \right)^{0.67} L_{\odot}, \quad (3.5)$$

where M_l and M_u are the lower and upper mass limits for star formation, respectively, $t_B = 10^8$ yr is the lifetime of the starburst, and $\alpha = 0.23$ and 0.55 for $M_l < 1 M_{\odot}$ and $> 1 M_{\odot}$, respectively.

The supernova rate ν_{SN} of a starburst galaxy can be calculated from the star formation rate using the following expression from Smith et al. (1998b), that assumes the same IMF introduced above:

$$\nu_{\text{SN}} \simeq 0.33 (\text{SFR}) \frac{(M_u^{-3/2} - M_{\text{SN}}^{-3/2})}{(M_u^{-1/2} - M_l^{-1/2})} \text{ yr}^{-1}, \quad (3.6)$$

where $M_{\text{SN}} = 8 M_{\odot}$ for Type II supernovae.

To obtain the star formation and supernova rates in IRAS 17208–0014 ($L_{\text{FIR}} = 2.3 \times 10^{12} L_{\odot}$), we use the lower and upper mass arguments obtained for Arp 220, the prototype ULIRG, which has a very similar q value to IRAS 17208–0014. For Arp 220, an upper limit mass was set from free-free emission and $\text{Pa}\beta$ observations and the lower mass limit was set from the CO dynamical mass measurements and the adopted disk model (Smith et al. 1998b and references therein). These limits are $M_l = 5 M_{\odot}$ and $M_u = 28 M_{\odot}$. It has also been found that the far-IR luminosity is a good measure of the bolometric luminosity produced by fairly massive ($M \geq 5 M_{\odot}$) young stars (Condon 1992). Thus, with these mass limits, we can state that $L_* = L_{\text{FIR}}$. The resulting massive star formation rate (Equation 3.5) is $\text{SFR} \simeq 96 M_{\odot} \text{ yr}^{-1}$, and the supernova rate (Equation 3.6) is $\nu_{\text{SN}} \simeq 4.6 \text{ yr}^{-1}$.

As an alternative, we can derive these rates using the empirical approach of Condon & Yin (1990), which is based on the observed Galactic non-thermal luminosity (L_{NT}) and the supernova rate ν_{SN} . This relationship is

$$\left(\frac{L_{\text{NT}}}{10^{22} \text{ W Hz}^{-1}} \right) = 13 \left(\frac{\nu}{\text{GHz}} \right)^{-\alpha} \left(\frac{\nu_{\text{SN}}}{\text{yr}^{-1}} \right), \quad (3.7)$$

where $\alpha \sim 0.8$ is the non-thermal spectral index for “normal” galaxies. Our 52 mJy total VLBI flux density for IRAS 17208–0014, which is mostly non-thermal, corresponds to a luminosity of $1.81 \times 10^{23} \text{ W Hz}^{-1}$. From Equation (3.7), we get $\nu_{\text{SN}} \simeq 1.8 \text{ yr}^{-1}$, and from Equation (3.6) we get a massive SFR of $37 M_{\odot} \text{ yr}^{-1}$, assuming the mass constraints as for Arp 220.

These values are lower than the rates obtained from the far-IR luminosity by a factor of 2.6, and suggest that there might be non-thermal diffuse emission which is not detected by our VLBI array. As shown by Condon (1992), the observed fraction of thermal emission in “normal” galaxies is ≤ 0.1 at 1.4 GHz. Thus, a reasonable approximation would be to consider the total VLA flux density, which is 100 mJy, to be non-thermal. Then, following the above argument with the luminosity $3.48 \times 10^{23} \text{ W Hz}^{-1}$ that corresponds to the detected VLA flux density, we obtain $\nu_{\text{SN}} \simeq 3.4 \text{ yr}^{-1}$ and $\text{SFR} \simeq 71 M_{\odot} \text{ yr}^{-1}$. These values are more consistent with the rates obtained from the far-IR luminosity using similar mass limits, and support the suggestion that there is undetected diffuse flux in our VLBI

observations.

We averaged the rates obtained from both the far-IR luminosity and the VLA radio flux density to obtain our best estimates for the massive SFR in IRAS 17208–0014, $\sim 84 \pm 13 M_{\odot} \text{ yr}^{-1}$, and the supernova rate $\sim 4 \pm 1 \text{ yr}^{-1}$. The derived star formation and supernova rates are consistent with the rates in the ULIRG Arp 220, where Smith et al. (1998b) obtained an SFR of $50 - 100 M_{\odot} \text{ yr}^{-1}$, and a supernova rate of $1.75 - 3.5 \text{ yr}^{-1}$ in VLBI observations at 18 cm. Our supernova rate is much higher than the upper limit of 0.3 yr^{-1} that Ulvestad & Antonucci (1997) derived for the nearby starburst galaxy NGC 253 from higher-frequency VLA observations. Follow-up VLBI observations will make it possible to look for new sources (i.e., RSNe) to directly constrain both the supernova and the massive star formation rates in the nuclear starburst region of IRAS 17208–0014.

An estimate of the magnetic field strength and the pressure of the relativistic electrons responsible for the synchrotron radiation detected from the starburst region can be obtained by minimizing the summed energy in magnetic fields and relativistic particles (Miley 1980). The resulting magnetic field is $\sim 144 \mu\text{G}$, and the corresponding pressure is $\sim 6 \times 10^{-10} \text{ dyn cm}^{-2}$, indicating extreme physical conditions compared to the disks of spiral galaxies.

3.4.1.2 The nature of the compact sources

The VLBI continuum emission in IRAS 17208–0014 extends over a region of $670 \times 340 \text{ pc}$, and can be explained in part by synchrotron radiation from aged SNRs, but this region is also punctuated by a number of bright compact sources (Figure 3.2). The radio spectral luminosities of these sources range over $(1 - 10) \times 10^{21} \text{ W Hz}^{-1}$ at 1.362 GHz and are at least an order of magnitude greater than the brightest RSNe seen in M 82 (Muxlow et al. 1994; Pedlar et al. 1999), but comparable to the rare class of extreme luminosity RSNe characterized by SN 1986J in NGC 891 (Rupen et al. 1987) and SN 1979C (Weiler & Sramek 1988). More recently, a substantial population of such luminous RSNe was discovered in Arp 220 by Smith et al. (1998b), who suggest that the high luminosities of those RSNe may indicate denser environments, more massive progenitors, or stronger magnetic fields relative to typical RSNe.

The compact sources revealed in our observations are a few times brighter and larger in size than the RSNe reported in the ULIRGs Arp 220 (Smith et al. 1998b) and Mrk 273 (Carilli & Taylor 2000). Thus, we presume that the compact sources in the starburst region of IRAS 17208-0014 are clustered young SNRs and/or luminous RSNe. Support for the clumpy nature of the nuclear region in IRAS 17208-0014 is provided by the high-resolution near-IR images obtained with the *Hubble Space Telescope* NICMOS camera (Scoville et al. 2000). These images, with resolutions between $0''.11$ and $0''.22$, reveal numerous extremely luminous clusters of massive stars in the inner 1 kpc region of this galaxy.

Smith et al. (1998a) have fitted smooth Gaussian and clumped models of starburst distributions to the observed visibility functions of 11 luminous and ultraluminous IR galaxies. Their first conclusion was that starbursts with standard RSNe are incapable of producing the radio power and structure of these galaxies. For luminous RSNe models, the Gaussian fits represented the visibility function poorly, but the clustered models, which assumed simultaneous detonation of the RSNe within one clump, were more successful. Excluding poor solutions, the sizes of these clumps ranged over 1–15 pc in diameter, and the number of supernovae per clump was between 2 and 12. These clumps are at least two times smaller than the minimum sizes implied by the Gaussian fits to our compact sources (Table 3.2).

However, we cannot rule out the possibility that the compact sources in our high resolution image are mainly powered by very luminous individual RSNe. Smith et al. (1998b) fitted the following expression for the postmaximum light curve of luminous RSNe:

$$S_{\nu} = S_{\nu, \max} \left(\frac{\Delta t}{3 \text{ yr}^{-1}} \right)^{1.3}, \quad (3.8)$$

where $\Delta t = t - t_0$, and $t = t_0$ is the detonation time. Following their discussion, individual RSNe will lie above our 5σ detection level for 7 years. Given our adopted supernova rate of 4 yr^{-1} , we expect to see about 28 individual luminous RSNe, in remarkable agreement with the 25 compact sources revealed in our observations.

Future multi-epoch VLBI observations would determine which of the two above assumptions better explain the nature of the compact components in IRAS 17208-0014.

3.4.2 The H I Absorption

The wide H I absorption observed against the whole extent of the nuclear region in IRAS 17208–0014, with a full width of 696 km s^{-1} at 20% maximum, is common in ULIRGs. Similar wide absorption lines have been found in Arp 220 (Mirabel & Sanders 1988), Mrk 273 (Bottinelli et al. 1985), and Mrk 231 (Dickey 1982). The present observations are consistent with the Nançay 300 m meridian telescope observations by Martin et al. (1989), who found a broad H I absorption ($\Delta V_{20\%} = 695 \text{ km s}^{-1}$) centered at $12,790 \pm 10 \text{ km s}^{-1}$. The detected peak absorption flux density in our observations is -8.65 mJy , about 72% of the single-dish detection.

Our observations reveal the details of the H I absorption against the radio emission in IRAS 17208–0014 (Figures 3.3, 3.4, 3.5, and 3.6). The absorption is complex, and composed of five main features (Table 3.3). Three of them are wide ($\Delta V_{\text{FWHM}} = 174 - 232 \text{ km s}^{-1}$) with $\tau < 1$, and the other two relatively narrow ($\Delta V_{\text{FWHM}} = 58 \text{ km s}^{-1}$) with $\tau > 1$. These two narrow lines appear to be localized features on the east edge and the north-east side of the continuum emission region (Figure 3.4), suggesting the existence of quiescent H I clouds in the interstellar medium of the galaxy. The linear extent of these two features is $0.3 - 0.46 \text{ kpc}$, as seen in the optical depth images (Figure 3.4).

The PV diagram in position angle 120° (Figure 3.6-*bottom*), shows a strong velocity gradient of 453 km s^{-1} over $0''.36$ (274 pc). Assuming Keplerian motion, the enclosed dynamical mass is $2.3 \times 10^9 (\sin^{-2}i) M_\odot$, where i is the inclination angle. The rotational behavior of the H I and the derived dynamical mass are largely consistent with the results of CO (1 – 0) emission line observations (Solomon et al. 1997; Downes & Solomon 1998). The interferometric observations of the CO (1 – 0) by Downes & Solomon (1998) with IRAM at Plateau de Bure show a velocity gradient of 400 km s^{-1} over $1''.5$ at position angle 120° , and an enclosed mass of $8.5 \times 10^9 M_\odot$. The resolution of these observations was $5''.1 \times 1''.6$ in position angle 47° . In both H I absorption and CO (1 – 0) emission, the strongest velocity gradient is seen along the same direction (position angle 120°). The H I absorption results show a stronger velocity gradient ($1653 \text{ km s}^{-1} \text{ kpc}^{-1}$) compared to the CO (1 – 0) ($346 \text{ km s}^{-1} \text{ kpc}^{-1}$), suggesting that the H I disk represents the inner region of

a larger molecular disk. A similar model was proposed for the absorbing neutral hydrogen in Mrk 231, where the observed H I disk was identified as the inner region of the molecular gas seen in CO (1 – 0) emission (Carilli, Wrobel, & Ulvestad 1998).

It is likely that both atomic and molecular gas exist in the region where the H I absorption is detected. The emission detected in low spatial resolution (FWHM $5''.1 \times 1''.6$) CO observations arises from larger scales, and would not show variations on the scales seen in the H I absorption in IRAS 17208–0014.

The neutral hydrogen column densities of the observed absorption features are high, covering a range $(10.1 - 28.0)T_s \times 10^{19} \text{ cm}^{-2}$, where T_s is in kelvins. The corresponding visual extinctions A_v , assuming a Galactic dust-to-gas ratio, are between $0.066 T_s$ and $0.174 T_s$ mag. The discussion in Scoville et al. (1998) for Arp 220, with the infrared magnitudes obtained for IRAS 17208-0014 (Scoville et al. 2000), implies a visual extinction value of ~ 22 mag, comparable to the values derived from our H I column densities with a spin temperature of $T_s \sim 100$ K.

Our results show a very good agreement between the physical properties of the neutral H I in IRAS 17208–0014 and in the other ULIRGs previously observed in detail, namely Arp 220 (Mundell, Ferruit, & Pedlar 2001), Mrk 273 (Cole et al. 1999; Carilli & Taylor 2000) and Mrk 231 (Carilli, Wrobel, & Ulvestad 1998). The strong velocity gradients seen in the H I absorption of these galaxies suggest rapidly rotating disks which are obscuring the radio-emitting nuclear regions, while the multiple absorption features seen against different regions of the continuum indicate the existence of several discrete clouds in those disks.

3.5 CONCLUSIONS

We have presented the results of phase-referenced VLBI observations, using the VLBA and the phased VLA, of the 21 cm continuum emission and the H I absorption in the central ~ 1.1 kpc of the very advanced merger galaxy IRAS 17208–0014.

The high resolution continuum images reveal the details of the previously undetected

nuclear starburst region of this galaxy. Both diffuse and compact continuum emission are detected. The total VLBI flux is 52 mJy, and represents only half of the total flux seen with the VLA at a lower resolution, suggesting the existence of diffuse emission not detected by our VLBI array. The compact sources in the starburst region are more likely clustered luminous RSNs and SNRs, considering the H II spectra observed in this galaxy and its morphological similarities to other well-known starbursts. However, we cannot rule out the possibility that each of our compact sources is mainly powered by an individual bright RSN nested in a region that contains faded SNRs. The brightness temperatures of the compact structures seen in these observations are more than 10^5 K. The flux density of the brightest source in the starburst region is less than 3% of the total radio flux density. The results suggest that there is no radio-loud AGN in the nuclear region of IRAS 17208–0014.

Both the far-IR luminosity and the radio continuum flux of this galaxy imply a massive SFR of $\sim 84 M_{\odot} \text{ yr}^{-1}$ and supernova rate of $\sim 4 \text{ yr}^{-1}$. The estimated individual luminous RSN number agrees surprisingly well with the number of the compact sources detected above 5σ level. From the minimum energy condition, we have estimated the pressure to be $\sim 6 \times 10^{-10} \text{ dyn cm}^{-2}$ and the magnetic field to be $\sim 144 \mu\text{G}$ in the starburst region.

The very wide H I absorption is composed of five components with velocity widths between 58 and 232 km s^{-1} . The column densities of these absorption peaks are on the order of $10^{20} T_s$, and the derived visual extinctions are between $0.066 T_s$ and $0.174 T_s$ mag. The strongest velocity gradient in the H I absorption is seen in position angle 120° , as in the CO (1 – 0) emission. The H I PV profile in this position angle shows a velocity gradient of $1653 \text{ km s}^{-1} \text{ kpc}^{-1}$. The calculated dynamical mass, assuming Keplerian motion, is $2.3 \times 10^9 (\sin^{-2} i) M_{\odot}$, comparable to the enclosed mass obtained from CO observations. The H I absorption results suggest the existence of a neutral gas disk containing several clouds, situated inside a larger scale molecular disk as seen in the interferometric CO (1 – 0) emission-line observations.

Table 3.1: Parameters of the VLBI Observations of IRAS 17208–0014

Parameter	Value
Frequency	1362 MHz
Observing Date	2001 June 4
Observing Array	VLBA + Y27
Total observing time	11 hr
R.A. (J2000)	17 ^h 23 ^m 21 ^s .9554
Dec. (J2000)	−00°17′00″.938
Phase-referencing cycle time	2 min
Bandwidth	16 MHz
Continuum image rms	70 μ Jy beam ^{−1}
Line velocity resolution	58 km s ^{−1}
Line image rms	0.5 mJy beam ^{−1}
Optical depth image cutoff	3 mJy beam ^{−1}
Angular to linear scale ^a	1 mas = 0.76 pc

NOTES: (a) Assumes distance of 171 Mpc, and $H_0 = 75 \text{ km s}^{-1} \text{ Mpc}^{-1}$.

Table 3.2: Compact Sources in IRAS 17208–0014

Gaussian Component Parameters						
Source (1)	Relative Position ^a (mas) (2)	Peak ^b ($\mu\text{Jy beam}^{-1}$) (3)	Total (mJy) (4)	Major Axis ^c (pc) (5)	Minor Axis ^c (pc) (6)	P.A. (deg) (7)
1	0, 0	1043.3 ± 1.0	2.764 ± 0.003	52.3 ± 0.4	34.9 ± 0.3	155
2	87E, 40N	791.1 ± 0.9	2.356 ± 0.003	50.7 ± 0.5	40.5 ± 0.4	78
3	153W, 6S	759.6 ± 1.3	2.316 ± 0.004	54.9 ± 1.3	38.3 ± 1.0	107
4	182E, 31S	737.5 ± 0.7	1.438 ± 0.001	38.5 ± 0.2	34.9 ± 0.2	122
5	98W, 86N	731.0 ± 1.0	2.269 ± 0.003	53.7 ± 1.3	39.8 ± 1.0	26
6	50W, 6S	718.7 ± 1.3	1.489 ± 0.003	45.2 ± 0.7	31.6 ± 0.2	171
7	6W, 109S	700.7 ± 2.0	2.834 ± 0.001	78.3 ± 2.0	35.6 ± 0.9	26

NOTES: (a) The reference position (0,0) is $\alpha(\text{J2000}) = 17^{\text{h}}23^{\text{m}}21^{\text{s}}9554$, $\delta(\text{J2000}) = -00^{\circ}17'00''938$.

(b) Higher than $9\sigma = 630\mu\text{Jy beam}^{-1}$.

(c) At half maximum.

Table 3.3: Parameters of the H I Clouds in IRAS 17208–0014

Velocity ^a	Δv_{FWHM}	τ_{peak}	$N_{\text{HI}}/T_{\text{s}}$	N_{HI} ^b	$A_{\text{v}}/T_{\text{s}}$ ^c	A_{v} ^b
(km s ^{−1})	(km s ^{−1})		(cm ^{−2} K ^{−1})	(cm ^{−2})	(mag K ^{−1})	(mag)
(1)	(2)	(3)	(4)	(5)	(6)	(7)
12653.5	174	0.3	10.1×10^{19}	10.1×10^{21}	0.066	6.6
12825.7	58	2.5	28.0×10^{19}	28.0×10^{21}	0.174	17.4
12883.1	232	0.3	13.5×10^{19}	13.5×10^{21}	0.085	8.5
12940.4	58	1.3	14.4×10^{19}	14.6×10^{21}	0.094	9.4
12997.8	174	0.5	16.8×10^{19}	16.8×10^{21}	0.111	11.1

NOTES: (a) Heliocentric velocity of the H I absorption feature at τ_{peak} .

(b) Based on $T_{\text{s}} = 100$ K.

(c) Assumes a Galactic dust-to-gas ratio.

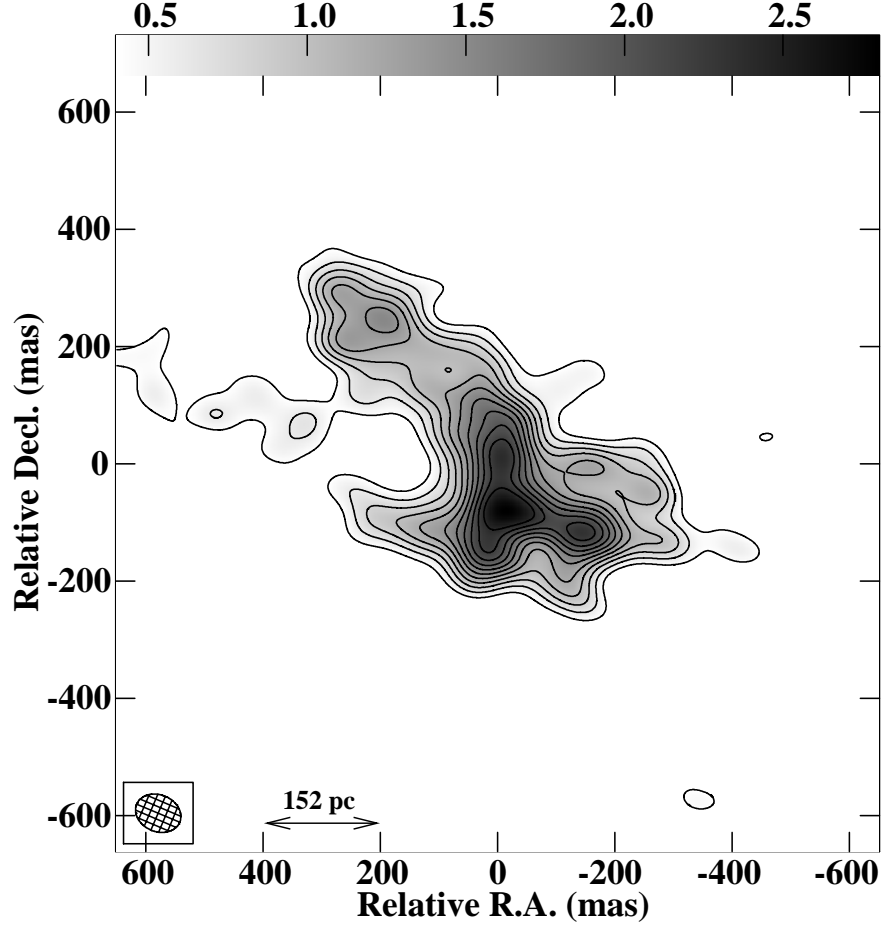


Figure 3.1: Low resolution continuum image of the central region in IRAS 17208–0014 at 1362 MHz. The restoring beam size is 80×63 mas in position angle 67° . The peak flux is $2.8 \text{ mJy beam}^{-1}$, and the contour levels are at $-4, 4, 8, \dots, 24$ times the rms noise level, which is $0.1 \text{ mJy beam}^{-1}$. The gray scale range is indicated by the wedge at the top of the image in units of mJy beam^{-1} . The reference position (0,0) is $\alpha(\text{J2000}) = 17^{\text{h}}23^{\text{m}}21^{\text{s}}.9648$, $\delta(\text{J2000}) = -00^\circ17'00''.819$. A two dimensional Gaussian taper falling to 30% at $2 \text{ M}\lambda$ was applied.

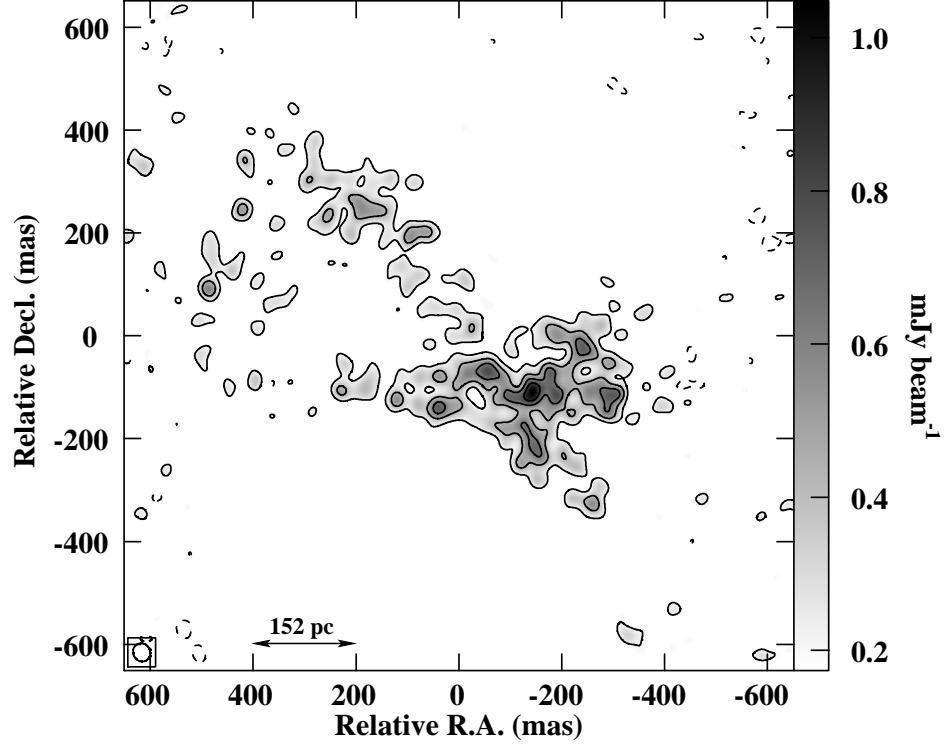


Figure 3.2: High resolution continuum image of the central region in IRAS 17208–0014 at 1362 MHz. The restoring beam size is 36×33 mas in position angle 25° . The peak flux is $1043 \mu\text{Jy beam}^{-1}$, and the contour levels are at -3 , 3 , 6 , 9 , and 12 times the rms noise level, which is $70 \mu\text{Jy beam}^{-1}$. The gray scale range is indicated by the wedge at the right side of the image. The reference position $(0,0)$ is $\alpha(\text{J2000}) = 17^{\text{h}}23^{\text{m}}21^{\text{s}}.9648$, $\delta(\text{J2000}) = -00^\circ17'00''.819$. A Gaussian taper falling to 30% at $6 \text{ M}\lambda$ in the u direction and $4.5 \text{ M}\lambda$ in the v direction was applied.

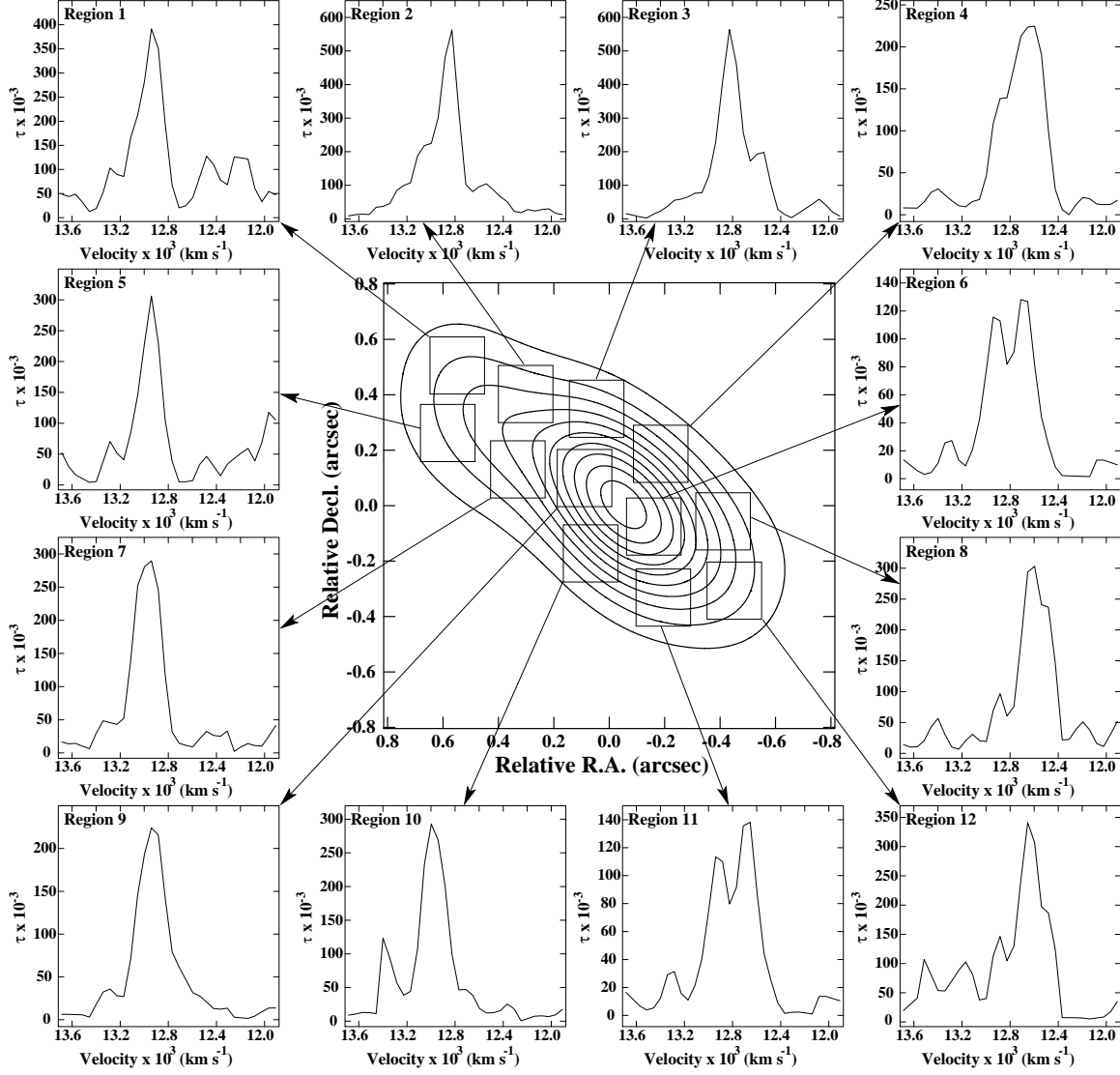


Figure 3.3: Hanning smoothed H I optical depth spectra obtained at various locations against the background continuum source IRAS 17208-0014 at 1362 MHz. All the spectra are scaled to the maximum H I absorption optical depth of each region. The restoring beam size is $0''.55 \times 0''.35$ in position angle 34° . The contour levels of the continuum image are at 3, 6, ... 30 mJy beam^{-1} , and the peak flux is 32 mJy beam^{-1} . The reference position (0,0) is $\alpha(\text{J2000}) = 17^{\text{h}}23^{\text{m}}21^{\text{s}}9648$, $\delta(\text{J2000}) = -00^\circ17'00''.819$.

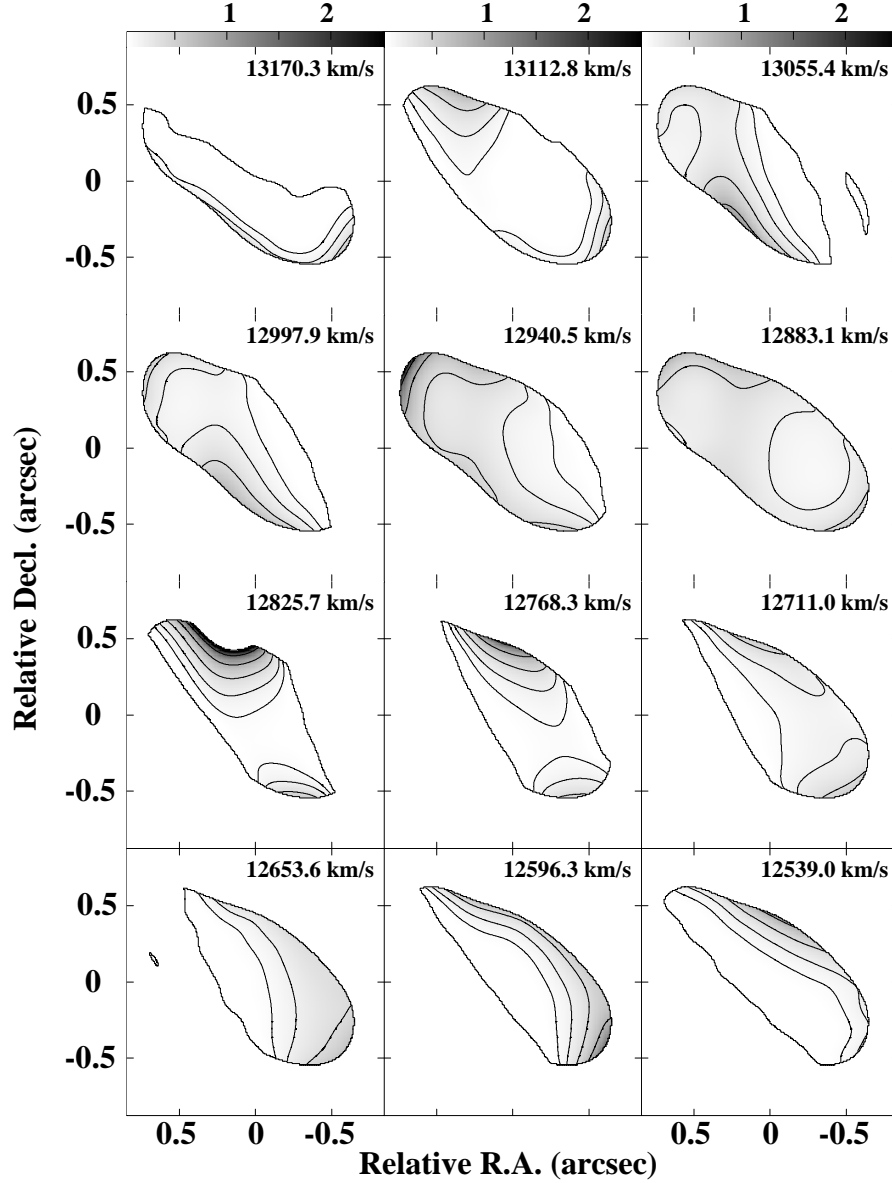


Figure 3.4: Gray-scale and contour HI optical depth channel images toward IRAS 17208–0014 in the velocity range 13,170.3–12,539.0 km s^{−1}. The restoring beam in these images is 0″55 × 0″35 in position angle 34°. The velocity resolution is 58 km s^{−1}. The gray-scale range is indicated by the step wedge at the top of the images; the contour levels are 0.1, 0.2, 0.4, 0.8, and 1.6.

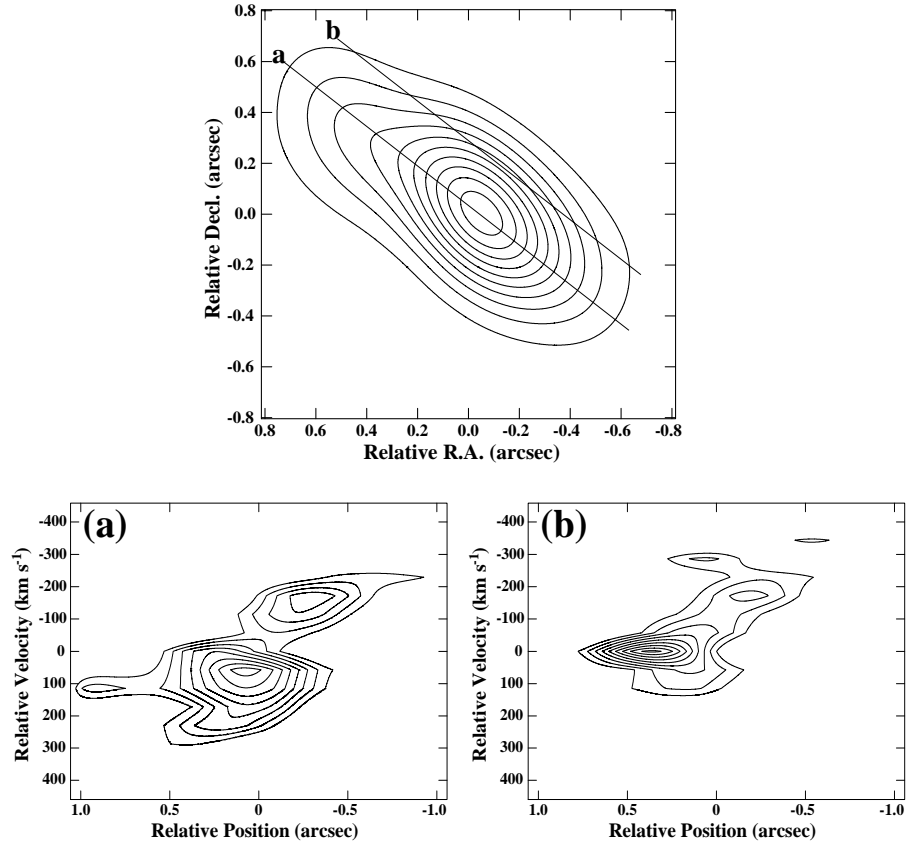


Figure 3.5: Position-velocity plots of the HI 21 cm absorption along two cuts in position angle 52° . The contour levels are at $-2, -2.5, \dots -6$ mJy beam $^{-1}$. The velocity resolution is 58 km s $^{-1}$. The zero point on the velocity scale corresponds to a heliocentric velocity (cz) of $12,825.7$ km s $^{-1}$. The contour levels of the continuum image shown at the top are at $3, 6, \dots 30$ mJy beam $^{-1}$, and the peak flux is 32 mJy beam $^{-1}$. The reference position $(0,0)$ is $\alpha(\text{J2000}) = 17^{\text{h}}23^{\text{m}}21^{\text{s}}.9648$, $\delta(\text{J2000}) = -00^\circ17'00''.819$. The restoring beam size is $0''.55 \times 0''.35$ in position angle 34° .

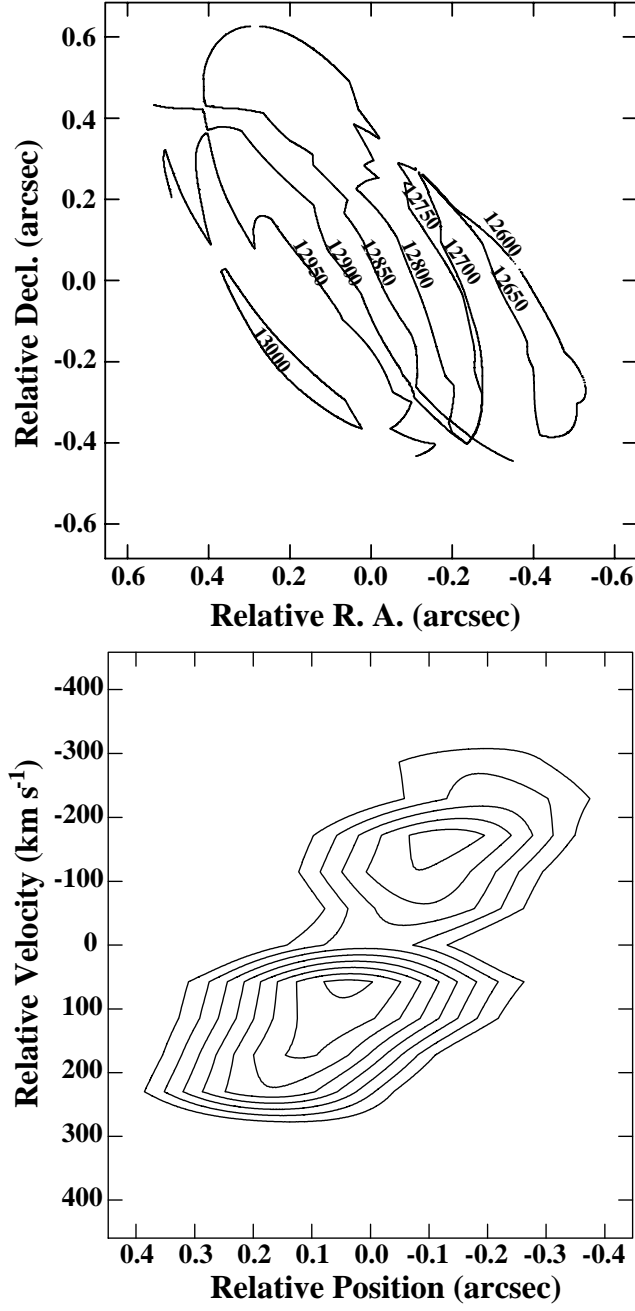


Figure 3.6: H I velocity field and H I position-velocity plot (P.A. 120°) *Top*: Velocity contours of the H I 21 cm absorption in steps of 50 km s⁻¹. The reference position (0,0) is $\alpha(\text{J2000}) = 17^{\text{h}}23^{\text{m}}21^{\text{s}}.9648$, $\delta(\text{J2000}) = -00^{\circ}17'00''.819$. *Bottom*: H I position-velocity plot in position angle 120°. The contour levels are at $-1.5, -2, \dots, -6$ mJy beam⁻¹. The zero point on the velocity scale corresponds to a heliocentric velocity (cz) of 12,825.7 km s⁻¹.

Chapter 4

Sensitive VLBI Continuum and H I Absorption Observations of NGC 7674: First Scientific Observations with the Combined Array VLBA, VLA & Arecibo¹

4.1 INTRODUCTION

At bolometric luminosities above $10^{11} L_{\odot}$, infrared galaxies become the most numerous objects in the local universe ($z \leq 0.3$). These galaxies further subdivide into luminous (LIRGs²), ultraluminous (ULIRGs³), and hyperluminous (HyLIRGs⁴) infrared galaxies (Sanders & Mirabel 1996). A large fraction of these IR galaxies are interacting or merger systems, and this fraction seems to increase with luminosity (Sanders et al. 1988). The bulk of the energy radiated by these sources is infrared emission from warm dust grains heated by a central power source or sources. The critical question concerning these galaxies is whether the dust is heated by a nuclear starburst, or an active galactic nucleus (AGN), or a combination of both. Mid-infrared spectroscopic studies on a sample of ULIRGs by Genzel et al. (1998), suggest that 70%–80% of these galaxies are predominantly powered by recently formed massive stars, and 20%–30% by a central AGN. These authors conclude

¹Results presented in Chapter 4 have been accepted for publication in The Astrophysical Journal (E. Momjian, J. D. Romney, C. L. Carilli & T. H. Troland).

²LIRG: $10^{11} L_{\odot} \leq L_{\text{IR}}(8 - 1000 \mu\text{m}) < 10^{12} L_{\odot}$

³ULIRG: $10^{12} L_{\odot} \leq L_{\text{IR}}(8 - 1000 \mu\text{m}) < 10^{13} L_{\odot}$

⁴HyLIRG: $L_{\text{IR}}(8 - 1000 \mu\text{m}) \geq 10^{13} L_{\odot}$

further that at least half of these ULIRGs are probably powered by both an AGN and a starburst in a 1–2 kpc diameter circumnuclear disk or ring.

In this chapter, we present VLBI continuum and H I absorption observations on the type-2 Seyfert galaxy NGC 7674 (Mrk 533, Arp 182, UGC 12608). This galaxy is a nearby LIRG with an infrared luminosity of $L_{\text{IR}} = 3.1 \times 10^{11} L_{\odot}$ (González Delgado, Heckman, & Leitherer 2001). Optical observations of NGC 7674 show a nearly face-on spiral with an inclination angle of $i = 31^{\circ}$ (Verdes-Montenegro et al. 1997). This galaxy is classified as Sbc pec (de Vaucouleurs, de Vaucouleurs, & Corwin 1976). It is the brightest member of the well isolated Hickson 96 compact galaxy group (Hickson 1982), which consists of four interacting galaxies with a mean heliocentric velocity of 8760 km s^{-1} and a low velocity dispersion ($\sigma_v = 160 \text{ km s}^{-1}$) (Verdes-Montenegro et al. 1997). The two largest members in this group, NGC 7674 (H96a) and NGC 7675 (H96b), are separated by a projected distance of 2.2 arcmin. The observed features in NGC 7674, as revealed in optical images, can be accounted for by tidal interactions with its companion galaxies in the group (Verdes-Montenegro et al. (1997).

The Very Large Array 15 GHz observations of NGC 7674 by Unger et al. (1988) showed a triple radio source with components defined as eastern, central, and western, but their 1666 MHz EVN+MERLIN observations at 20 mas resolution only revealed the central and the western components. These authors identified the central component as the radio nucleus and the western component as a radio lobe moving outward through the interstellar medium. However, their 20 mas VLBI image did not reveal any clear jet structure connecting the central and the western components, which are separated by ~ 0.5 arcsec. MERLIN observations by Beswick, Pedlar, & McDonald (2002) at $0''.27 \times 0''.15$ and 1.4 GHz also revealed a triple radio source consistent with the 15 GHz VLA observations (Unger et al. 1988).

Single dish Arecibo observations by Mirabel (1982) at 3.3 arcmin resolution showed two clearly separated H I absorption features that are blueshifted with respect to a wider emission line. The absorption lines have full velocity widths at 20% of 63 and 45 km s^{-1} , while the emission line has 344 km s^{-1} . The two H I absorption features are at $\sim 8600 \text{ km s}^{-1}$ and $\sim 8546 \text{ km s}^{-1}$, respectively. However, the neutral hydrogen interferometric observations

with MERLIN at $0''.27 \times 0''.15$ and 32 km s^{-1} (Beswick, Pedlar, & McDonald 2002) revealed a single H I absorption feature against the central component with an optical depth of 0.21 and a velocity width of 114 km s^{-1} at half maximum, centered at 8623 km s^{-1} . No H I absorption was reported toward the eastern or the western components in these MERLIN observations.

We adopt a distance of 115.6 Mpc to NGC 7674, assuming $H_0 = 75 \text{ km s}^{-1} \text{ Mpc}^{-1}$. At this distance 1 mas corresponds to 0.53 pc.

4.2 OBSERVATIONS AND DATA REDUCTION

The observations were carried out at 1380 MHz on September 15, 2001 using NRAO's⁵ Very long Baseline Array (VLBA) and the phased Very Large Array (VLA), and NAIC's 305-m Arecibo radio telescope⁶. These observations constitute the first scientific use of the Arecibo radio telescope with the VLBA after the installation and the successful testing of the VLBA4 recording system. Two adjacent 8 MHz baseband channel pairs were used in these observations, both with right and left-hand circular polarizations, sampled at two bits. The first baseband channel pair was centered close to the frequency of the neutral hydrogen 21 cm line, which is at a heliocentric redshift of $z = 0.0287$, or $cz = 8600 \text{ km s}^{-1}$. The velocity coverage of each baseband channel was $\sim 1738 \text{ km s}^{-1}$. The data were correlated at the VLBA correlator in Socorro, NM with 512-point spectral resolution per baseband channel, and 5.1 seconds correlator integration time. The total observing time was 12 hours, with the 305-m Arecibo radio telescope participating for 140 minutes. Table 4.1 summarizes the parameters of these observations.

The inclusion of both the phased VLA (Y27) and Arecibo were essential in these observations in two respects. One is the overall image sensitivity (the rms thermal noise level), and the other is the short to moderate-length sensitive baselines necessary to image large scale structures. While including the phased VLA in the VLBA improves the image

⁵The National Radio Astronomy Observatory is a facility of the National Science Foundation operated under cooperative agreement by Associated Universities, Inc.

⁶The Arecibo Observatory is part of the National Astronomy and Ionosphere Center, which is operated by Cornell University under a cooperative agreement with the National Science Foundation.

sensitivity by a factor of ~ 2.4 , the sensitivity improves by a factor of ~ 7.1 when both the phased VLA and Arecibo are added to the VLBA. This latter sensitivity improvement is achieved only during the time when Arecibo is observing. In our observations, where Arecibo participated for about 20% of the total observing time, the image sensitivity was ~ 4.2 times better than the VLBA alone for the whole observing time. Also, the 305-m Arecibo radio telescope provided the 3rd sensitive short baseline in our observations, this baseline is Arecibo–Saint Croix with 238 km length. The other two sensitive short baselines are the Y27–Pie Town (52 km) and Y27–Los Alamos (226 km). Short sensitive baselines are critical to image extended continuum structures as well as the HI absorption toward these structures.

Data reduction and analysis were performed using the Astronomical Image Processing System (AIPS) and the Astronomical Information Processing System (AIPS++).

Along with the target source NGC 7674, the compact source J2329+0834 was observed as a phase reference with a cycle time of 150 seconds, 100 seconds on the target source and 50 seconds on the phase calibrator. The source J2334+0736 was used for amplitude calibration, and 3C 454.3 (J2253+1608) was observed as a fringe finder and used to determine the initial fringe delays and to calibrate the bandpass.

After applying *a priori* flagging and manually excising integrations affected by interference, ionospheric corrections were applied using the AIPS task “TECOR”. Amplitude calibration was performed using measurements of the antenna gain and the system temperature of each station. The delay solutions for 3C 454.3 were applied and a bandpass calibration was performed. To image the continuum of the target source, its line-free channels were averaged to a single spectral channel with a total width of 14 MHz. The phase calibrator J2329+0834 was self-calibrated in both amplitude and phase and imaged in an iterative cycle. The self-calibration solutions of J2329+0834 were applied on the continuum data of the target source NGC 7674. Due to the high rms noise values obtained after applying the self-calibration solutions of the phase reference source to NGC 7674, self calibration was performed on the continuum data set of the target source itself. This resulted in a significant improvement in the signal-to-noise ratio. The self calibration solutions of both the phase calibrator and the target source were later applied to the line data, in which every

two channels were averaged to increase the sensitivity. The resulting channel separation of the H I data cube was 31.25 kHz (6.986 km s⁻¹). The continuum emission was subtracted from the spectral-line visibility data using the AIPS task “UVLSF”. The spectral-line data were then analyzed at various spatial and spectral resolutions. Deconvolution of the images in the continuum and line data sets was performed using the Clark “CLEAN” algorithm as implemented in the AIPS task “IMAGR”. Optical-depth $\tau(\nu)$ cubes were calculated from the H I absorption image cubes and continuum images with a similar resolution as

$$\tau(\nu) = -\ln[1 - I_{\text{line}}(\nu)/I_{\text{continuum}}]. \quad (4.1)$$

Along with these observations, archival VLA data of NGC 7674 from 1986 have been reduced and analyzed. These A-array observations with program ID AH 233 were carried out at 15 GHz.

4.3 RESULTS AND ANALYSIS

4.3.1 The Radio Continuum

Figure 4.1 shows moderate and high resolution continuum images of the nuclear region in NGC 7674 at 1380 MHz. The top image has a resolution of 20 mas (10.6 pc) obtained with natural grid weighting (ROBUST = 5 in AIPS task “IMAGR”). The resolution of this image is comparable to the VLBI image of Unger et al. (1988). We distinguish six structures in this image, only three of them previously known. We identify these three structures, following Unger et al. (1988), as western (W), central (C) and eastern (E) components. In our image, C is the brightest, E is the diffuse emission region just to the east of C, and W is the second brightest peak. In addition to these components, we detect a clear collimated jet structure (J) connecting the C and W components, and two diffuse emission regions, one located to the north-east of E that we designate the northeastern component (NE), and another to the south-west of W, the southwestern component (SW). The linear extent of the whole nuclear region in the plane of the sky is ~ 1.4 arcsec (742 pc), and the total flux is ~ 138 mJy. We also reduced the VLA data from these 1.38 GHz observations, which

were performed in the DnC configuration and yielded a resolution of $40''.5 \times 17''.3$ (PA 80°). The total flux density of the source at this resolution is ~ 230 mJy. Our analysis of the 15 GHz archival VLA data resulted in a marginal detection (3σ) of the newly discovered components NE and SW.

The bottom images in Figure 4.1 are of C (*left*) and W (*right*) at the full resolution of our array, which is 11×5 mas (5.8×2.7 pc). These two images were obtained with grid weighting ROBUST = -1 . The other components identified in our 20 mas image are resolved.

Figure 4.2 shows the continuum structure in gray scale with half-maximum ellipses for gaussians fitted to the structures seen in C (*left*) and W (*right*). These gaussian components provide a convenient measure of source structure even if they do not necessarily represent discrete physical structures. Parameters of the gaussian fits are listed in Tables 4.2 and 4.3, for components C and W, respectively. Column 1 in both these tables lists the gaussians seen in Figure 4.2, and column 2 their positions relative to the brightest peak in each image. Columns 3 and 4 show the peak and the total flux densities of the fitted gaussian functions, respectively. Columns 5, 6, and 7 list the half-power ellipse axes and the position angles. Column 8 shows the derived brightness temperatures of these components. All Gaussian fitting parameters were obtained using the tool “IMAGEFITTER” in AIPS++.

An image of the nuclear region of NGC 7674 at lower resolution (Figure 4.3) clearly shows the diffuse components seen at 20 mas (Figure 4.1-top). The restoring beam in Figure 4.3 is 92×76 mas (48.8×40.3 pc). Table 4.4 summarizes the characteristics of the continuum structures labeled in Figure 4.3. The positions (col. [2]) are relative to the central component (C). Columns 3 and 4 show the peak and the total flux densities of the fitted gaussian functions, respectively. Columns 5, 6, and 7 list the half-power ellipse axes and the position angles. No good gaussian fit was obtainable for the jet structure; thus its flux density and its size were estimated from the residual image left after subtracting the gaussian fittings of the other components. The reported size of the jet component is its linear extent on the plane of the sky.

The accuracy of the phase calibrator position is important in phase-referencing observations (Walker 1999), which allow the determination of the absolute position of the target

source and its components, if any, from the position of the calibrator. The positions reported in all the above mentioned images and tables are obtained from the position of the phase-reference source J2329+0834. The position of J2329+0834 is from the VLBA calibrator survey (Beasley et al. 2002), with positional accuracy of ~ 0.7 mas in right ascension and ~ 1.3 mas in declination.

Table 4.5 summarizes the magnetic field and pressure values of the radio continuum components seen in NGC 7674 at low angular resolution using the minimum energy condition (Miley 1980). These properties were derived using the 1380 MHz total flux densities of these components (Table 4.4) and their angular extents on the plane of the sky, and assuming a path length through the source on the line of sight equal to the major axis of the component. Spectral indices of the C, E, and W components were obtained from Beswick, Pedlar, & McDonald (2002). For the NE and SW components, we derived spectral indices from the marginal detection of these structures at 15 GHz with the VLA and our 1380 MHz VLBI results convolved to the beam size of the 15 GHz observations. Spectral indices of all five components are steep (> 0.6 ; $S \propto \nu^{-\alpha}$). No spectral index estimate was possible for the jet (J) structure, hence it was excluded from these calculations.

4.3.2 The H I Absorption

All images reported in this section are reconstructed with natural grid weighting in the AIPS task “IMAGR”. The H I data cube was imaged using Hanning smoothing to improve the signal-to-noise ratio. Thus, although the channel separation is about 7 km s^{-1} , the effective velocity resolution is $\sim 14 \text{ km s}^{-1}$. The H I results are described separately for high and low spatial resolutions, because of the distinctive characteristics of the absorption at these two scales.

4.3.2.1 H I Absorption at High Spatial Resolution

Figure 4.4 shows the naturally weighted high resolution continuum images of the central (*top*) and the western (*bottom*) components in NGC 7674 with averaged H I absorption spectra against several background continuum regions in both C and W. The angular resolution

is 17×5 mas (9×2.7 pc). The rms noise in the continuum images is $\sim 30 \mu\text{Jy beam}^{-1}$. While the spectra obtained toward W show no H I absorption, all the spectra obtained against the components in C show significant absorption. The rms noise in the H I image cube is $\sigma \simeq 260 \mu\text{Jy beam}^{-1}$.

Figure 4.5 shows optical depth $\tau(\nu)$ images in the velocity range 8626.7–8529.0 km s^{−1}. These images explicitly show the variation of the H I opacity against the central component of NGC 7674 at high spatial resolution. The images are obtained by blanking areas where the flux density of the continuum image is below 2.5 mJy beam^{−1} (i.e. less than 15% of the peak flux), or the H I absorption is below 1.04 mJy beam^{−1} (i.e. 4σ).

Four main absorption features are distinguished in both the spectra H I and the optical depth images. They are identified in Figure 4.4. Their velocity widths range between 18 and 98 km s^{−1} at half maximum, with optical depths between 0.164 and 0.412. Table 4.6 summarizes the physical characteristics of these four H I absorption features, obtained by fitting gaussian functions to the optical depth spectra averaged over regions where the absorption features are seen. The fits were performed using the tool “IMAGEPROFILEFITTER” in AIPS++. The velocities (col. [2]) refer to the center velocities of these features. The widths of these lines (col. [3]) are the full widths at half peak optical depth. Column 4 is the peak optical depth value of each feature. N_{HI}/T_s of each peak (col. [5]) is calculated as

$$N_{\text{HI}}/T_s \text{ (cm}^{-2} \text{ K}^{-1}\text{)} = 1.823 \times 10^{18} \int \tau(v) dv, \quad (4.2)$$

with

$$\int \tau(v) dv = 1.06 \tau_{\text{peak}} \Delta v_{\text{FWHM}} \quad (4.3)$$

for gaussian profiles. The column densities N_{HI} (col. [6]) are derived assuming a spin temperature T_s of 100 K.

The first two H I absorption components listed in Table 4.6 are mainly seen against the continuum component C1. The weaker of these two is wider, 98.3 km s^{−1}. The other two features are narrower, and are seen against the continuum component C3. Only the strongest H I absorption feature, the first component in Table 4.7, has a measurable velocity gradient as shown in the velocity field image with continuum contours superimposed

(Figure 4.6-*top*). Figure 4.6-*bottom* shows a position velocity (P-V) diagram along a cut in position angle 14° . This diagram suggests a velocity gradient of $\sim 30.3 \text{ km s}^{-1}$ along $\sim 18.4 \text{ pc}$ (i.e. $\sim 1647 \text{ km s}^{-1} \text{ kpc}^{-1}$).

Figures 4.7*a*-4.7*b* are N_{HI}/T_s images in the velocity range $8626.7\text{--}8529.0 \text{ km s}^{-1}$. Figure 4.7*a* is a color-scale image and contours of N_{HI}/T_s . Figure 4.7*b* shows the same N_{HI}/T_s color-scale image with continuum contours superimposed for positional reference.

4.3.2.2 H I Absorption at Low Spatial Resolution

Figure 4.8 shows the naturally weighted low resolution continuum image of the nuclear region in NGC 7674 at 1380 MHz and $129 \times 108 \text{ mas}$ ($68.4 \times 57.2 \text{ pc}$) resolution. Averaged H I absorption spectra are shown against the previously identified continuum components. The rms noise level of the continuum and the H I data are 85 and $570 \mu\text{Jy beam}^{-1}$, respectively. We notice clear H I absorption detections (greater than $3\sigma = 1.68 \text{ mJy beam}^{-1}$) toward C, E, and NE. No absorption is detected against SW, W, or J. The strongest H I feature is centered at 8600.3 ± 1.1 . This value is consistent with the strongest feature seen in the Arecibo single dish spectrum at $3''.3$ resolution (Mirabel 1982); however, it is lower by 23 km s^{-1} from the value reported by Beswick, Pedlar, & McDonald (2002) at $0''.27 \times 0''.15$ resolution with MERLIN. The non-detection of H I absorption in the MERLIN observations toward E (Beswick, Pedlar, & McDonald 2002) could be simply a result of their low velocity resolution, which is 32 km s^{-1} , compared to 14 km s^{-1} achieved in our sensitive VLBI observations.

Figure 4.9 shows optical depth $\tau(\nu)$ images in the velocity range $8619.6\text{--}8522.0 \text{ km s}^{-1}$. These images explicitly show the variation of the H I opacity against C, E, and NE at low spatial resolution. The images are obtained by blanking areas where the flux density of the continuum image is below 6 mJy beam^{-1} (i.e. less than 12% of the peak flux), or the H I absorption is below $2.28 \text{ mJy beam}^{-1}$ (i.e. 4σ).

Figures 4.10*a*-4.10*b* are N_{HI}/T_s images in the velocity range $8626.7\text{--}8522.0 \text{ km s}^{-1}$. Figure 4.10*a* is a color-scale image and contours of N_{HI}/T_s . Figure 4.10*b* shows the same N_{HI}/T_s color-scale image with continuum contours superimposed for positional reference.

The top panel of Figure 4.11 is the velocity field of the H I absorption at low spatial

resolution superimposed on the continuum contours, and the bottom panel is the averaged H I absorption spectrum over the region where absorption signals are detected.

From the H I absorption images and spectra at low resolution (Figures 4.8, 4.9, 4.10, & 4.11-*top*), we distinguish four main absorption features. They are identified in Figure 4.8. Their velocity widths range between 23 and 165 km s⁻¹ at half maximum, with optical depths between 0.1 and 0.65. Table 4.7 summarizes the physical characteristics of these four H I absorption features, obtained by fitting gaussian functions to the optical depth spectra averaged over regions where the absorption features are seen. The fittings were performed using the tool “IMAGEPROFILEFITTER” in AIPS++. The velocities (col. [2]) refer to peaks of these features. The widths of these lines (col. [3]) are the full widths at half peak optical depth. Column 4 is the peak optical depth value of each feature as seen in the averaged spectra. N_{HI}/T_s of each peak (col. [5]) is calculated using equations 4.2 and 4.3. The column densities N_{HI} (col. [6]) are derived assuming $T_s = 100$ K.

At this low resolution, the absorption feature with the highest velocity is seen toward C. The velocity of the H I line seen against E is lower than the velocities of the H I features seen against C and NE.

The bottom panel of Figure 4.11 is the integrated H I absorption profile against the whole region where H I signals are detected at 129×108 mas resolution. While the high velocity feature is mainly due to the H I absorption toward C, the lower velocity feature arises from the H I absorption toward both E and NE. The double peak pattern seen in our spectrum is very consistent with the observed H I absorption profile with Arecibo at 3'3 resolution (Mirabel 1982) in both velocity and width values. It should be noted that the MERLIN observations of Beswick, Pedlar, & McDonald (2002) did not detect the lower velocity component seen in this spectrum.

4.4 DISCUSSION

4.4.1 The Radio Continuum

At moderate resolution (tens of mas), the nuclear region of NGC 7674 is composed of several continuum structures extending over 0.75 kpc (Figure 4.1-*top*, & Figure 4.3). At high resolution, the continuum results (Figure 4.1-*bottom*, & Figure 4.2) show several compact continuum structures in both the central (C) and the western (W) components, with brightness temperatures $\geq 10^7$ K. The total flux density of all the radio components seen in our VLBI array is ~ 138 mJy and represents only 60% of the total flux density seen at lower resolution with the VLA, and 72% of the total flux density detected with MERLIN (Beswick, Pedlar, & McDonald 2002). These differences suggest the existence of diffuse emission not detected by our VLBI array, which may be extensions to the continuum structures seen in our observations. In the next two sections, we will discuss the possible nature of all the continuum structures seen in this galaxy.

4.4.1.1 Is there a starburst in NGC 7674?

Most characteristics of the continuum structures in NGC 7674, both at large and small scales, seem to be related to AGN activity and not to a nuclear or circumnuclear starburst. Calculations by Yun, Reddy, & Condon (2001) clearly indicate that this galaxy does not obey the radio-FIR correlation well known for “normal” galaxies, where the main energy source is not due to a supermassive black hole (Condon 1992). This correlation is represented by the quantity q as defined by Helou, Soifer, & Rowan-Robinson (1985):

$$q = \log \{ [FIR / (3.75 \times 10^{12})] / S_{1.4 \text{ GHz}} \}, \quad (4.4)$$

where FIR is given by:

$$FIR = 1.26 \times 10^{-14} (2.58 S_{60 \text{ } \mu\text{m}} + S_{100 \text{ } \mu\text{m}}). \quad (4.5)$$

For “normal galaxies”, $q = 2.34 \pm 0.01$ (Yun, Reddy, & Condon 2001). Furthermore, these authors conclude that a value of $q \leq 1.64$ indicates the presence of an AGN. For NGC 7674, they report $q = 1.53$.

Nonetheless, evidence does exist for star formation. The optical spectroscopic studies of González Delgado, Heckman, & Leitherer (2001) indicate the presence of young/intermediate age (a few Myr to a few 100 Myr) stars in the nuclear region of NGC 7674, and the question we seek to answer at this stage is whether any of the emission structures we observe in the nuclear region of NGC 7674 could be related to starburst activity. For this purpose, we compare the expected star formation rates from $H\alpha$ and IR emissions with the nonthermal radio continuum emission. The star formation rates will be calculated using a Salpeter IMF which has the form $\psi(M) \propto M^{-2.35}$ (Salpeter 1955) with mass limits 0.1 and 100 M_\odot as given by Kennicutt (1998), taking into account that the nonthermal radio emission would result from Type II supernova explosions that require stars with masses $\geq 8 M_\odot$.

The optical spectroscopic observations of de Grijp et al. (1992) suggest that the $H\alpha$ luminosity of the nuclear region of NGC 7674 is 5.3×10^{34} W. Assuming all the $H\alpha$ emission is due to starburst activity and using the relationship between the star formation rate (SFR) and the $H\alpha$ luminosity (Kennicutt 1998), which has the form:

$$SFR (M_\odot \text{ yr}^{-1}) = 7.9 \times 10^{-35} L_{H\alpha} \text{ (W)}, \quad (4.6)$$

we derive an SFR of $4.2 M_\odot \text{ yr}^{-1}$.

To calculate the SFR from the IR emission, we assume all the IR luminosity is only due to starburst, and use the relationship given by Kennicutt (1998):

$$SFR (M_\odot \text{ yr}^{-1}) = 4.5 \times 10^{-44} L_{\text{IR}} \text{ (erg s)}^{-1}. \quad (4.7)$$

The IR luminosity of NGC 7674 is $3.1 \times 10^{11} L_\odot$ (González Delgado, Heckman, & Leitherer 2001), and the resulting SFR is $54 M_\odot \text{ yr}^{-1}$.

The SFR calculations based on radio luminosity will take into account the flux densities of the three diffuse radio components, namely E, NE and SW. The radio luminosity of these three components is $8.6 \times 10^{22} \text{ W Hz}^{-1}$, and it is all due to nonthermal radiation because of the mere fact that they are detected by our VLBI array. VLBI arrays, even with the extremes of sensitivity we were able to achieve in these observations, currently lack the sensitivity to detect thermal emission. To derive the SFR from the radio luminosity, we first calculate the supernova rate using the empirical relation of Condon & Yin (1990) that

relates the observed Galactic non-thermal luminosity (L_{NT}) to the supernova rate ν_{SN} :

$$\left(\frac{L_{\text{NT}}}{10^{22} \text{ W Hz}^{-1}}\right) = 13 \left(\frac{\nu}{\text{GHz}}\right)^{-0.8} \left(\frac{\nu_{\text{SN}}}{\text{yr}^{-1}}\right). \quad (4.8)$$

We derive $\nu_{\text{SN}}=0.86 \text{ yr}^{-1}$. The SFR can be calculated from the supernova rate by using and combining the following expressions:

$$\nu_{\text{SN}} = \int_{m_{\text{sn}}}^{100M_{\odot}} \psi(m) dm, \quad (4.9)$$

with $m_{\text{sn}} = 8 M_{\odot}$ for Type II supernovae, and

$$\text{SFR} = \int_{0.1M_{\odot}}^{100M_{\odot}} m \psi(m) dm. \quad (4.10)$$

These two equations result in an SFR of $\sim 116 M_{\odot} \text{ yr}^{-1}$.

The very low SFR obtained from the $\text{H}\alpha$ emission could result from extinction. However, the SFR estimated from the luminosity of the three diffuse radio components in NGC 7674 is still greater than the SFR calculated from the whole IR luminosity of the nuclear region. Thus, we conclude that these continuum components are more likely related to AGN activity, with no strong indication for a nuclear or circumnuclear starburst in our VLBI results.

4.4.1.2 The reason for the S-shaped pattern in NGC 7674, and the location of the AGN

Our continuum results at $\sim 100 \text{ mas}$ resolution (Figure 4.3) revealed the previously unknown continuum structures NE and SW. The overall shape of the continuum components in the nuclear region seem to form an S-shaped pattern. A detailed study on galaxies with similarly shaped radio structures was reported by Merritt & Ekers (2002). The authors point out that the orientation of a black hole's spin axis could dramatically change even in a minor merger, leading to a flip in the direction of any associated jet. Thus, following their discussion, it is possible that the components NE and SW are jet structures that formed before a possible black hole merger in NGC 7674. However, it is also possible that the interstellar medium could be diverting the outcoming jets from the AGN and causing them to form the NE and SW structures and the overall S-shaped pattern we are seeing in NGC 7674.

The black hole merger scenario would imply that the AGN may be located in the central component (C). However, the few high angular resolution observations available on this source are not enough to identify the AGN component in this galaxy. Early 18 cm VLBI observations at 20 mas resolution Unger et al. (1988) tentatively identified the component C to host the AGN, because of its brightness and proximity to the optical center of the galaxy. At a few mas resolution, the VLBA observations at 2.3 & 8.4 GHz (J. F. Gallimore & C. Murray-Krezan 2002, private communication) detected two of the three compact continuum features seen in the component C at 21 cm. These components seem to match the C1 and C3 structures seen in our 21 cm observations. The measured total fluxes at 2.3 & 8.4 GHz were noisy, and the derived spectral indices for the two components were neither flat, nor steep. For $S \propto \nu^{-\alpha}$, these values were $\alpha(\text{C1}) = 0.53$ and $\alpha(\text{C3}) = 0.35$. Thus, it is not clear whether either of these two components is hosting the AGN. Also, no information is available on the third structure seen in the central component. While it is possible that any of these compact sources could be hosting the AGN, they could also be shock-like features formed because of the interaction between the jet and compact interstellar clouds in the nuclear region of NGC7674.

4.4.2 The H I Absorption

Our observations reveal the details of the H I absorption against the radio continuum emission in NGC 7674 both at high angular resolution (17×5 mas, Figures 4.4 to 4.7), and low resolution (129×108 mas, Figures 4.8 to 4.11). The H I absorption at high angular resolution is composed of several features. The strongest H I line is the only feature with a measurable velocity gradient (Figure 4.6-top panel). The P-V diagram in position angle 14° (Figure 4.6-bottom panel), shows a velocity gradient of $1647 \text{ km sec}^{-1} \text{ kpc}^{-1}$. If this measured gradient is arising from H I gas in a rotating disk or torus, then at a radius of 17.4 mas (9.2 pc), assuming a Keplerian motion, the enclosed dynamical mass would be $5 \times 10^5 M_\odot$. However, calculation based on the observed width of the hidden broad H β emission line suggests a black hole mass in the range $(4.4 - 13.2) \times 10^7 M_\odot$, assuming an optical depth for electron scattering between $\tau_{\text{es}} = 0.1$ and 1 (Nishiura & Taniguchi 1998).

This difference could be explained by a rotating H I disk, with only a small section of it being illuminated by the background radio source. A similar explanation was put forward by Beswick, Pedlar, & McDonald (2002). These authors further suggested that the rotating H I disk should be edge-on, because of the non-detection of H I absorption toward the western or the eastern components seen on MERLIN scale.

However, our results clearly show H I absorption against E and NE, and no absorption against J, W, or SW (Figure 4.8). While a possible origin for the H I absorption toward E and NE could be neutral gas in intervening clouds far from the nuclear region of NGC 7674, the almost face-on orientation of the galaxy and the velocities of the detected H I features suggest that these H I absorption lines also arise within an H I disk or torus. Thus, this rotating H I disk around the central black hole should be inclined, i. e. should not be an edge-on structure.

Following the H I torus model illustrated by Peck (1999) which suggests the existence of dense neutral hydrogen clumps in the circumnuclear H I torus associated with a central AGN, it is very likely that the absorption features seen at both low and high angular resolution with velocity widths $< 50 \text{ km s}^{-1}$ arise from such clumpy structures. Thus, the velocity gradient seen in Figure 4.6 for the H I feature with a width of 35.4 km s^{-1} at half maximum, could be due to turbulent motion or infall of a dense clumpy structure within the H I torus, and not represent the rotational motion around the black hole. The absorption seen toward E and NE components could also arise in such H I clumps within the torus. An indication for the clumpy H I torus can be seen from the optical depths and the velocity widths of the various H I components listed in Tables 4.6 and 4.7. The narrower H I features (i.e. 1, 3, 4, I, II, & IV), which also have higher optical depths ($\gtrsim 0.3$), seem to represent the neutral hydrogen clumps in the torus, and the wider H I components (i.e. 2 & III), which have lower optical depths, seem to represent the rotating H I torus itself. Using virial considerations, the enclosed dynamical mass estimated from the widest H I feature ($\Delta v_{\text{FWHM}} = 165 \text{ km s}^{-1}$) at a radius of about 10 pc is $\sim 7 \times 10^7 M_{\odot}$. This value is consistent with the dynamical mass derived from the hidden broad H β emission by Nishiura & Taniguchi (1998).

4.4.2.1 The Location of the AGN: a more comprehensive picture

Observations of NGC 7674 with the BeppoSAX X-ray observatory by Malaguti et al. (1998) resulted in an absorption column density of $N_{\text{H}} \simeq 6 \times 10^{22} \text{ cm}^{-2}$, which is derived from the hard X-ray spectrum. Comparing this column density with the values listed in column 5 of Table 4.5 & 4.6 would suggest a spin temperature (T_{s}) of at least 1000 K. Such a high value could be expected for the H I spin temperature if the absorption is actually tracing a warmer atomic medium in the AGN environment (Gallimore et al. 1999), where the spin temperature can rise to several 1000 K before the hydrogen atoms are significantly ionized (Maloney, Hollenbach, & Tielens 1996).

However, the neutral hydrogen absorption studies in Seyfert galaxies by Gallimore et al. (1999) showed that the H I absorption in these galaxies generally avoids the nucleus, and it is more commonly seen against other radio components. This suggests that the absorption in the X-ray could be tracing different foreground gas than the absorption at 21 cm, and explains the higher column density in X-ray compared to the 21 cm H I absorption. This also suggests that the continuum structures associated with the H I absorption, namely C, E, and NE, are jet structures. This possibility is further supported by the steep spectra of these continuum structures seen at low resolutions discussed by Beswick, Pedlar, & McDonald (2002) and in section 3.1 of this work.

Based on the preceding discussion, we speculate that the AGN is located to the west of all the continuum structures that have H I absorption associated with them. This picture would exclude the W and SW components as AGN hosts, because of their steep spectra. Hence, a possible location for the AGN is in the J structure revealed for the first time in these sensitive VLBI observations. This implies that the two strongest sources, C and W, are possibly radio lobes or hot spots, with the AGN located somewhere in between these two structures, but simply free-free absorbed at 1.38 GHz.

4.4.3 The age of the AGN in NGC 7674

Using the above model for the location of the AGN and the nature of the C and W components, we can estimate the age of the AGN in NGC 7674. For this purpose, we follow the discussion in Carilli & Barthel (1996) for non-relativistic high Mach jets. The standard assumption is that the bulk of the kinetic energy supplied by the jet is $L_j = L_R/\epsilon$, where L_R is the total radio lobe luminosity, and ϵ is an efficiency factor for converting bulk kinetic energy into radio luminosity. The value of ϵ is ≤ 0.4 , but it is more likely to be considerably less (Carilli & Barthel 1996 and references therein). Also, the jet must do work ($W \approx P_L \times V_L$) to expand the ambient medium, where P_L is the lobe pressure derived using the minimum energy argument and V_L is the volume of the lobe. For the central component in NGC 7674, $L_R = 8.5 \times 10^{40}$ erg s $^{-1}$, $P_L = 12.3 \times 10^{-9}$ dyn cm $^{-2}$, and $V_L = 6.84 \times 10^{61}$ cm 3 . The source lifetime t_s , which could be indicative of the AGN lifetime, would be $t_s \approx W/L_j \simeq 0.3/\epsilon$ Myr. Thus, the estimated age of the AGN in NGC 7674 is few Myr, which is approximately the age of the young stellar population reported by Genzel et al. (1998).

4.5 CONCLUSIONS

We have presented the results of phase-referenced VLBI observations, using the VLBA, the phased VLA, and the 305-m Arecibo radio telescope, of the 21 cm continuum emission and the H I absorption in the central ~ 0.75 kpc of the type-2 Seyfert galaxy NGC 7674, which is also classified as a LIRG. The inclusion of both the phased VLA and Arecibo was a key factor in the success of these observations.

The low resolution continuum images reveal previously unknown structures in the nuclear region of this galaxy. The total VLBI flux density at 1380 MHz is 138 mJy, and represents only 60% of the total flux seen with the VLA at a lower resolutions, suggesting the existence of diffuse emission not detected by our VLBI array. All the observed structures seem to be related to AGN activity with no strong indication of a nuclear or circumnuclear starburst. The overall S-shaped pattern that the radio structures seem to

form could be the result of the interstellar medium diverting the outcoming jets from the central AGN. However, we cannot rule out the possibility of a black hole merger that could result in a similar structural pattern.

The high resolution images show at least seven compact sources in the components defined in the literature as central (C) and western (W). Their brightness temperature is $\gtrsim 10^7$ K. These compact sources are probably shock-like features formed due to the interaction of the jet with interstellar gas. However, one of these compact sources may actually be hosting the AGN. The currently available studies are insufficient to confirm such a possibility. Future sensitive multi-frequency VLBI observations will be the most direct way to identify a possible AGN component in the nuclear region of NGC 7674.

Both low and high resolution VLBI images show a complex H I absorption with several peaks. The detected H I lines have column densities on the order of 10^{21} cm $^{-2}$, assuming a spin temperature of 100 K. At low resolution, we distinguish at least four H I absorption peaks detected against the central (C), the eastern (W), and the northeastern (NE) components. No H I absorption was seen against the jet (J), the western (W), or the southwestern (SW) component. All these absorption features seem to arise in the H I disk or torus associated with the AGN. While the narrow features ($\Delta v_{\text{FWHM}} < 50$ km s $^{-1}$) could represent clumpy neutral hydrogen structures in the H I torus, the widest absorption feature ($\Delta v_{\text{FWHM}} = 165$ km s $^{-1}$) may represent the rotating torus itself. If the widest H I feature (component III) is rotationally broadened by a massive central object, the implied mass is about 10^7 M $_{\odot}$. This value of the derived enclosed mass is very consistent with the black hole mass calculated from the width of the hidden broad H β emission line. The detection of H I absorption toward some of the continuum components, and its absence toward others, suggest that the H I disk or torus is inclined and not edge-on as previously had been suggested.

Table 4.1: Parameters of the VLBI Observations of NGC 7674

Parameter	Value
Frequency	1380 MHz
Observing Date	2001 September 15
Observing Array	VLBA + Y27 + AR
Total observing time	12 hr
R.A. (J2000)	23 ^h 27 ^m 56 ^s .7097
Dec. (J2000)	+08°46′44″.135
Phase-referencing cycle time	2.5 min
Bandwidth	16 MHz
High resolution (11×5 mas) cont. image rms	67 μ Jy beam ⁻¹
Moderate resolution (20×20 mas) cont. image rms	34 μ Jy beam ⁻¹
Low resolution (92×76 mas) cont. image rms	78 μ Jy beam ⁻¹
Line velocity resolution	14 km s ⁻¹
High Resolution (17×5 mas) line image rms	260 μ Jy beam ⁻¹
Low Resolution (129×108 mas) line image rms	570 μ Jy beam ⁻¹
Angular to linear scale ^a	1 mas = 0.53 pc

NOTES: (a) Assumes distance of 115.6 Mpc, and $H_0 = 75$ km s⁻¹ Mpc⁻¹.

Table 4.2: Gaussian Fits to the Central Component in NGC 7674

Source	Relative Position ^a	Peak	Total	Major Axis ^b	Minor Axis ^b	P.A. ^c	T _b
(1)	(mas) (2)	(mJy beam ⁻¹) (3)	(mJy) (4)	(pc) (5)	(pc) (6)	(deg) (7)	(K) (8)
C1	0, 0	16.229 ± 0.006	27.060 ± 0.010	6.4	4.0	0.16	21.5 × 10 ⁷
C2	7.5W, 0N	5.023 ± 0.002	11.783 ± 0.006	7.8	4.7	5.98	6.6 × 10 ⁷
C3	16.5W, 1N	5.829 ± 0.002	8.405 ± 0.003	6.3	3.5	178.34	7.3 × 10 ⁷

NOTES: (a) The position (0,0) is $\alpha(\text{J2000}) = 23^{\text{h}}27^{\text{m}}56^{\text{s}}.7101$, $\delta(\text{J2000}) = +08^{\circ}46'44''.134$.

(b) Errors are ≤ 0.02 pc.

(c) Errors are ≤ 0.03 deg.

Table 4.3: Gaussian Fits to the Western Component in NGC 7674

Source	Relative Position ^a	Peak	Total	Major Axis ^b	Minor Axis ^b	P.A. ^c	T _b
(1)	(mas) (2)	(mJy beam ⁻¹) (3)	(mJy) (4)	(pc) (5)	(pc) (6)	(deg) (7)	(K) (8)
W1	0, 0	3.229 ± 0.002	12.386 ± 0.009	9.7	6.1	174	4.3 × 10 ⁷
W2	13.5E, 1N	0.891 ± 0.001	2.231 ± 0.002	7.9	4.9	169	1.2 × 10 ⁷
W3	22.5E, 3N	1.121 ± 0.002	2.726 ± 0.004	8.9	4.2	175	1.5 × 10 ⁷
W4	34.5E, 6N	0.628 ± 0.001	2.132 ± 0.002	10.0	5.3	164	0.8 × 10 ⁷

NOTES: (a) The position (0,0) is $\alpha(\text{J2000}) = 23^{\text{h}}27^{\text{m}}56^{\text{s}}.6790$, $\delta(\text{J2000}) = +08^{\circ}46'44''.369$.

(c) Errors are ≤ 0.03 pc.

(c) Errors are ≤ 0.002 deg.

Table 4.4: Parameters of the Continuum Components in Figure 4.4

Source	Relative Position ^a	Peak	Total	Major Axis ^b	Minor Axis ^b	P.A. ^c
(1)	(mas) (2)	(mJy beam ⁻¹) (3)	(mJy) (4)	(pc) (5)	(pc) (6)	(deg) (7)
C	0, 0	49.74 ± 0.01	52.74 ± 0.01	49.56 ± 0.02	41.85 ± 0.02	17
E	168E, 1N	6.46 ± 0.02	17.64 ± 0.05	77.29 ± 0.24	69.13 ± 0.32	78
W	450W, 226N	19.71 ± 0.04	25.07 ± 0.04	51.20 ± 0.10	48.60 ± 0.15	176
NE	317E, 213N	5.59 ± 0.01	20.57 ± 0.03	99.98 ± 0.18	72.01 ± 0.17	30
SW	633W, 68S	2.45 ± 0.01	15.73 ± 0.06	144.11 ± 0.98	87.31 ± 0.65	164
J	-	-	7.9	218	78	116

NOTES: (a) The position (0,0) is $\alpha(\text{J2000}) = 23^{\text{h}}27^{\text{m}}56^{\text{s}}.7098$, $\delta(\text{J2000}) = +08^{\circ}46'44''.137$.

(b) Half power width for components with gaussian fits. Linear extent on the plain of the sky for the jet component.

(c) Gaussian fit errors are ≤ 0.002 deg.

Table 4.5: Physical Properties of the Continuum Structures

Source	Magnetic Field	Pressure
	(Gauss)	(dyne cm ⁻²)
(1)	(2)	(3)
C	6.3×10^{-4}	12.3×10^{-9}
E	3.0×10^{-4}	2.8×10^{-9}
W	3.8×10^{-4}	4.5×10^{-9}
NE	2.8×10^{-4}	2.5×10^{-9}
SW	1.6×10^{-4}	0.8×10^{-9}

Table 4.6: Gaussian Fit Parameters of the H I Absorption Features at High Resolution

Feature	Velocity (km s ⁻¹)	Δv_{FWHM} (km s ⁻¹)	τ_{peak}	$N_{\text{HI}}/T_{\text{s}}$ (cm ⁻² K ⁻¹)	N_{HI} (cm ⁻²)
(1)	(2)	(3)	(4)	(5)	(6)
1	8603.1 ± 0.7	35.4 ± 2.3	0.412 ± 0.025	(2.8 ± 0.3) × 10 ¹⁹	(2.8 ± 0.3) × 10 ²¹
2	8577.6 ± 4.8	98.3 ± 7.1	0.164 ± 0.028	(3.1 ± 0.6) × 10 ¹⁹	(3.1 ± 0.6) × 10 ²¹
3	8573.3 ± 1.8	22.5 ± 4.3	0.298 ± 0.051	(1.3 ± 0.4) × 10 ¹⁹	(1.3 ± 0.4) × 10 ²¹
4	8534.3 ± 1.2	18.0 ± 2.9	0.337 ± 0.047	(1.2 ± 0.3) × 10 ¹⁹	(1.2 ± 0.3) × 10 ²¹

Table 4.7: Gaussian Fit Parameters of the H I Absorption Features at Low Resolution

Feature	Velocity (km s ⁻¹)	Δv_{FWHM} (km s ⁻¹)	$\tau_{\text{peak}} \times 10^{-3}$	$N_{\text{HI}}/T_{\text{s}}$ (cm ⁻² K ⁻¹)	N_{HI} (cm ⁻²)
(1)	(2)	(3)	(4)	(5)	(6)
I	8600.3 ± 1.1	49.8 ± 2.5	0.369 ± 0.016	(3.5 ± 0.2) × 10 ¹⁹	(3.5 ± 0.3) × 10 ²¹
II	8550.7 ± 1.8	30.8 ± 4.4	0.647 ± 0.080	(3.8 ± 0.7) × 10 ¹⁹	(3.8 ± 0.6) × 10 ²¹
III	8544.0 ± 8.9	165.0 ± 14.6	0.104 ± 0.010	(3.3 ± 0.3) × 10 ¹⁹	(3.3 ± 0.3) × 10 ²¹
IV	8536.3 ± 1.7	22.6 ± 4.0	0.434 ± 0.067	(1.9 ± 0.4) × 10 ¹⁹	(1.9 ± 0.4) × 10 ²¹

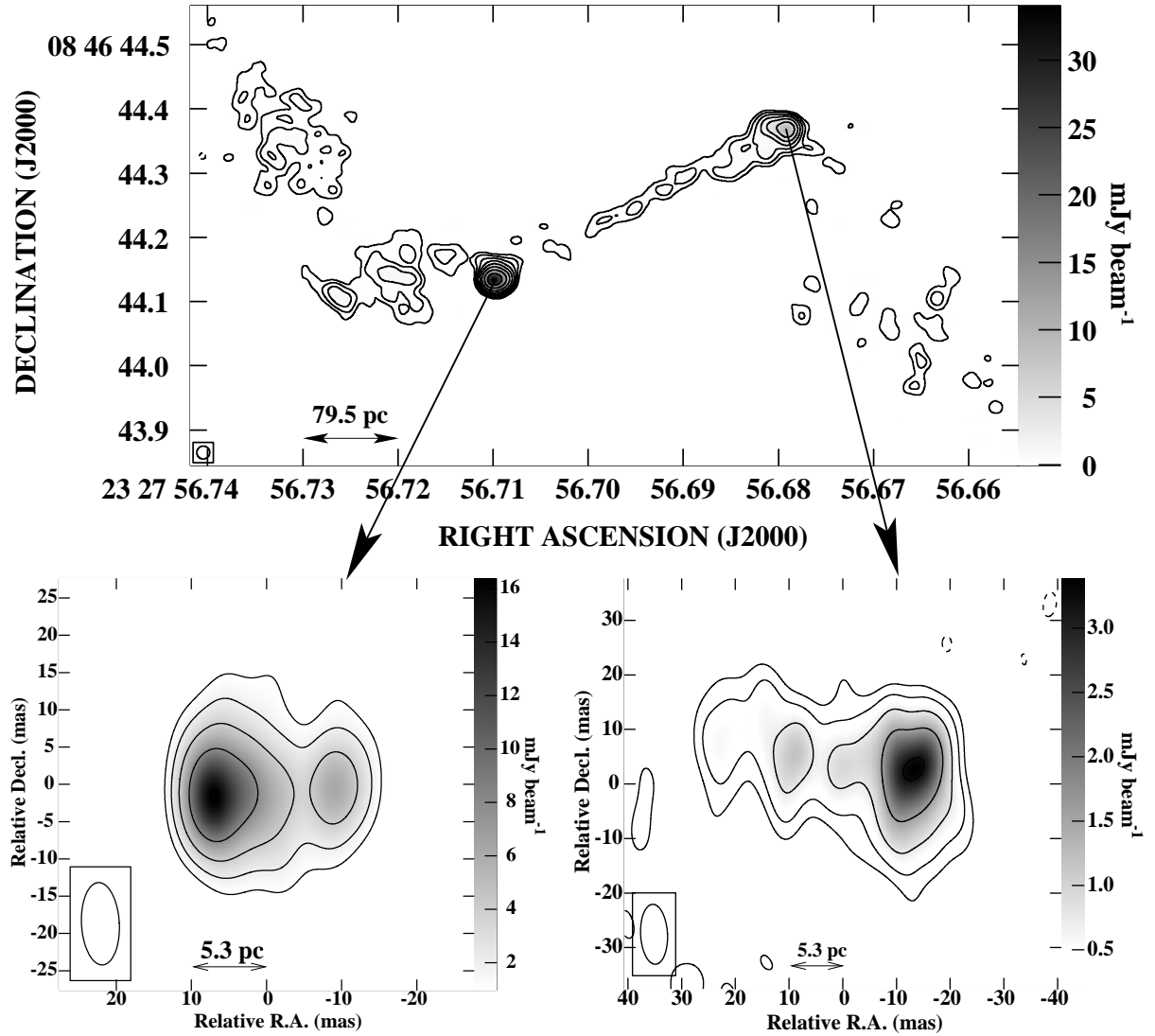


Figure 4.1: Continuum images of the nuclear region in NGC 7674 at 20 and 11×5 mas resolution. *Top*: Continuum image of the nuclear region in NGC 7674 at 1380 MHz. A Gaussian taper falling to 30% at $8 \text{ M}\lambda$ in the u direction and $15 \text{ M}\lambda$ in the v direction was applied. The restoring beam size is 20 mas . The peak flux is 34 mJy beam^{-1} , and the contour levels are at $-5, 5, 10, 20, 40, \dots, 640$ times the rms noise level, which is $34 \mu\text{Jy beam}^{-1}$. *Bottom*: Full resolution continuum images of the central (*left*) and the western (*right*) components in NGC 7674. The restoring beam size is $11 \times 5 \text{ mas}$ in position angle 3° . The peak fluxes are indicated with the wedge on the right side of each image. The rms noise in both images is $67 \mu\text{Jy beam}^{-1}$. The contour levels of the bottom-left image are at $-1, 1, 2, 4, 8, 16 \text{ mJy beam}^{-1}$, and the (0,0) point is $\alpha(\text{J2000}) = 23^{\text{h}}27^{\text{m}}56^{\text{s}}.7097$, $\delta(\text{J2000}) = 08^\circ46'44''.135$. The contour levels of the bottom-right image are at $-0.2, 0.2, 0.4, 0.8, 1.6, 3.2 \text{ mJy beam}^{-1}$, and the (0,0) point is $\alpha(\text{J2000}) = 23^{\text{h}}27^{\text{m}}56^{\text{s}}.6798$, $\delta(\text{J2000}) = 08^\circ46'44''.367$.

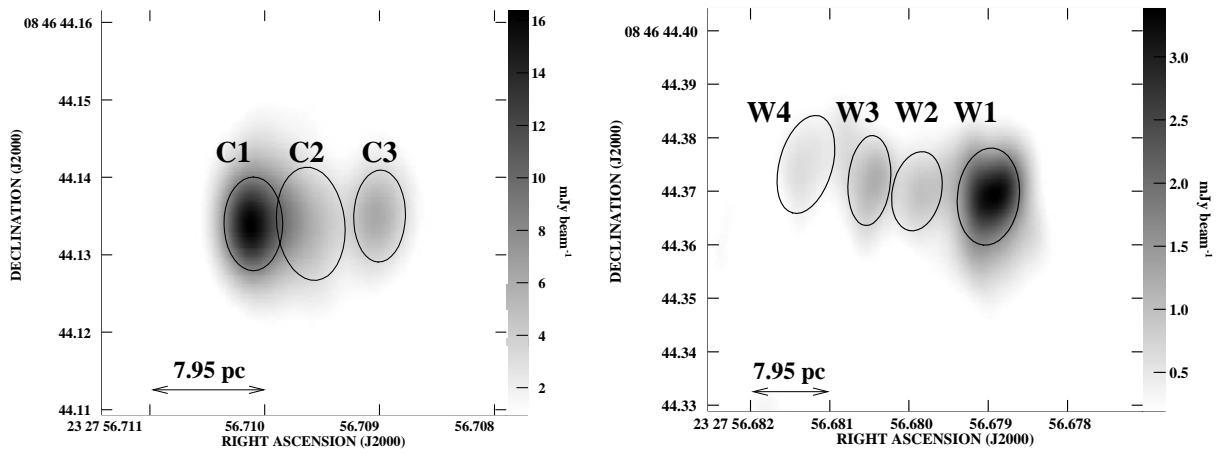


Figure 4.2: Gray scale continuum image of the central (*left*) and western (*right*) components in NGC 7674 at 11×5 mas resolution. The ellipses represent the gaussian fitting components at full width half maximum.

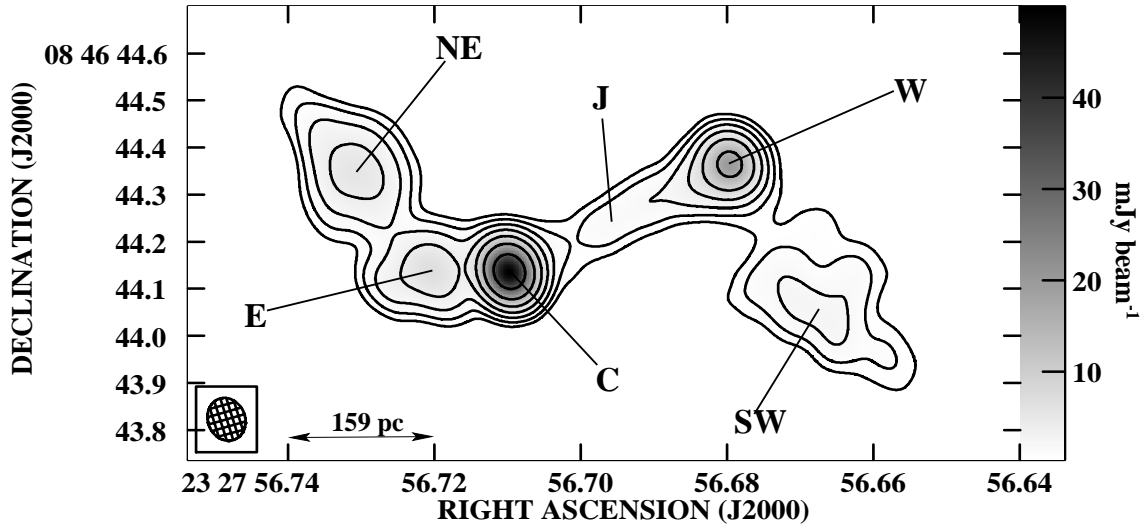


Figure 4.3: Continuum image of the nuclear region in NGC 7674 at 1380 MHz and 92×76 mas resolution. A two dimensional Gaussian taper falling to 30% at $2.5 M\lambda$ was applied. The contour levels are $-0.5, 0.5, 1, 2, 4, 8, 16, 32 \text{ mJy beam}^{-1}$. The rms noise level is $78 \mu\text{Jy beam}^{-1}$. The properties of the labeled components are listed in Table 4.4.

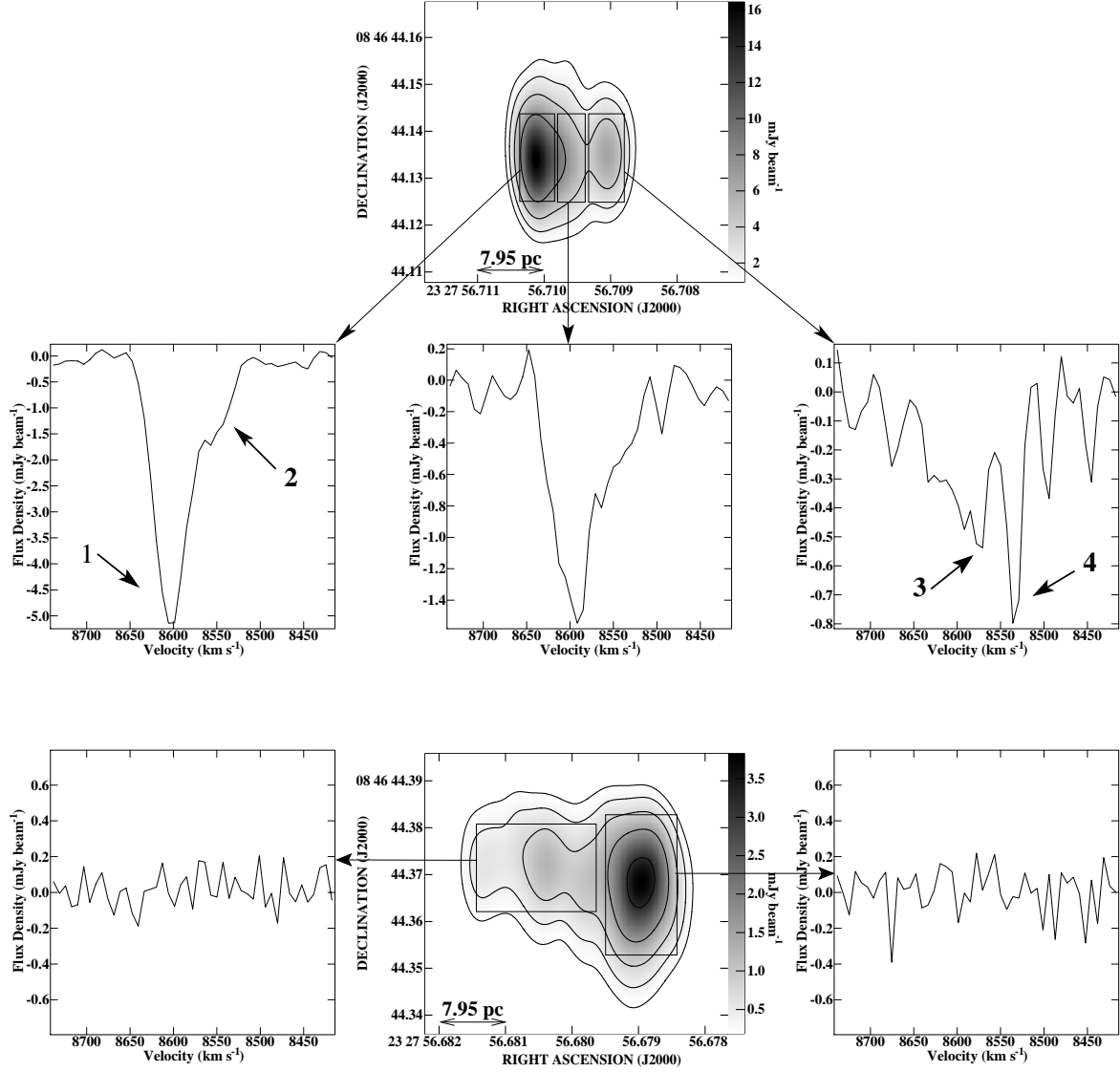


Figure 4.4: HI absorption spectra obtained at various locations against the central (*top*) and the western (*bottom*) components of NGC 7674 at 1380 MHz. The effective velocity resolution of the HI spectra is 14 km s⁻¹. The restoring beam size of both the continuum and the HI is 17×5 mas in position angle 3°. The contour levels of the continuum images are the same as in Figure 4.1-*bottom*.

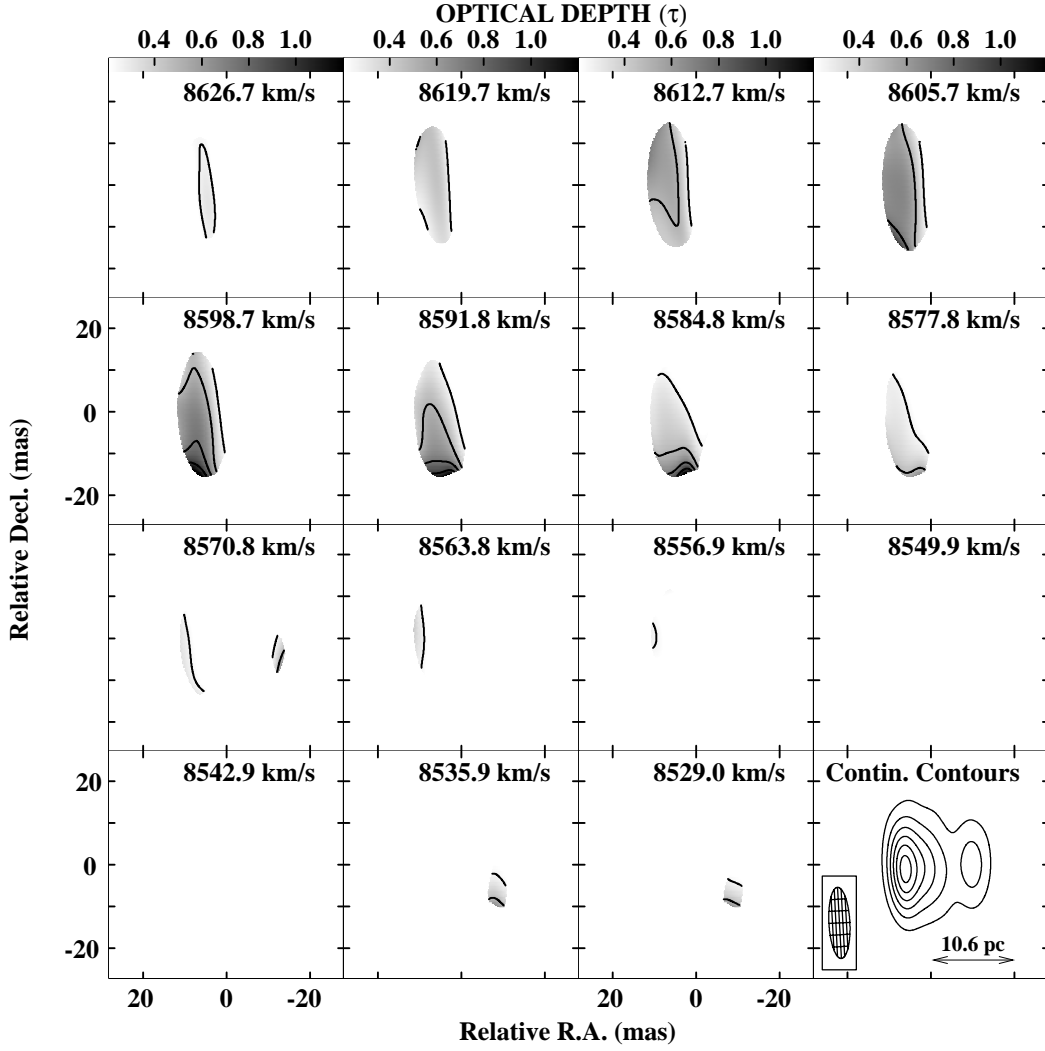


Figure 4.5: High resolution gray-scale and contour H I optical depth channel images toward the central component in NGC 7674 in the velocity range 8626.7–8529.0 km s⁻¹. The gray-scale range is indicated by the step wedge at the top of the images; the contour levels are 0.25, 0.5, 0.75, and 1.0. At the bottom-right corner a contour image of the continuum is shown as a positional reference with levels at 2.5, 5, 7.5, 10, 12.5 and 15 mJy beam⁻¹. The restoring beam in these images is 17 × 5 in position angle 3°. The point (0,0) is $\alpha(\text{J2000}) = 23^{\text{h}}27^{\text{m}}56^{\text{s}}.7097$, $\delta(\text{J2000}) = 08^{\circ}46'44''.135$.

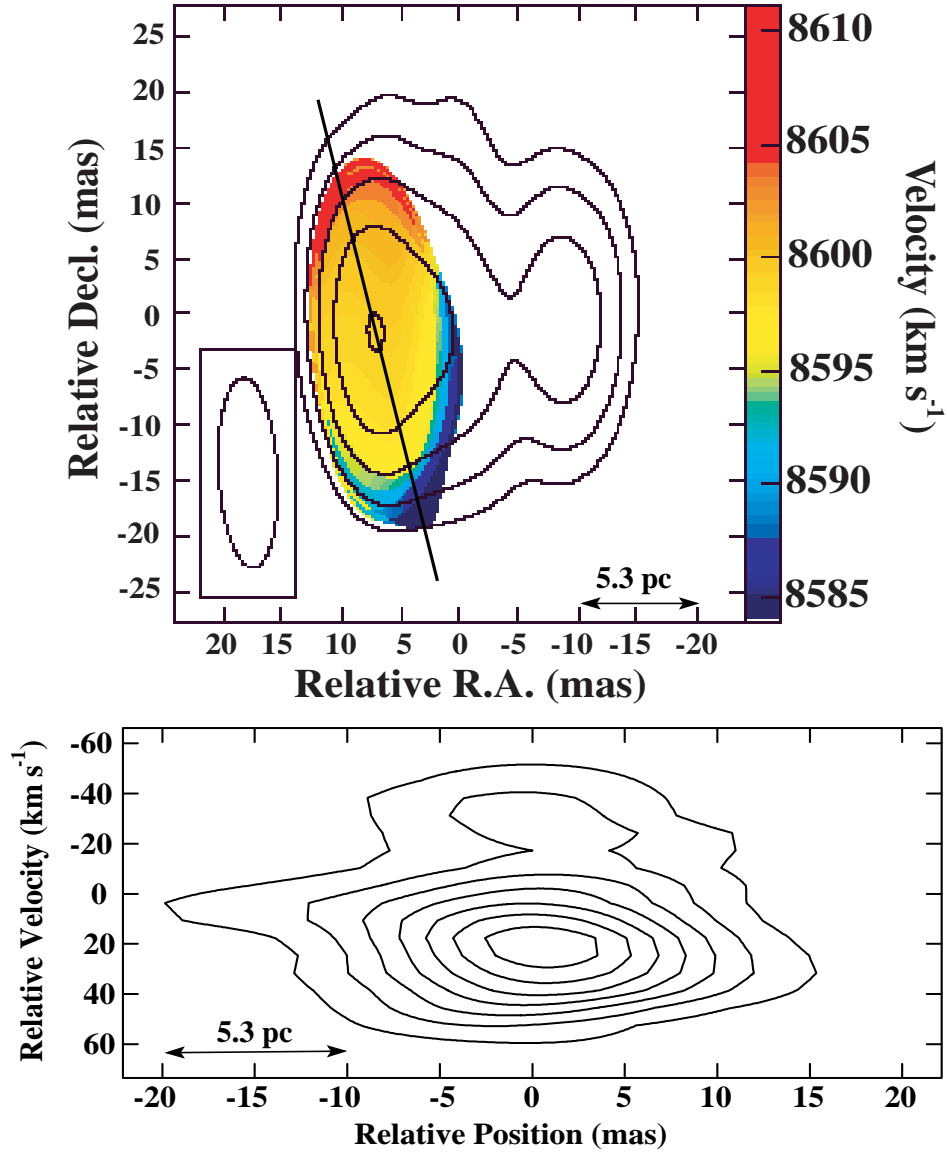


Figure 4.6: Velocity field and position-velocity plot (P.A. 14°) of the strongest H I absorption in NGC 7674 at high spatial resolution. *Top*: Velocity field of the strongest H I absorption feature at high spatial resolution, superimposed on the continuum contours with levels at 1, 2, 4, 8, 16 mJy beam^{-1} . The 17×5 mas (P.A. 3°) restoring beam is shown in the lower left corner. The point (0,0) is $\alpha(\text{J2000}) = 23^{\text{h}}27^{\text{m}}56^{\text{s}}.7097$, $\delta(\text{J2000}) = 08^\circ46'44''.135$. *Bottom*: Position-velocity plot of the 21 cm H I absorption along a cut in position angle 14° as shown in the top panel image. The zero point on the velocity scale corresponds to a heliocentric velocity (cz) of 8601.1 km s^{-1} . The contour levels of the PV plot are at $(-4, -8, -12, \dots, -28) \times 1\sigma$ ($260 \mu\text{Jy beam}^{-1}$).

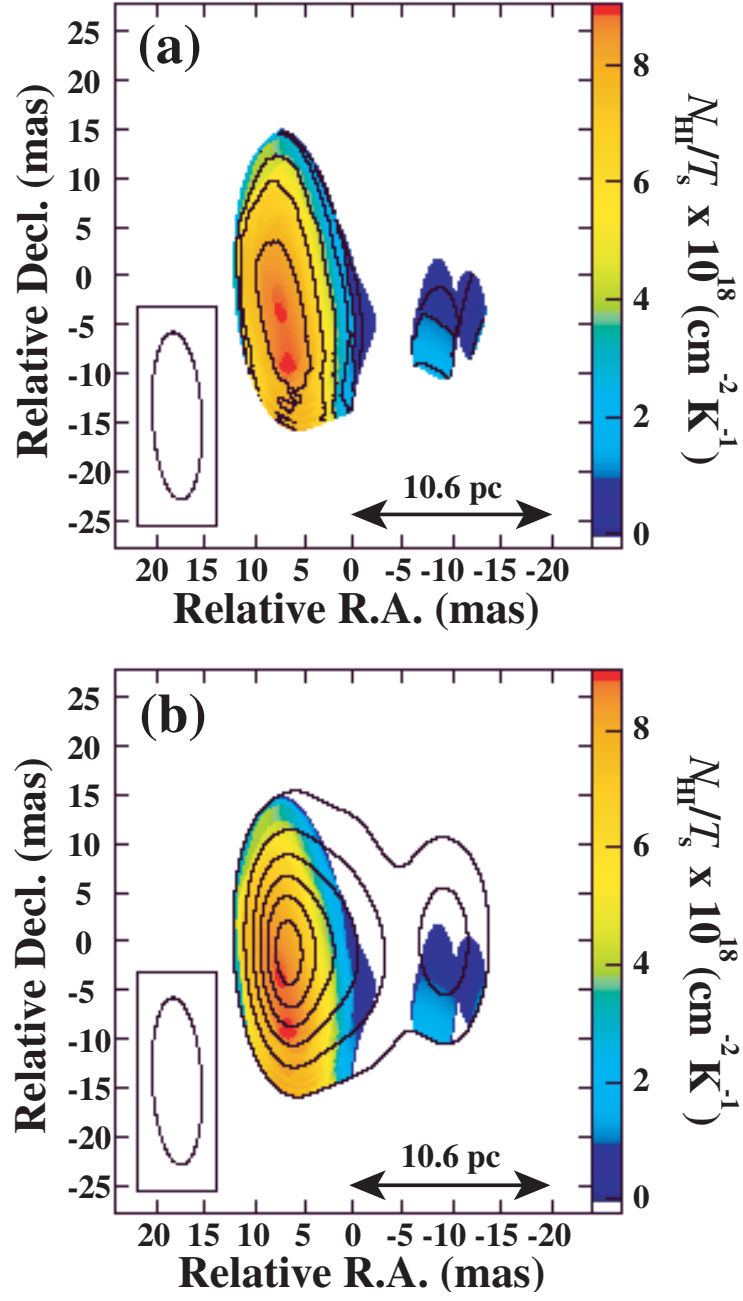


Figure 4.7: High angular resolution N_{HI}/T_s images in the velocity range 8626.7–8529.0 km s $^{-1}$: (a) N_{HI}/T_s color image and contours superimposed; the contours are at 0.5, 1, 2, 4, 6, 8 $\times 10^{18} \text{ cm}^{-2} \text{ K}^{-1}$ (b) N_{HI}/T_s color image with continuum contours superimposed; the contour levels are 2.5, 5, 7.5, ... 15 mJy beam $^{-1}$. The 17×5 mas (P.A. 3°) restoring beam is shown in the lower left corner of each image. The point (0,0) is $\alpha(\text{J2000}) = 23^{\text{h}}27^{\text{m}}56^{\text{s}}.7097$, $\delta(\text{J2000}) = 08^\circ46'44''.135$.

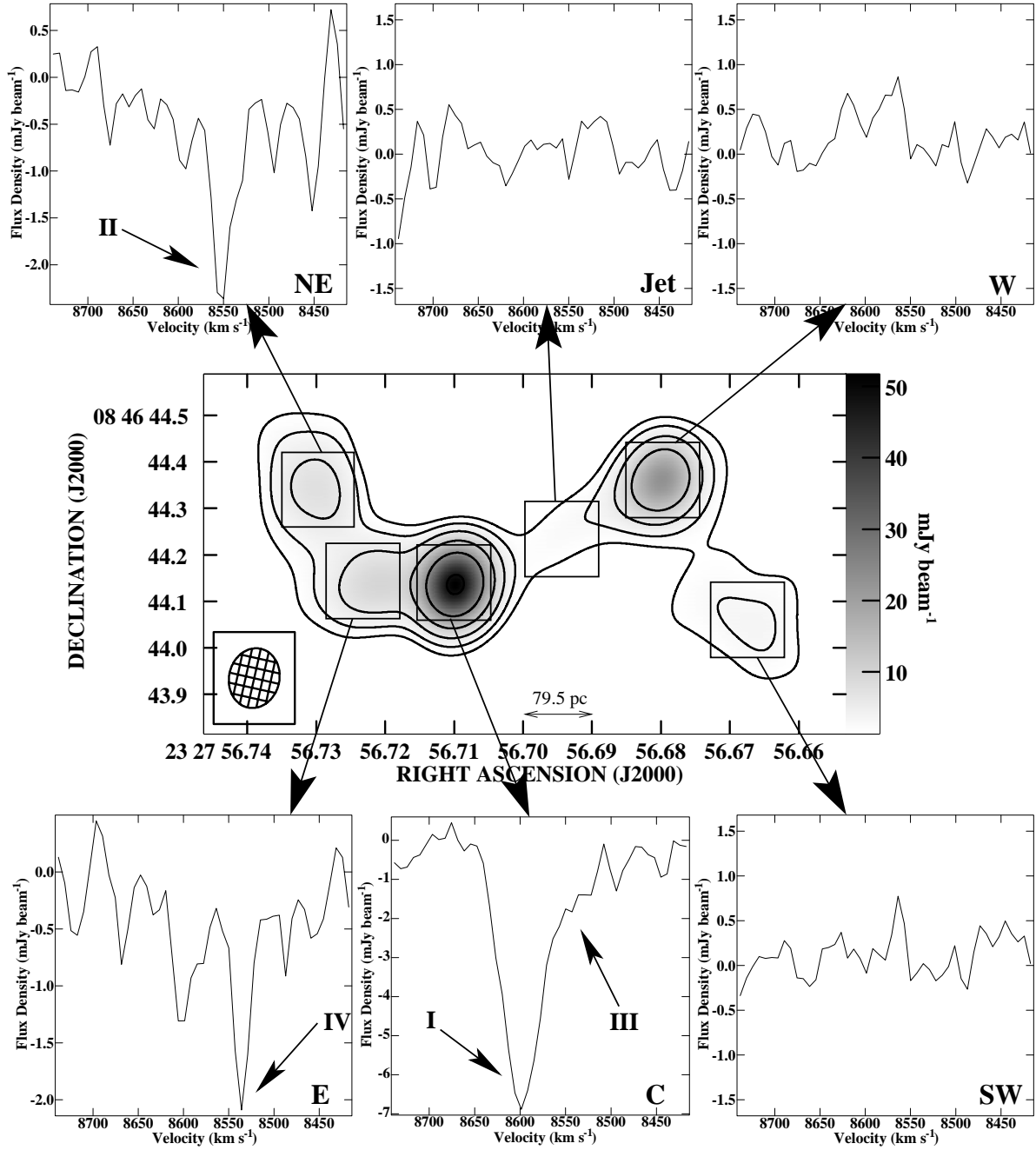


Figure 4.8: HI absorption spectra averaged against the continuum components of NGC 7674 at 1380 MHz and low spatial resolution. The effective velocity resolution of the HI spectra is 14 km s^{-1} . The restoring beam size of both the continuum and the HI is $129 \times 108 \text{ mas}$ in position angle -13° . The contour levels of the continuum image are at $-1.5, 1.5, 3, 6, \dots, 48 \text{ mJy beam}^{-1}$. The rms noise level of the continuum and the HI data are 85 and $570 \mu\text{Jy beam}^{-1}$, respectively. A two dimensional Gaussian taper falling to 30% at 1.4 MA was applied to obtain these images.

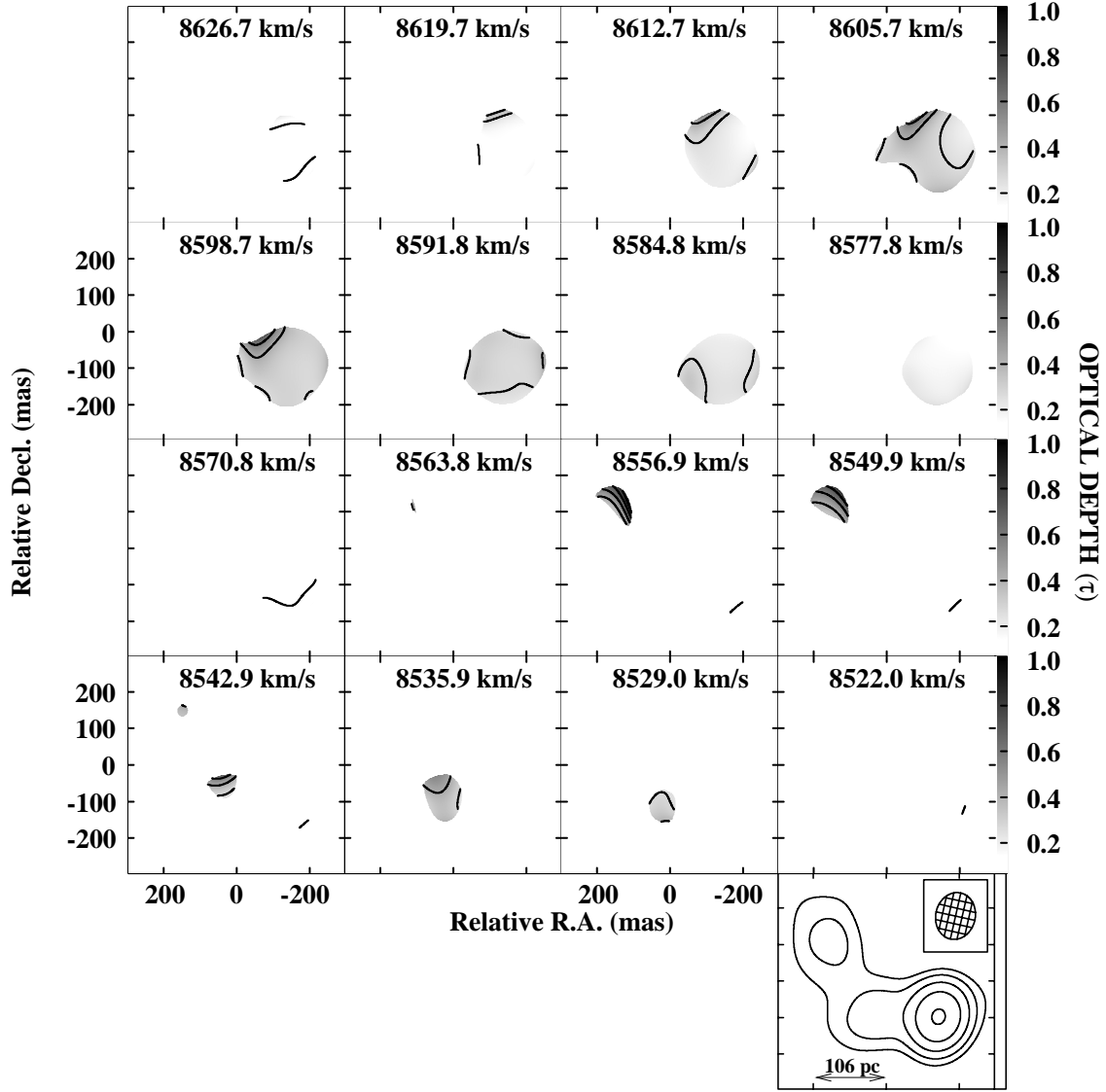


Figure 4.9: Low resolution gray-scale and contour HI optical depth channel images toward the central, eastern, and northeastern components in NGC 7674 in the velocity range 8626.7–8522.0 km s⁻¹. The gray-scale range is indicated by the step wedge on the right-side of the images; the contour levels are 0.15, 0.3, 0.45, 0.6, 0.75 and 0.9. At the bottom-right corner a contour image of the continuum is shown as a positional reference with levels at 3, 6, 12, 24 and 48 mJy beam⁻¹. The restoring beam in these images is 129 × 108 in position angle 13°. The point (0,0) is $\alpha(\text{J2000}) = 23^{\text{h}}27^{\text{m}}56^{\text{s}}.7195$, $\delta(\text{J2000}) = 08^{\circ}46'44''.234$.

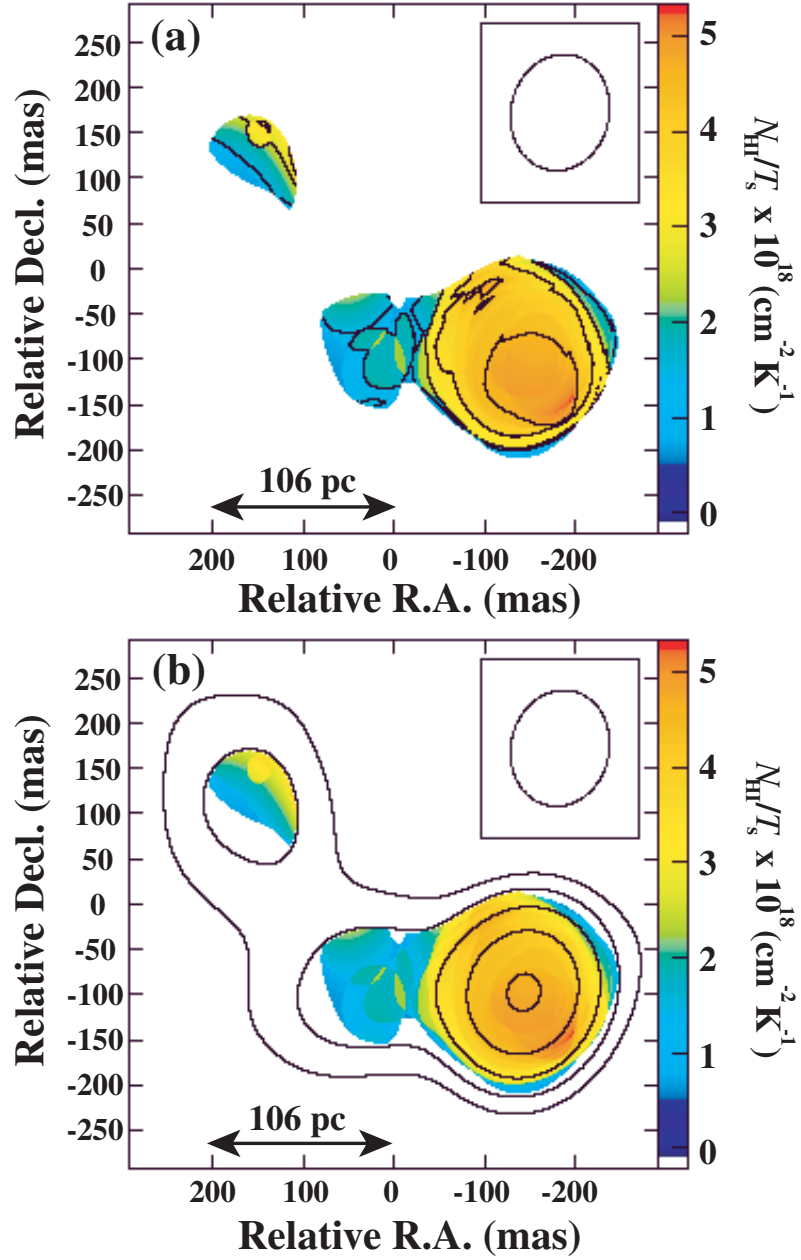


Figure 4.10: Low angular resolution N_{HI}/T_s images in the velocity range 8626.7–8522.0 km s $^{-1}$: (a) N_{HI}/T_s color image and contours superimposed; the contours are at 0.5, 1.5, 2.5, 3.5, 4.5 $\times 10^{18} \text{ cm}^{-2} \text{ K}^{-1}$ (b) N_{HI}/T_s color image with continuum contours superimposed; the contour levels are 3, 6, 12, ... 48 mJy beam $^{-1}$. The 129×108 mas (P.A. -13°) restoring beam is shown in the upper-right corner of each image. The point (0,0) is $\alpha(\text{J2000}) = 23^{\text{h}}27^{\text{m}}56^{\text{s}}.7195$, $\delta(\text{J2000}) = 08^\circ46'44''.234$.

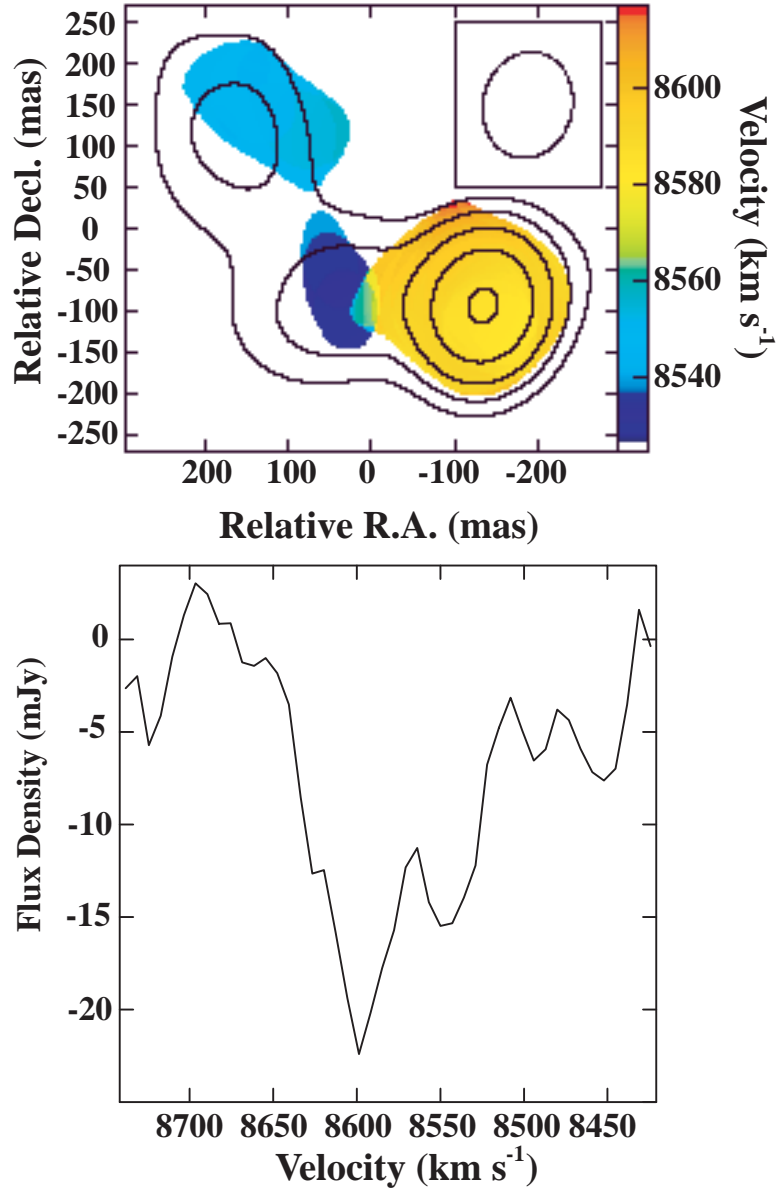


Figure 4.11: Velocity field of the H I absorption at low spatial resolution, and the integrated H I 21 cm absorption profile against the whole region where H I absorption is detected at low spatial resolution. *Top*: Velocity field of the H I absorption at low spatial resolution superimposed on the continuum contours with levels at 3, 6, 12, 24, 48 mJy beam⁻¹. The 129×108 mas (P.A. -13°) restoring beam is shown in the upper-right corner. *Bottom*: Integrated H I 21 cm absorption profile against the whole region where H I absorption is detected at low spatial resolution (129×108 mas). The double H I absorption profile is consistent with the two absorption features in the H I spectrum obtained with the 305-m Arecibo radio telescope at 3'3 resolution (Mirabel 1982).

Chapter 5

Summary and Future Work

5.1 SUMMARY

The main findings of the four projects comprising this thesis are briefly described below.

5.1.1 Global VLBI Observations of the high Velocity H I Absorption Toward NGC 1275

We have presented global VLBI observations of the $\sim 8100 \text{ km s}^{-1}$ H I absorption feature detected toward the strong radio nucleus 3C 84 of NGC 1275 in the Perseus cluster ($V_{\text{sys}} \sim 5200 \text{ km s}^{-1}$). The observations were obtained using the Very Long Baseline Array (VLBA), the phased Very Large Array (VLA), and three stations of the European VLBI Network (EVN). Our results provide the first high dynamic range image of this feature at high spectral and spatial resolutions. We detect six distinct absorption peaks with optical depths ranging from 0.1 to 0.45, and multiple weak features with $\tau \leq 0.1$. The compactness of the background radio source 3C 84, which has a linear extent of only about 16 pc, limits the conclusions that can be drawn as to the nature of the intervening object, which must be falling toward the center of the Perseus cluster at $\sim 3000 \text{ km s}^{-1}$. However, the detected absorption peaks indicate the existence of several H I clouds with velocity differences and widths similar to those seen in Galactic neutral hydrogen absorption and similar to some of the H I absorption seen in the Large Magellanic Cloud. The most prominent H I clouds extend from 12 to 30 mas (milliarcseconds) on the plane of the sky. The derived H I column

densities, assuming $T_s = 50$ K, range over $(0.35 - 3.8) \times 10^{20} \text{ cm}^{-2}$, and the implied volume densities range between 1.4 and 11 cm^{-3} .

5.1.2 Sensitive VLBI Continuum and H I Absorption Observations of the Ultra-Luminous IR Galaxy IRAS 17208–0014

We have presented phase-referenced VLBI observations of the radio continuum emission from, and the neutral hydrogen 21 cm absorption toward, the Ultra-Luminous Infrared Galaxy IRAS 17208–0014. The observations were carried out at 1362 MHz using the Very Long Baseline Array, including the phased Very Large Array as an element. The high-resolution radio continuum images reveal a nuclear starburst region in this galaxy, which is composed of diffuse emission approximately 670×340 pc on the plane of the sky, and a number of compact sources. These sources are most likely to be clustered supernova remnants and/or luminous radio supernovae. Their brightness temperatures range over $(2.2\text{--}6.6) \times 10^5$ K, with radio spectral luminosities between $(1 - 10) \times 10^{21} \text{ W Hz}^{-1}$. The total VLBI flux density of the starburst region is ~ 52 mJy, which is about 50% of the total flux density detected with the VLA at arcsecond resolution. For this galaxy, we derive a massive star formation rate of $\sim 84 \pm 13 M_\odot \text{ yr}^{-1}$, and a supernova rate of $\sim 4 \pm 1 \text{ yr}^{-1}$. H I absorption is detected in multiple components with optical depths ranging between 0.3 and 2.5, and velocity widths between 58 and 232 km s^{-1} . The derived column densities, assuming $T_s = 100$ K, range over $(10 - 26) \times 10^{21} \text{ cm}^{-2}$. The H I absorption shows a strong velocity gradient of 453 km s^{-1} across $0''.36$ (274 pc). Assuming Keplerian motion, the enclosed dynamical mass is about $2.3 \times 10^9 (\sin^{-2} i) M_\odot$, comparable to the enclosed dynamical mass estimated from CO observations.

5.1.3 Sensitive VLBI Continuum and H I Absorption Observations of the Seyfert-2 NGC 7674

We have presented phase-referenced VLBI observations of the radio continuum emission from, and the neutral hydrogen 21 cm absorption toward, the Luminous Infrared Galaxy

NGC 7674. The observations were carried out at 1380 MHz using the Very Long Baseline Array, the phased Very Large Array, and the 305-m Arecibo radio telescope. These observations constitute the first scientific use of the Arecibo telescope in a VLBI observation with the VLBA. The high- and low-resolution radio continuum images reveal several new continuum structures in the nuclear region of this galaxy. At ~ 100 mas resolution, we distinguish six continuum structures extending over 1.4 arcsec (742 pc), with a total flux density of 138 mJy. Only three of these structures were known previously. All these structures seem to be related to AGN activity. At the full resolution of the array (11×5 mas), we only detect two of the six continuum structures, namely the central and the western. Both are composed of several compact components with brightness temperatures ranging over $(0.8 - 21.5) \times 10^7$ K. While it is possible that one of these compact structures could host an AGN, they could also be shock-like features formed by the interaction of the jet with compact interstellar clouds in the nuclear region of this galaxy. At low spatial resolution (129×108 mas), we detect H I absorption only toward the central, the eastern, and the north-eastern components. Two of the four H I absorption peaks seen at this resolution are detected toward the central component. These four H I features have optical depths ranging between 0.1 and 0.65, and velocity widths between 23 and 165 km s $^{-1}$ at half maximum. The derived column densities, assuming $T_s = 100$ K, range over $(1.9 - 3.8) \times 10^{21}$ cm $^{-2}$. Assuming that the widest H I feature is associated with a rotating H I disk or torus feeding a central AGN, we estimate an enclosed dynamical mass of $\sim 7 \times 10^7 M_\odot$, comparable to the value derived from the hidden broad H β emission in this galaxy. The overall averaged H I spectrum toward all the continuum structures at 129×108 mas resolution is very consistent with the Arecibo single dish H I absorption spectrum at $3''.3$ resolution. At high resolution (17×5 mas), we distinguish four H I absorption features toward the central component. Their velocity widths are between 18 and 98 km s $^{-1}$ at half maximum, with optical depths ranging over 0.16 and 0.41, and column densities in the order of 10^{21} cm $^{-2}$.

5.2 FUTURE WORK

Based on the results reported in this thesis, several projects can be carried out to further enhance our understanding of interacting/merging galaxies and their evolution. Some of these projects will be proposed in the near future, some have already been granted observing time, and a few have even been observed:

- As part of the continuing effort to study the nature of the high velocity system associated with NGC 1275, VLA A array observations have been carried out in collaboration with A. P. Sarma. These observations will use the Zeeman effect in the H I absorption line to study the magnetic field seen in the high velocity system.
- Several multi-frequency radio observations will be used to continue studying the advanced merger system IRAS 17208-0014. One of the projects we have recently observed is the strong OH maser (megamaser) emission from this galaxy. The extreme merging conditions in IR galaxies could, in some cases, induce nuclear OH masing up to 10^6 times stronger than typical galactic masers (Baan 1989). The above mentioned OH emission observations were carried out with a sensitive VLBI array that included the VLBA, the phased VLA and the Green Bank Telescope (GBT). The data is currently being reduced. These observations will allow us to study the connection between extreme merging environments and OH megamaser emission at very high angular resolution. If the OH megamaser emission is found to be confined in a compact region, and if no correlation is found between the continuum emission of the starburst (reported in Chapter 3 of this thesis), then this would be evidence of a newly forming AGN in this galaxy. It should be noted that there has been no indication of an AGN in IRAS 17208-0014. In addition to the OH megamaser studies, low frequency (330 and 600 MHz) VLBA observations and 5 GHz MERLIN (Multi-Element Radio Linked Interferometer Network) observations will be utilized to further study the starburst region of this galaxy.
- Multi-frequency interferometric observations of NGC 7674 will be carried out to further investigate the various continuum structures in the nuclear region of this galaxy,

which are seen at both high (~ 10 mas) and low (~ 100 mas) angular resolutions (Chapter 4 of this thesis). These observations are: (1) Sensitive VLBI at 5 and 8 GHz with the VLBA, GBT, Arecibo, resulting in a few mas resolution; (2) 5 GHz with MERLIN, resulting in 50 mas resolution ; (3) 22 GHz VLA A array observations, resulting in 80 mas resolution. These observations will allow us to study the large scale jet structures in the nuclear region of NGC 7674. Moreover, these observations will be utilized to identify the AGN source in NGC 7674.

- In addition to the above mentioned projects, we will continue to study other interacting/merging systems at 21 cm, both in continuum and H I absorption. Two galaxies have already been observed with sensitive VLBI arrays: one is the triple merger system NGC 2623, and the other is the peculiar galaxy Arp 193. A third galaxy, UGC 02369, will be observed with MERLIN. In addition to these, several other merging systems will be considered for future observations. Each interacting/merging system in the universe represents a unique stage in galactic evolution that could extend for billions of years. Hence, observations of several such systems provide unique snapshots of different evolutionary periods.

References

- Arp, H. C. 1966, ApJS, 14, 1
- Baan, W. A. 1989, ApJ, 338, 804
- Beasley, A. J., Gordon, D., Peck, A. B., Petrov, L., MacMillan, D. S., Fomalont, E. B., & Ma, C. 2002, ApJS, 141, 13
- Benson, J. M. 1995, in Very Long Baseline Interferometry and the VLBA, ed. J. A. Zensus, P. J. Diamond, & P. J. Napier (San Francisco: ASP), 117
- Beswick, R. J., Pedlar, A., McDonald, A. R. 2002, MNRAS, 335, 1091
- Biretta, J. A., Bartel, N., Deng, J. 1991, in IAU Colloq. 131, Radio Interferometry: Theory, Techniques, and applications, ed. T. J. Cornwell & R. A. Perley (ASP Conf. ser. 19; San Fransisco:ASP), 334
- Bottinelli, L., Fraix-Burnet, D., Gouguenheim, L., Kazes, I., Le Squeren, A. M., Patey, I., Rickard, L. J., & Turner, B. E. 1985, A&A, 151, L7
- Browne, I. W. A., Patnaik, A. R., Wilkinson, P. N., & Wrobel, J. M. 1998, MNRAS, 293, 257
- Carilli, C. L., & Barthel, P. D. 1996, A&A Rev., 7, 1
- Carilli, C. L., & Taylor, G. B. 2000, ApJ, 532, L95
- Carilli, C. L., Wrobel, J. M., & Ulvestad, J. S. 1998, AJ, 115, 928
- Caulet, A., Woodgate, B. E., Brown, L.W., Gull, T. R., Hintzen, P., Lowenthal, J. D., Oliverson, R. J., & Ziegler, M. M. (1992), ApJ, 388, 301
- Cheng, K. P., Collins, N., Angione, R., Talbert, F., Hintzen, P., Smith, E. P., Stecher, T., & The UIT Team, 1997, UITVi; Vol. U.
- Cole, G. H. J., Pedlar, A., Holloway, A. J., & Mundell, G. C. 1999, MNRAS, 310, 1033
- Condon, J. J. 1992, ARA&A, 30, 575

- Condon, J. J., & Yin, Q. F. 1990, *ApJ*, 357, 97
- Condon, J. J., Helou, G., Sanders, D. B., & Soifer, B. T. 1996, *ApJS*, 103, 81
- de Grijp, M. H. K., Keel, W. C., Miley, G. K., Goudfrooij, P., Lub, J. 1992, *A&AS*, 96, 389
- de Vaucouleurs, G., de Vaucouleurs, A., & Corwin, J. R. 1976, *Second Reference Catalogue of Bright Galaxies*, University of Texas, Austin
- De Young, D. S., Roberts, M. S., & Saslaw W. C. 1973, *ApJ*, 185, 809
- Diamond, P. J., Lonsdale, C. J., Lonsdale, C. J., & Smith, H. E. 1999, *ApJ*, 511, 178
- Dickey, J .M. 1982, *ApJ*, 263, 87
- Dickey, J. M., Mebold, U., Marx, M., Amy, S., Haynes, R. F., & Wilson, W. 1994, *A&A*, 289, 357
- Downes D., & Solomon P. M. 1998, *ApJ*, 507, 615
- Faison, M. D., Goss, W. M., Diamond, P. J., & Taylor G. B. 1998, *AJ*, 116, 2916
- Faison, M. D., & Goss, W. M. 2001, *AJ*, 121, 2706
- Gallimore, J. F., Baum, S. A., O'Dea, C. P., Pedlar, A., & Brinks, E. 1999, *ApJ*, 524, 684
- Garwood, R. W., & Dickey, J. M. 1989, *ApJ*, 338, 841
- Genzel, R., et al. 1998, *ApJ*, 498, 579
- Goldader, J. D., Joseph, R. D., Doyon, R., & Sanders, D. B. 1995, *ApJ*, 444, 97
- González Delgado, R. M., Heckman, T., & Leitherer, C. 2001, *ApJ*, 546, 865
- Goss, W. M., Radhakrishnan, V., Brooks, J. W., & Murray, J. D. 1972, *ApJS*, 24, 123
- Helou, G., Soifer, B. T., & Rowan-Robinson, M. 1985, *ApJ*, 298, L7
- Hickson, P. 1982, *ApJ*, 255, 382
- Houck, J. R. et al. 1984, *ApJ*, 278, L63
- Houck, J. R., Schneider, D. P., Danielson, G. E., Neugebauer, G., Soifer, B. T., Beichman, C. A., & Lonsdale, C. J. 1985, *ApJ*, 290, L5

- Kennicutt, R. C. 1998, ARA&A, 36, 189
- Lutz, D., Veilleux, S., & Genzel, R. 1999, ApJ, 517, L13
- Malaguti, G. et al. 1998, A&A, 331, 519
- Malkan, M. A., Gorjian, V., Tam, R. 1998, ApJS, 117, 25
- Maloney, P. R., Hollenbach, D. J., Tielens, A. G. G. M. 1996, ApJ, 466, 561
- Martin, J. M., Bottinelli, L., Dennefeld, M., Gouguenheim, L., & Le Squeren, A. M. 1989, A&A, 208, 39
- Marx-Zimmer, M., Herbstmeier, U., Dickey, J. M., Zimmer, F., Staveley-Smith, L., & Mebold, U. 2000, A&A, 354, 787
- Melnick, J., & Mirabel, I. F. 1990, A&A, 231, L19
- Merritt, D., & Ekers, R. D., 2002, Science, 297, 1310
- Miley, G. 1980, ARA&A, 18, 165
- Mirabel, I. F. 1982, ApJ, 260, 75
- Mirabel, I. F., & Sanders D. B. 1988, ApJ, 335, 104
- Mundell, C. G., Ferruit, P., & Pedlar, A. 2001, ApJ, 560, 168
- Murphy, T. W. Jr., Armus, L., Matthews, K., Soifer, B. T., Mazzarella, J. M., Shupe, D. L., Strauss, M. A., & Neugebauer, G. 1996, AJ, 111, 1025
- Muxlow, T. W. B., Pedlar, A., Wilkinson, P. N., Axon, D. J., Sanders, E. M., & de Bruyn, A. G. 1994, MNRAS, 266, 455
- Napier, P. J. 1995, in Very Long Baseline Interferometry and the VLBA, ed. J. A. Zensus, P. J. Diamond, & P. J. Napier (San Francisco: ASP), 59
- Napier, P. J., Bagri, D. S., Clark, B. G., Rogers, A. E. E., Romney, J. D., Thompson, A. R., & Walker, R. C. 1994, Proc. IEEE, 82, 658
- Nishiura, S., Taniguchi, Y. 1998, ApJ, 499, 134
- Oort, J. H. 1976, PASP, 88, 591
- Peck, A. B. 1999, Ph. D. thesis, NMIMT

- Pedlar, A., Muxlow, T. W. B., Garrett, M. A., Diamond, P., Wills, K. A., Wilkinson, P. N., & Alef, W. 1999, *MNRAS*, 307, 761
- Pihlström, Y. M., Conway, J. E., Booth, R. S., Diamond, P. J., & Polatidis, A. G. 2001, *A&A*, 377, 413
- Radhakrishnan, V., Goss, W. M., Murray, J. D., & Brooks, J. W. 1972, *ApJS*, 24, 49
- Romney, J. D. 1978, Ph.D. thesis, California Institute of Technology
- Romney, J. D. 1999, in *Synthesis Imaging in Radio Astronomy II*, ed. G. B. Taylor, C. L. Carilli, & R. A. Perley (San Francisco: ASP), 433
- Rieke, G. H., & Lebofsky, M. J. 1986, *ApJ*, 304, 326
- Rubin, V. C., Ford, W. K. Jr., Peterson, C. J., & Lynds, C. R. 1978, *ApJS*, 37, 235
- Rubin, V. C., Ford, W. K. Jr., Peterson, C. J., & Oort, J. H. 1977, *ApJ*, 211, 693
- Rupen, M. P., van Gorkom, J. H., Knapp, G. R., Gunn, J. E., & Schneider, D. P. 1987, *AJ*, 94, 61
- Salpeter, E. E. 1955, *ApJ*, 121, 161
- Sandage, A., & Bedke, J. 1994, *The Carnegie Atlas of Galaxies*, vol. 1.
- Sanders, D. B., Soifer, B. T., Elias, J. H., Madore, B. F., Matthews, K., Neugebauer, G., & Scoville, N. Z. 1988, *ApJ*, 325, 74
- Sanders, D. B., Egami, E., Lipari, S., Mirabel, I. F., & Soifer, B. T. 1995, *AJ*, 110, 1993
- Sanders, D. B., & Mirabel, I. F. 1996, *ARA&A*, 34, 749
- Scalo, J. 1986, *Fundam. Cosmic Phys.*, II, 1
- Scoville, N. Z., & Soifer, B. T. 1991, in *Massive Stars in Starbursts*, ed. C. Leitherer, N. Walborn, T. Heckman, & C. Norman (Cambridge: Cambridge Univ. Press), 233
- Scoville, N. Z., et al. 1998, *ApJ*, 492, L107
- Scoville, N. Z., et al. 2000, *AJ*, 119, 991
- Sijbring, D. 1993, Ph.D. thesis, Rijksuniversiteit Groningen
- Silver, C. S., Taylor, G. B., & Vermeulen, R. C. 1998, *ApJ*, 502, 229

- Smith, H. E., Lonsdale, C. J., & Lonsdale, C. J. 1998a, *ApJ*, 492, 137
- Smith, H. E., Lonsdale, C. J., Lonsdale, C. J., & Diamond, P. J. 1998b, *ApJ*, 493, L17
- Soifer, B. T. et al. 1984, *ApJ*, 278, L71
- Soifer, B. T., Sanders, D. B., Neugebauer, G., Danielson, G. E., Lonsdale, C. J., Madore, B. F., & Persson, S. E. 1986, *ApJ*, 303, L41
- Soifer, B. T., et al. 2000, *AJ*, 119, 509
- Solomon, P. M., Downes, D., Radford, S. J. E., & Barrett, J. W. 1997, *ApJ*, 478, 144
- Staveley-Smith, L., & Davies, R. D. 1987, *MNRAS*, 224, 953
- Taylor, G. B., & Vermeulen, R. C. 1996, *ApJ*, 457, L69
- Ulvestad, J. S., & Antonucci, R. J. 1997, *ApJ*, 488, 621
- Unger et al. 1988, *MNRAS*, 234, 754
- Unger, S. W., Taylor, K., Pedlar, A., Ghataure, H. S., Penston, M. V., & Robinson, A. 1990, *MNRAS*, 242, 33
- van den Bergh, S. 1977, *Astron. Nachr.*, 298, 285
- Veilleux, S., Kim, D.-C., Sanders, D. B., Mazzarella, J. M., & Soifer, B. T. 1995, *ApJS*, 98, 171
- Verdes-Montenegro, L., del Olmo, A., Perea, J., Athanassoula, E., Márquez, I., & Augarde, R. 1997, *A&A*, 321, 409
- Verontsov-Velyaminov, B. A. 1959, *Atlas and Catalogue of Interacting Galaxies, Part I*, Moscow, Moscow State University
- Verontsov-Velyaminov, B. A. 1977, *Part II, A&AS*, 28, 1
- Vermeulen, R. C., Readhead, A. C. S., & Backer, D. C. 1994, *ApJ*, 429, L41
- Walker, C. R. 1999, in *Synthesis Imaging in Radio Astronomy II*, ed. G. B. Taylor, C. L. Carilli, & R. A. Perley (San Francisco: ASP), 433
- Walker, R. C., Romney, J. D., & Benson J. M. 1994, *ApJ*, 430, L45
- Weiler, K. W., & Sramek, R. A., 1988, *ARA&A*, 26, 295

Wunderlich, E., & Klein, U. 1988, A&A, 206, 47

Yun, Min S., Reddy, N. A., & Condon, J. J. 2001, ApJ, 554, 803

Zenner, S., & Lenzen, R. 1993, A&AS, 101, 363